Report UFLA-DAAK02-74-102

INVESTIGATION OF ELECTRONIC TRANSPORT,
RECOMBINATION AND OPTICAL PROPERTIES
IN $InAs_{1-x}P_x$ ALLOY SYSTEMS

Sheng S. Li
University of Florida
Engineering and Industrial Experiment Station
Gainesville, Florida 32611

1 May 1976

FINAL REPORT
30 November 1973 - 31 March 1976

DISCLAIMER NOTICE

THIS DOCUMENT IS THE BEST
QUALITY AVAILABLE.

COPY FURNISHED CONTAINED
A SIGNIFICANT NUMBER OF
PAGES WHICH DO NOT
REPRODUCE LEGIBLY.

INVESTIGATION OF ELECTRONIC TRANSPORT, RECOMBINATION AND OPTICAL PROPERTIES IN InAs$_{1-x}$P$_x$ ALLOY SYSTEMS

Sheng S. Li
University of Florida
Engineering and Industrial Experiment Station
Gainesville, Florida 32611

1 May 1976

FINAL REPORT
30 November 1973 - 31 March 1976

DISTRIBUTION STATEMENT

Approved for public release;
distribution unlimited
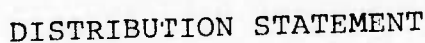
PREPARED FOR
ADVANCED RESEARCH PROJECTS AGENCY
1400 Wilson Blvd.
Arlington, Virginia 22209

MONITORING OFFICE
ARMY NIGHT VISION LABORATORY
Fort Belvoir, Virginia 22060

REPORT DOCUMENTATION PAGE

READ INSTRUCTIONS
BEFORE COMPLETING FORM

1. REPORT NUMBER	2. GOVT ACCESSION NO.	3. RECIPIENT'S CATALOG NUMBER
UFLA-DAAK02-74		

TITLE (and Subtitle)

Investigation of Electronic Transport, Recombination and Optical Properties in InAs$_{1-x}$P$_x$ Alloy Systems.

5. TYPE OF REPORT & PERIOD COVERED

Final Report, Dec 73 - Apr 76

6. PERFORMING ORG. REPORT NUMBER

7. AUTHOR(s)

Sheng S. Li

8. CONTRACT OR GRANT NUMBER(s)

DAAK02-74-C-0102, ARPA Order-2182

9. PERFORMING ORGANIZATION NAME AND ADDRESS

University of Florida
Engineering & Industrial Experiment Station
Gainesville, Florida 32611

10. PROGRAM ELEMENT, PROJECT, TASK AREA & WORK UNIT NUMBERS

61101E, ARPA 2182, 6D10, 017 CJ

11. CONTROLLING OFFICE NAME AND ADDRESS

Advanced Research Projects Agency
1400 Wilson Blvd.
Arlington, Virginia 22209

12. REPORT DATE

May 1976

13. NUMBER OF PAGES

139

14. MONITORING AGENCY NAME & ADDRESS(if different from Controlling Office)

Night Vision Laboratory
U.S. Army Electronics Command
Fort Belvoir, Virginia 22060

15. SECURITY CLASS. (of this report)

unclassified

15a. DECLASSIFICATION/DOWNGRADING SCHEDULE

16. DISTRIBUTION STATEMENT (of this Report)

Approved for public release; distribution unlimited.

17. DISTRIBUTION STATEMENT (of the abstract entered in Block 20, if different from Report)

18. SUPPLEMENTARY NOTES

This research was supported by the Defense Advanced Research Project Agency.

19. KEY WORDS (Continue on reverse side if necessary and identify by block number)

InAs$_{1-x}$P$_x$ epitaxial samples, electron scattering electrical resistivity, Hall coefficient, electron mobility, electron concentration, optical absorption coefficient, energy band gap.

20. ABSTRACT (Continue on reverse side if necessary and identify by block number)

An experimental study has been made of the transport properties of InAs$_{1-x}$P$_{(x)}$ grown epitaxially from the vapor phase onto semi-insulating GaAs substrates. The hydrogen carrier gas flow rate was varied for four sets of samples of InAs$_{0.61}$P$_{(0.39)}$ with changing thickness between sets. A fifth set was investigated with varying composition. Resistivity and Hall effect measurements from 3K to 300K yielded electron mobilities as high as 13,100 cm^2/volt-sec at 77K and electron concentrations from 1.5x10^{16} cm^{-3} to 8x10^{16} cm^{-3} at 300 K. Transport at low temperatures (T<30K) is attributed to the formation of a donor impurity band

(over)

*1.5 x 10 to the 16th power/cc to 8 x 10 to the 16th power/cc

20. (cont'd.)

Optical transmission measurements and electron microprobe analyses were made on bulk $InAs_{1-x}P_x$ samples of different compositions.

Absorption coefficient as a function of wavelength near the fundamental absorption edge was deduced from transmission data. Energy band gap versus alloy composition was determined for these samples for $0 \leq x \leq 1$.

Surface photovoltage technique was employed to determine the hole diffusion length on three n-type InP specimens with (111) and (100) orientations. The measured hole diffusion length was found to be independent of the surface conditions.

PREFACE

This final technical report covers the research activities from December 1973 through April 1976 under contract DAAK02-74-C-0102. This research was supported by the Defense Advanced Research Project Agency (order No. 2182) and monitored by the Army Night Vision Laboratory, Fort Belvoir, Va. Mr. David A. Jackson, Jr. was the initial contract monitor. Mr. Terry Jones is currently the responsible contract monitor for the Army Night Vision Laboratory. Major contributors are J. R. Anderson, D. W. Schoenfeld and R. A. Owen. Additional support derived from Dr. J. K. Kennedy of the Air Force Cambridge Research Laboratory who so generously prepared the needed $InAs_{1-x}P_x$ epitaxial samples for this contract research. The bulk specimens of InAsP were supplied by Dr. R. Behringer of the Naval Research Laboratory.

Additional information on the results of our earlier efforts were covered in the three semi-annual technical reports.

<div style="text-align: right">

Sheng S. Li
Principal Investigator

</div>

ABSTRACT

An experimental study has been made of the transport properties of $InAs_{1-x}P_x$ grown epitaxially from the vapor phase onto semi-insulating GaAs substrates. The hydrogen carrier gas flow rate was varied for four sets of samples of $InAs_{0.61}P_{0.39}$ with changing thickness between sets. A fifth set was investigated with varying composition. Resistivity and Hall effect measurements from 3K to 300K yielded electron mobilities as high as 13,100 cm^2/volt-sec at 77K and electron concentrations from $1.5 \times 10^{16} cm^{-3}$ to $8 \times 10^{16} cm^{-3}$ at 300K. Transport at low temperatures (T<30K) is attributed to the formation of a donor impurity band.

Optical transmission measurements and electron microprobe analyses were made on bulk $InAs_{1-x}P_x$ samples of different compositions.

Absorption coefficient as a function of wavelength near the fundamental absorption edge was deduced from transmission data. Energy band gap versus alloy composition was determined for these samples for $0 \leq x \leq 1$.

Surface photovoltage technique was employed to determine the hole diffusion length on three n-type InP specimens with (111) and (100) orientations. The measured hole diffusion length was found to be independent of the surface conditions.

TABLE OF CONTENTS

PART I

ELECTRICAL AND TRANSPORT PROPERTIES OF EPITAXIALLY GROWN $InAs_{1-x}P_x$

PART II

OPTICAL AND RECOMBINATION PROPERTIES
OF BULK $InAs_{1-x}P_x$ SYSTEM

SEMI-ANNUAL REPORTS

1. Sheng S. Li, "Investigation of Basic Electronic Transport, Recombination and Optical Properties in $InAs_{1-x}P_x$ Alloy System," First Semi-Annual Technical Report, Contract No. DAAK02-74-C-0102, Night Vision Laboratory, June 15, 1974.

2. Sheng S. Li, "Investigation of Basic Electronic Transport, Recombination and Optical Properties in $InAs_{1-x}P_x$ Alloy System," Second Semi-Annual Technical Report, Contract No. DAAK02-74-C-0102, Army Night Vision Laboratory, December, 1974.

3. Sheng S. Li, "Investigation of Basic Electronic Transport, Recombination and Optical Properties in $InAs_{1-x}P_x$ Alloy System," Third Semi-Annual Technical Report, Contract No. DAAK02-74-C-0102, Army Night Vision Laboratory, June, 1975.

PART I

ELECTRICAL AND TRANSPORT PROPERTIES
OF EPITAXIALLY GROWN $InAs_{1-x}P_x$

CHAPTER I

INTRODUCTION

There has been an active interest in the development
and properties of III-V compounds. Lately, much of this
effort has been directed toward III-V ternary compounds,
especially the $InAs_{1-x}P_x$ system because of its many useful
characteristics such as high electron mobility and broad
range of energy band gaps (0.36ev for InAs to 1.29ev for
InP). These characteristics indicate that the $InAs_{1-x}P_x$
system has several device applications such as injection
laser diodes[1] and detecting devices operable in the infrared
region with wavelengths from 0.96 to 3.45 μm. Highly
efficient photocathodes operating at 1.06 μm have been
fabricated[2,3] from the $InAs_{1-x}P_x$ system. The band structure
and high mobility also indicate the possibility of high
frequency applications such as Gunn oscillators.[4,5]

Folberth[6] first reported both the $InAs_{1-x}P_x$ and the
$GaAs_{1-x}P_x$ systems in 1955. However, the $InAs_{1-x}P_x$ system
was almost totally ignored since research at that time was
directed more toward materials, such as $GaAs_{1-x}P_x$, whose
band gaps were in the visible light range. Now with the
interest in infrared emission and detection there is a
renewed interest in $InAs_{1-x}P_x$. All work, until recently,

1

on $InAs_{1-x}P_x$ has been attempts to grow pure single crystals using standard bulk techniques previously successful with group IV semiconductors.[7,8] The resulting crystals were typically inhomogenous and polycrystalline. Vapor-deposited epitaxial layers of $InAs_{1-x}P_x$ were first reported by Tietjen et al.[9] in 1969. The layers were grown on conducting InAs substrates which had to be mechanically removed before measurements could be made on the epilayers. Thus, layers of at least 100 μm thicknesses had to be grown to insure mechanical strength. Later, Allen and Mehal[10,11] deposited $InAs_{1-x}P_x$ on substrates of both GaAs and GaP for their insulating nature and for their utility as optical windows in photocathodes.

Epitaxially grown $InAs_{1-x}P_x$ is limited, as yet, by impurity content, surface states, and low mobility. There is then a need to broaden the knowledge of not only the electrical characteristics of epitaxial $InAs_{1-x}P_x$ but also how those characteristics may be enhanced by altering the growth conditions. These are the basic intentions of this research.

A general discussion of some theoretical aspects is presented in Chapter II. The effects of different scattering modes, especially those important to $InAs_{1-x}P_x$, are considered. Also the idea of conduction within an impurity band is developed.

The samples used for this research were epitaxially deposited using the hydride system similar to Tietjen's. The

growth procedure is presented in Chapter III along with a summary of the experimental methods used in measuring the transport properties.

The experimental results obtained for samples of $InAs_{0.61}P_{0.39}$ grown with different flow rates and varying epitaxial thicknesses are presented in Chapter IV. The results for samples of varying composition ($InAs_{1-x}P_x$) are presented in Chapter V. In both chapters the results are compared to the theory of Chapter II.

In the last chapter some conclusions are made concerning the properties of these epitaxial samples.

CHAPTER II

THEORY OF ELECTRON TRANSPORT IN $InAs_{1-x}P_x$

2.1 Scattering Processes

In any semiconductor, the charge carriers (i.e.
electrons and holes), at temperatures above absolute
zero, may be scattered by a number of different mechanisms.
These mechanisms normally have their dominance in certain
temperature regimes but in some cases two or more may be
interacting simultaneously. In a polar semiconductor, such
as $InAs_{1-x}P_x$, the most important scattering mechanisms
which limit the mobility of the charge carriers are polar
optical phonon scattering, ionized impurity scattering,
neutral impurity scattering, and electron-electron
collisions.

In the following sections the theoretical effects of
these scattering mechanisms on the transport properties of
$InAs_{1-x}P_x$ will be considered. For most of the calculations
presented here only the theory pertinent to $InAs_{0.61}P_{0.39}$
will be shown since the greater portion of the samples
studied in this work were of that composition. Comparisons
of the theory to experimental data will be made later when
the results are presented in Chapter IV and V.

2.1a Optical Phonon Scattering

The effects of optical phonons in a compound semi-conductor are twofold, and their strength is dependent upon the nature of the bonding between the atoms. In a crystal dominated by ionic bonds, the opposing motion of ions of opposite charge produce large polarization fields with which electrons strongly interact. However, a less mention-ed effect becomes more important in semiconductors with covalent bonding. Because of the bonding, polarization is not seen but rather the crystal potential is perturbed by the optical phonons in a manner quite similar to acoustical phonons. Unfortunately, the strength of this perturbation is not known, and in the theoretical analysis it must be included as an unknown value. Ziman[12] has shown that at high temperatures the mobility limited by this process is quite similar in form to the mobility equa-tion derived from acoustical phonon scattering. The import-ance of this distinction between the two modes of scattering attributed to optical phonon scattering lies in the fact that the bonding in III-V compounds is neither totally cova-lent or totally ionic but falls somewhere in between those limits. The bonding scheme is certainly even more confused by the fact that this study deals with the ternary compound, $InAs_{1-x}P_x$. As an approximation, however, the contribution from polarization is considered dominant, and therefore only

polar optical phonon scattering will be presented here.

Analysis of electron scattering due to polar inter-
action is complicated by the fact that the approximation
of a relaxation time is only valid when the energy emitted
or absorbed by an electron in a collision is small compared
to the initial energy of the electron. This is true when
the condition

$$(\theta_D/T)^2 \ll 1 \tag{2.1}$$

is satisfied. This, as will be seen shortly, is certainly
not the case for $InAs_{1-x}P_x$ at room temperature or below.

The first correct treatment of this problem was done
by Howarth and Sondheimer,[13] and although some authors[14,15]
have modified their theory[13] to account for special cases,
it is generally in close agreement with experimental data.
From the results of their complex mathematical treatment,
the mobility due to polar optical scattering may be written
as

$$\mu_0 = 3.54 \times 10^{40} \left(\frac{e}{e_c^*}\right)^2 \left(\frac{m_0}{m^*}\right)^{3/2} MvT^{1/2} \theta_D F\left(\frac{\theta_D}{T}\right) \left[\exp\left(\frac{\theta_D}{T}\right) - 1\right], \tag{2.2}$$

where e_c^* is the effective charge, m^* is the effective mass,
and v is the volume of the unit cell. The term M is the
reduced mass of the atoms given by

$$M = \frac{M_1 M_2}{M_1 + M_2} . \tag{2.3}$$

For the case of $InAs_{1-x}P_x$, the M_2 was taken to be a linear
interpolation between the mass of an arsenic atom and the
mass of a phosphorus atom. The function $F\left(\frac{\theta_D}{T}\right)$ is a slowly

varying function which decreases from unity at high temperatures to a minimum of 0.6 when $\theta_D = T$, and then increases steadily with $\frac{\theta_D}{T}$. A graph of this function is shown in Fig. 2.1. The Debye temperature, θ_D, is characteristic of the material and is relatively constant at room temperatures but decreases with decreasing temperature. The values for these parameters are listed in Table 2.1 for InAs, InP, and $InAs_{0.61}P_{0.39}$. The Debye temperature for $InAs_{0.61}P_{0.39}$ is shown in Fig. 2.2 from a linear interpolation of curves given for InAs and InP by Willardson and Beer.[16] Equation 2.2 is plotted versus inverse absolute temperature in Fig. 2.3 for InAs, InP, and $InAs_{0.61}P_{0.39}$. It is useful to note that the theoretical mobility due to polar optical scattering shown in Fig. 2.3 may be closely approximated by a power function in this temperature region. For the three compositions shown the following temperature dependences result:

$$
\begin{array}{ll}
InAs & \mu \propto T^{-2.20} \\
InAs_{0.61}P_{0.39} & \mu \propto T^{-2.28} \\
InP & \mu \propto T^{-2.42}
\end{array}
$$

These are necessarily the strongest dependences allowable in this region. Any other scattering mechanisms interacting with polar optical phonons will decrease the mobility and decrease its temperature dependence as will become evident when ionized impurity scattering is considered.

2.1b Ionized Impurity Scattering

Scattering of electrons by ionized impurity centers is in general more effective than phonon scattering, because
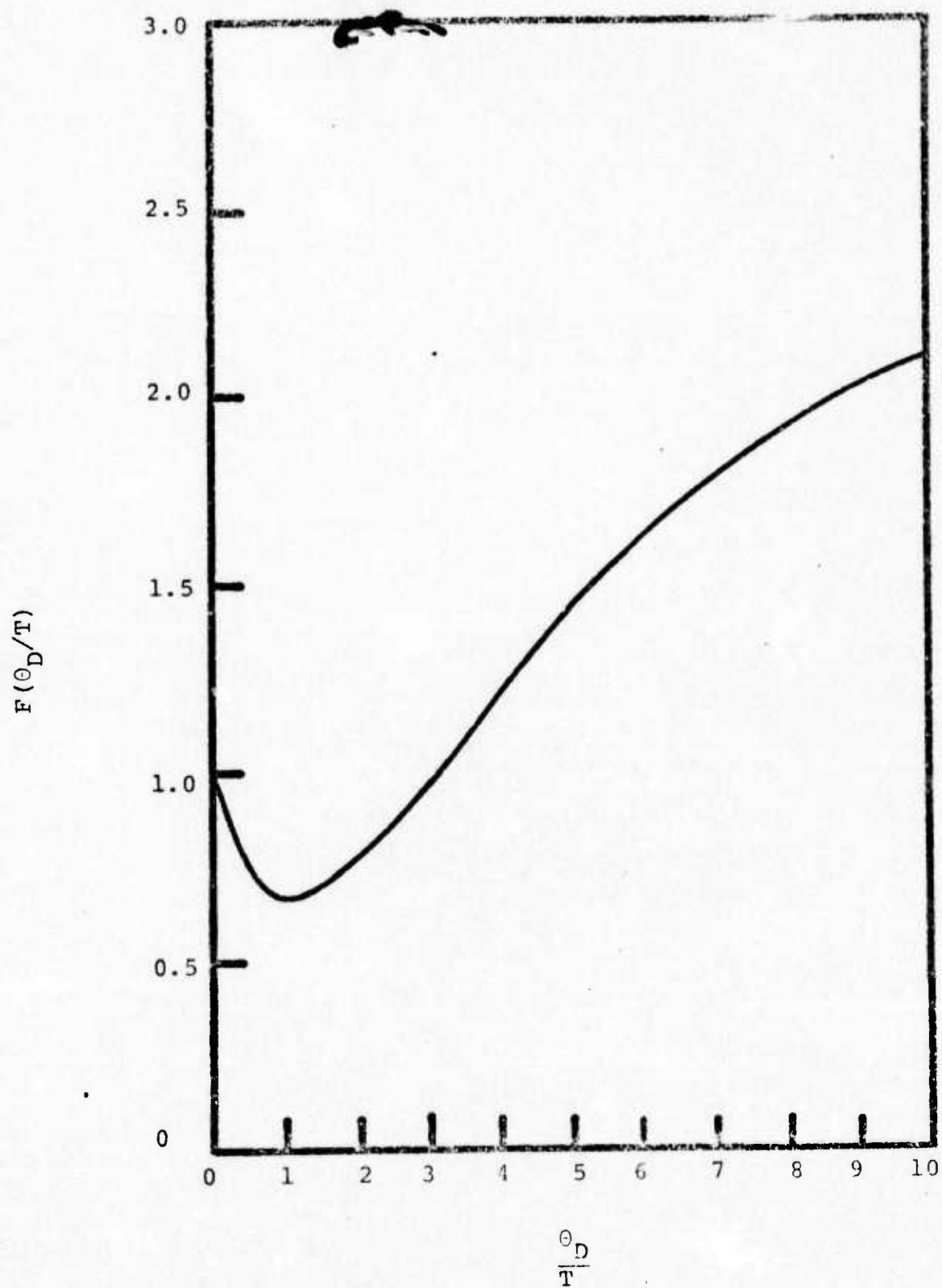
FIGURE 2.1 VARIATION OF THE FUNCTION $F(\Theta_D/T)$

TABLE 2.1

PARAMETERS FOR $InAs_{1-x}P_x$

	InAs	$InAs_{0.61}P_{0.39}$	InP
$\frac{e_c^*}{e}$	0.22	0.2278	0.24
$\frac{m^*}{m_0}$	0.02	0.0408	0.073
V	$2.217 \times 10^{-22} \, cm^3$	$2.143 \times 10^{-22} \, cm^3$	$2.020 \times 10^{-22} \, cm^3$
M	$7.527 \times 10^{-23} \, g$	$6.375 \times 10^{-23} \, g$	$4.050 \times 10^{-23} \, g$
κ	11.5	11.26	10.9

FIGURE 2.2   VARIATION OF DEBYE TEMPERATURE WITH
ABSOLUTE TEMPERATURE

FIGURE 2.3 MOBILITY LIMITED BY POLAR OPTICAL PHONON
SCATTERING PLOTTED LOG-LOG VERSUS INVERSE
ABSOLUTE TEMPERATURE

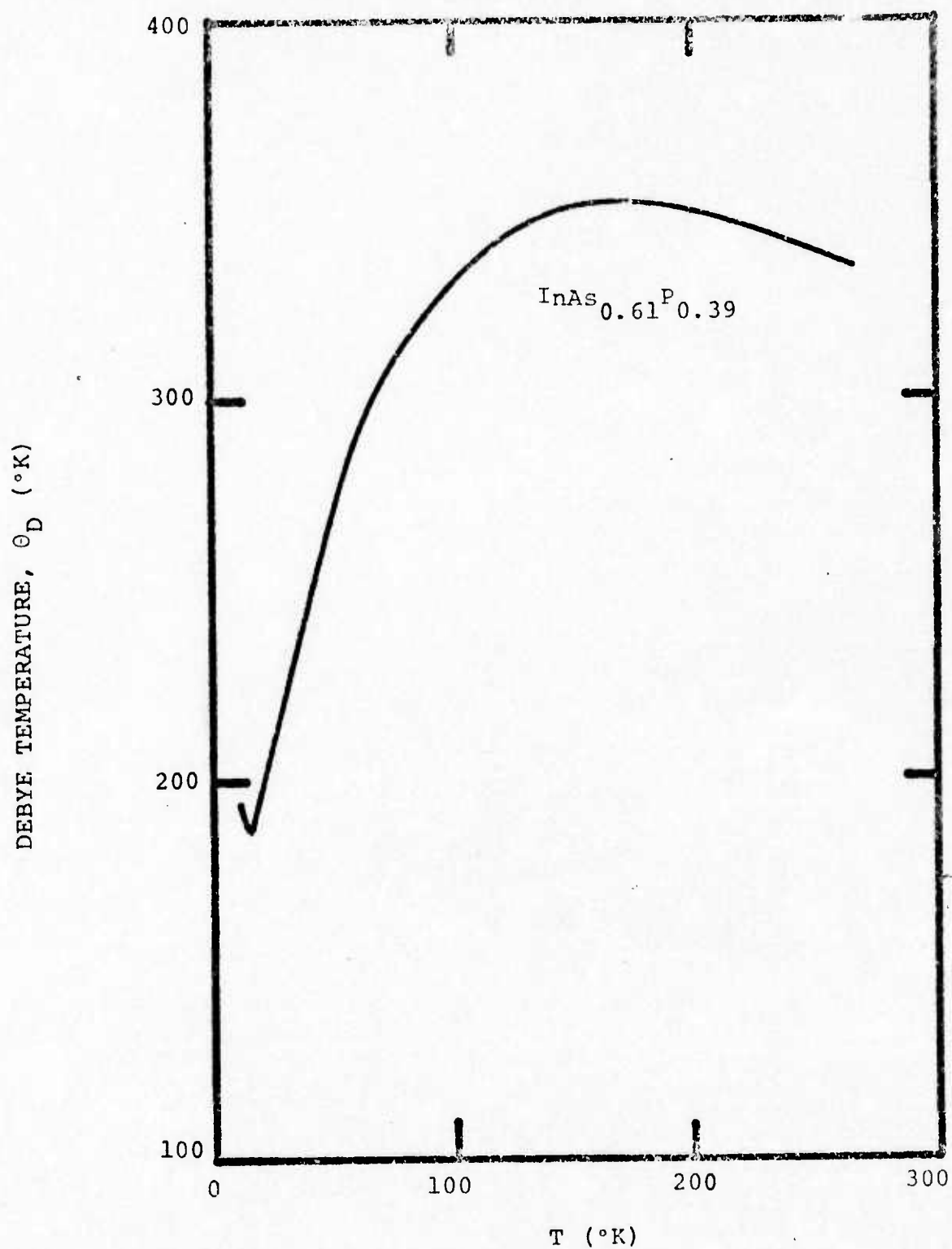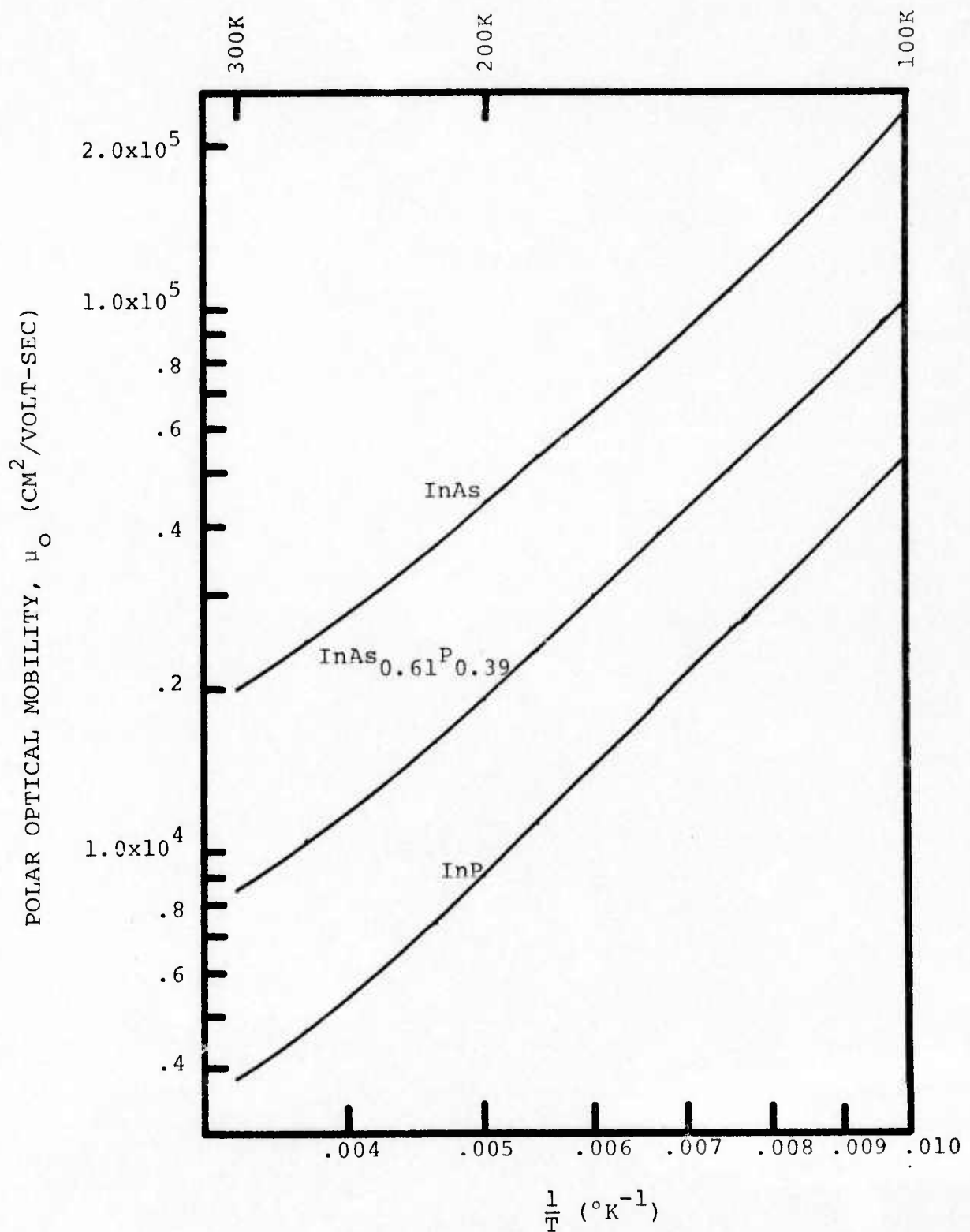of the electric charge associated with each impurity. The
perturbing potential is normally assumed to be equal to
the charge difference between the valence of the impurity
atom and the crystal atom which it replaced. Thus an elec-
tron will interact with this perturbing potential and be
scattered by the Coulomb field.

Conwell and Weisskopf[17] treated scattering due to
ionized impurities in an essentially classical manner. Each
ion was assumed to scatter independently of each other but
with its scattering strength truncated in the calculations
at a distance equal to half the average distance between
the ionized impurities. This assumption is somewhat justi-
fied by the screening effect of conduction electrons on the
impurities. The result of their analysis gives a mobility
limit due to ionized impurities in the form

$$\mu_i = \frac{2^{7/2}}{\pi^{3/2}} \frac{\kappa^2 (kT)^{3/2}}{m^{*1/2} e^3 N_i} \frac{1}{\ln\left[1+(3\kappa kT/e^2 N_i^{1/3})^2\right]} , \tag{2.4}$$

where κ is the effective dielectric constant, m^* is the
effective mass and N_i is the concentration of ionized im-
purities.

A quantum-mechanical approach by Brooks[18] takes into
account the effects of screening by the conduction electrons.
The results of this treatment give a mobility which is
identical to that of Conwell and Weisskopf except for an
alteration in the logarithmic term.

$$\mu_i = \frac{2^{7/2}}{\pi^{3/2}} \frac{\kappa^2 (kT)^{3/2}}{m^{*1/2} e^3 N_i} \frac{1}{f(b)} \tag{2.5}$$

$$f(b) = \ln(1+b) - \frac{b}{1+b} \tag{2.6}$$

$$b = \frac{24\pi\kappa m^* k^2 T^2}{nh^2 e^2} \tag{2.7}$$

In Eqn. 2.7, n is the concentration of conduction electrons.

These two forms for the mobility due to ionized impurity scattering, though derived from somewhat different principles, have basically the same form and for temperatures between 300 and 78K have been shown[19] to give almost identical numerical results for germanium. This close correspondence between the two equations was verified for the ternary semiconductor, $InAs_{1-x}P_x$, presented in this work. In most experimental semiconductor work, especially with silicon or germanium, the Brooks-Herring formula, Eqn. 2.5, is used to describe the region of mobility controlled by ionized impurities. However, due to the closeness of the results of the Conwell-Weisskopf formula and in light of some assumptions to be presented later, Eqn. 2.4 will be used here to describe this scattering process.

The Conwell-Weisskopf formula may be expressed in practical MKS units as

$$\mu_i = 3.286 \times 10^{15} \frac{\kappa^2 T^{3/2}}{m^{*1/2} N_i} \frac{1}{\ln[1+(1.795\times10^3 \frac{kT}{N_i^{1/3}})]^2} \tag{2.8}$$

where N_i is expressed in cm^{-3}. Equation 2.8 was combined

with the mobility due to polar optical phonon scattering, Eqn. 2.2, using the relation[20]

$$\mu_{0-i}^{-1} = \mu_0^{-1} + \mu_i^{-1} \tag{2.9}$$

The results of this combination for $InAs_{0.61}P_{0.39}$ are shown in Fig. 2.4 for varying concentrations of ionized impurities N_i. From these curves it may be seen that as the ionized impurity concentration increases the maximum of the mobility curves shift to higher temperatures. The initial slopes of the curves at 300K decrease with increasing impurity concentration. As was indicated in the discussion of optical phonon scattering, this portion of the curve dominated by optical phonons may be approximated by the equation

$$\mu = aT^{-\beta} \tag{2.10}$$

The power of temperature dependence, β, is then shown in Fig. 2.5 as a function of the ionized impurity concentration. This curve will serve later as a useful indicator of the impurity content of the samples studied by calculating the temperature power dependence of the experimental data near 300K and comparing that to Fig. 2.5.

2.1 c Neutral Impurity Scattering

A third important source of electron scattering is due to the effects of neutral impurities. This type of scattering is most effective at low temperatures where most semiconductors exhibit only a small degree of ionization. It
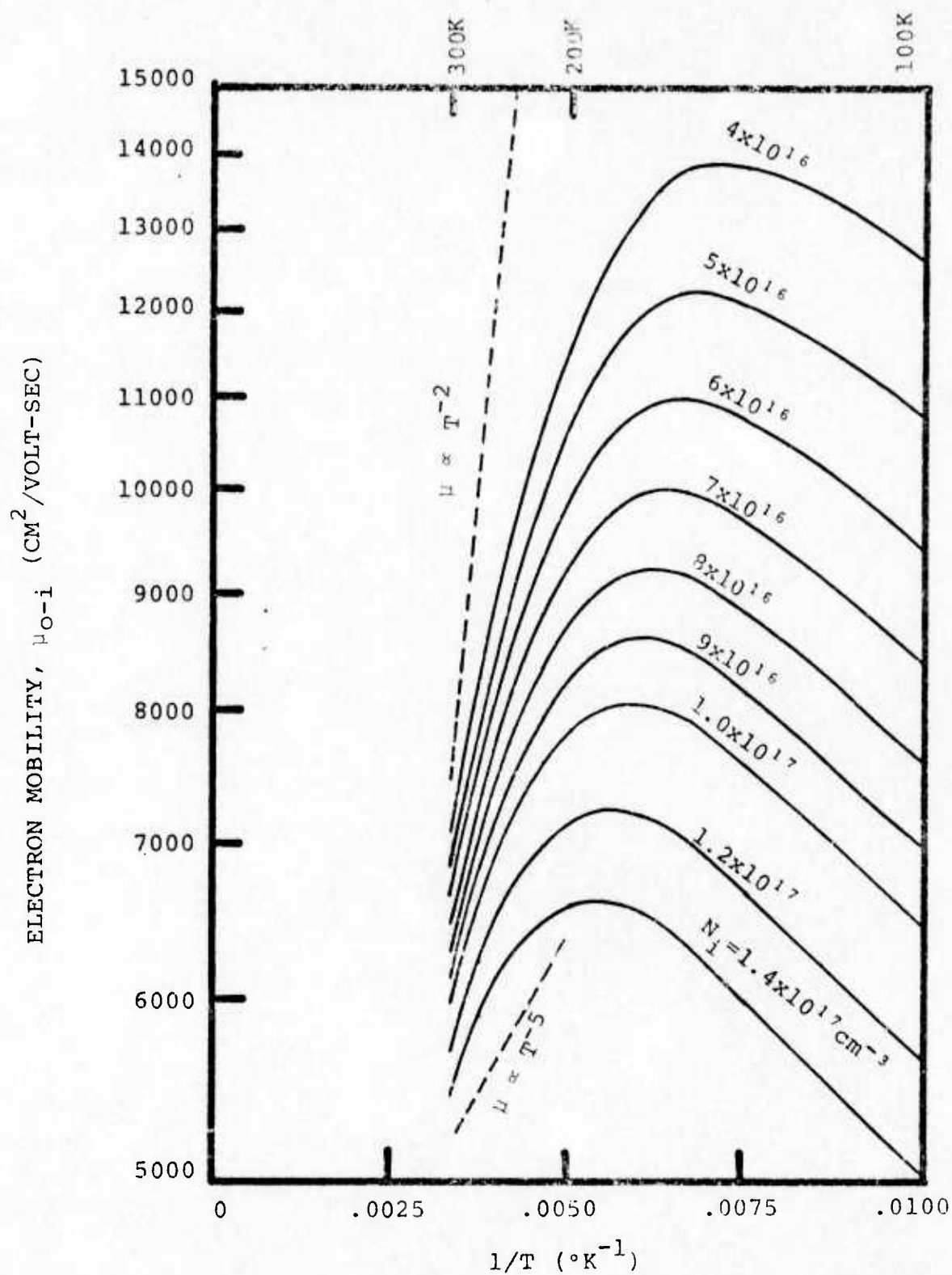
FIGURE 2.4   COMBINED MOBILITY LIMITS DUE TO POLAR
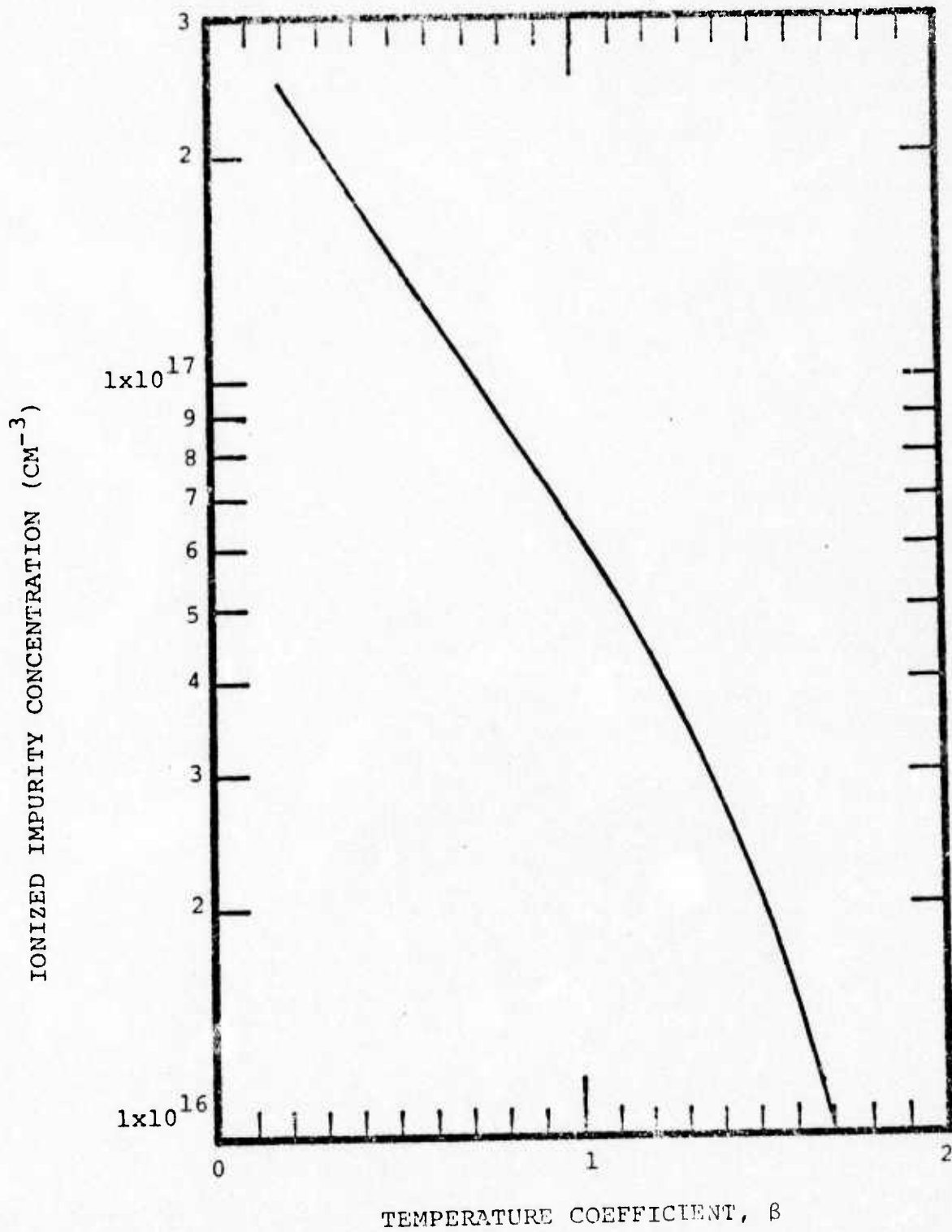OPTICAL PHONON AND IONIZED IMPURITY
SCATTERING FOR $InAs_{0.61}P_{0.39}$

FIGURE 2.5   VARIATION OF TEMPERATURE COEFFICIENT,
β, WITH IONIZED IMPURITY CONCENTRATION

may be comparable to scattering due to ionized impurities up to temperatures of around 100K.[21] Erginsoy[22] derived a theoretical model for this type of scattering by approximating an unionized donor or acceptor atom with a hydrogen atom. From this model, a mobility was derived which was temperature independent.

$$\mu_{ne} = \frac{1}{20} \; \frac{m^{*}e^{3}}{N_{n}\kappa h^{3}} \tag{2.11}$$

However, experimentally this temperature independence is not generally seen.[23] Erginsoy's theory was modified by Sclar[24] by including the possibility of bound states in the electron-hydrogen impurity scattering problem. His results were temperature dependent and the mobility from this theory may be expressed as

$$\mu_{n} = 0.82\mu_{ne} \left[2/3 \left(\frac{kT}{E_{n}}\right)^{1/2} + 1/3 \left(\frac{E_{n}}{kT}\right)^{1/2} \right] \tag{2.12}$$

where μ_{ne} is given by Eqn. 2.11 and E_{n} is

$$E_{n} = 0.71 \left(\frac{m^{*}}{\kappa^{2}}\right) eV \tag{2.13}$$

For the case of $InAs_{0.61}P_{0.39}$, Eqn. 2.12 may be written as

$$\mu_{n} = (4.266 \times 10^{13}/N_{n}) \; [0.4095T^{1/2} + 0.5427/T^{1/2}] \tag{2.14}$$

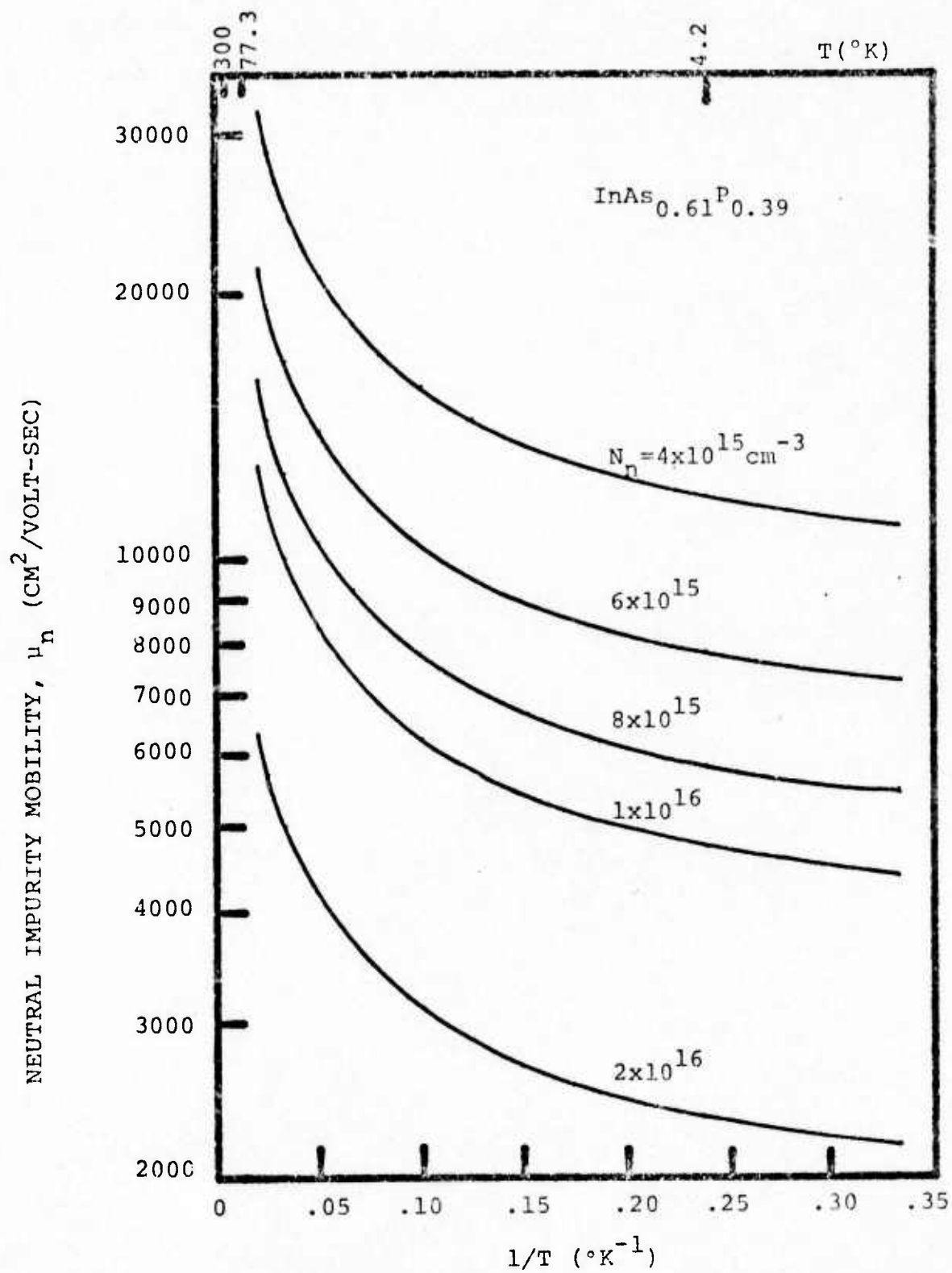The mobility computed from Eqn. 2.14 is shown in Fig. 2.6 as a function of inverse absolute temperature for different

FIGURE 2.6   MOBILITY LIMITED BY NEUTRAL IMPURITY
SCATTERING FOR InAs $_{0.61}$P$_{0.39}$

neutral impurity concentr. ons.

The mobility equations derived from polar optical scattering (Eqn. 2.2), ionized impurity scattering (Eqn. 3.8), and neutral impurity scattering (Eqn. 2.14) were combined in a manner similar to Eqn. 2.9. The results for a constant neutral impurity content of $1 \times 10^{16} cm^{-3}$ and varying ionized impurity content are shown in Fig. 2.7. If these are the three dominant scattering mechanisms and if the assumptions involved with each of their derivations are valid,   then these theoretical curves should be indicative of what might be expected experimentally for $InAs_{0.61}P_{0.39}$.

2.1d Electron-Electron Collisions

There are many other sources of electron scattering which tend to further limit and vary the shape of the mobility curves. These will not, however, be considered in this discussion since their effects are considered small or negligible in $InAs_{1-x}P_x$. One important source of scattering, though, should be presented at least in a qualitative fashion. This is the interaction of conduction electrons with other conduction electrons which will serve to increase the effectiveness of energy-dependent scattering mechanisms such as ionized impurity scattering.

The effect of electron-electron collisions may be understood by considering an electron current density distributed initially over a certain energy range. Upon encountering an energy-dependent scattering mechanism, such as an ionized
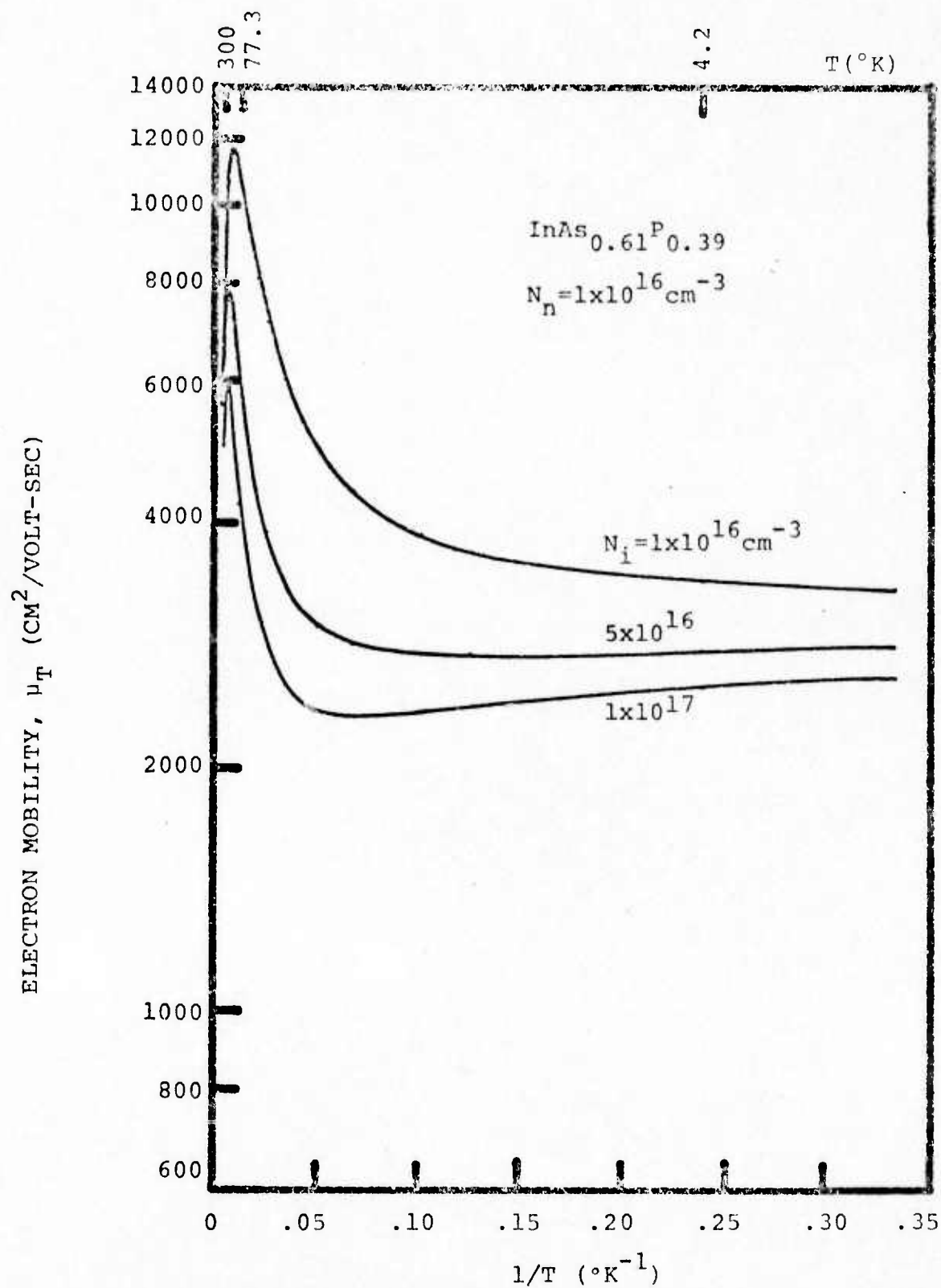
FIGURE 2.7 COMBINED THEORETICAL MOBILITIES
FOR InAs$_{0.61}$P$_{0 39}$

impurity, those electrons r. lower energy, thus lower velocity, will be affected more than the electrons of higher energy. Thus the momentum transfer to the mechanism will be due mostly to low energy electrons resulting in a non-uniform energy distribution among the electrons. Electron-electron collisions will not in themselves result in a change in the total momentum but will serve to redistribute that momentum, within the electron cloud, to the lower energy electrons. This results in a more efficient mechanism for momentum transfer to the scatterers and thus a lower mobility. The effect of electron-electron collisions is then dependent upon the degree to which the scattering mechanism is energy dependent. Its greatest effect is with ionized impurity scattering and has been shown[25] to have a possible effect of reducing the mobility from this source by a factor of 0.6, although this is not normally realized. In the case of $InAs_{1-x}P_x$, electron-electron collisions would tend to reduce the maximum peaks of the mobility curves shown in Fig. 2.7

2.2 Band Conduction

There are two sources of electrons in a semiconductor. In the case of intrinsic conduction, electrons are excited into the conduction band from the valence band. In the case of extrinsic conduction, electrons are excited from donor levels into the conduction band. Three cases will be considered here. First, the possibility of

irtrinsic conduction will be considered briefly Second, the effects of donor levels with compensating acceptor levels will be shown. Last, the consequences of high donor concentration and the formation of an impurity band will be discussed.

2.2a Intrinsic Conduction

Intrinsic conduction is a property of an ideally pure semiconductor or of the case when the electrons or holes excited from the impurity levels are negligible compared to n_i, the concentration of electrons excited from the valence band into the conduction band. In an ideally pure semi-conductor at absolute zero the valence band is completely filled and the conduction band, separated from the valence band by an energy gap, E_g, is completely empty. As the temperature is raised the electrons may gain enough thermal energy to break their bonds and be excited into the conduction band. The result is electrons which are free to propagate in the conduction band and corresponding holes which are capable of conduction within the valence band. It may be shown that the number of carriers in either band may be expressed as a function of absolute temperature by the relation[28]

$$n_i = 2(2\pi kT/h^2)^{3/2} (m_e^\star m_h^\star)^{3/4} \exp(-E_g/2kT) \qquad (2.15)$$

In realistic crystals, the conduction electron concentration is dominated by intrinsic conductors when either Eg is small

or at high temperatures because of the exponential term in
Eqn. 2.15. The effect of intrinsic conduction on $InAs_{0.61}P_{0.39}$,
with an energy gap of 0.705eV at room temperature, may be
seen by substitution of the appropriate values into Eqn. 2.15.

$$n_i = 4.827 \times 10^{15} T^{3/2} (m_e^* m_n^*)^{3/4} \exp\left(\frac{3.7 \times 10^{-4} T - .816}{2kT}\right) \qquad (2.16)$$

The density of intrinsic carriers for $InAs_{0.61}P_{0.39}$ and also
for InAs and InP is shown in Fig. 2.8 where it is seen that
for temperatures below room temperature this density is very
low especially as the content of phosphorus increases.

2.2b Conduction Due to Compensated Donors

In practical semiconductors, unless extreme caution is
taken in their growth and purification, the conduction electrons
are excited from donor states rather than from the top of the
valence band. Typically there are numerous types of impurity
atoms creating states within the forbidden energy gap between
the valence and conduction bands. For simplicity, however,
only a single shallow donor level and a single deep-lying
acceptor level will be considered here. An idealized diagram
of the energy states characterizing this condition is shown
in Fig. 2.9. It is assumed that the donor density, N_d, is
greater than the acceptor density, N_a.

At temperatures somewhat below the onset of intrinsic ion-
ization, it is reasonable to assume that all states in the
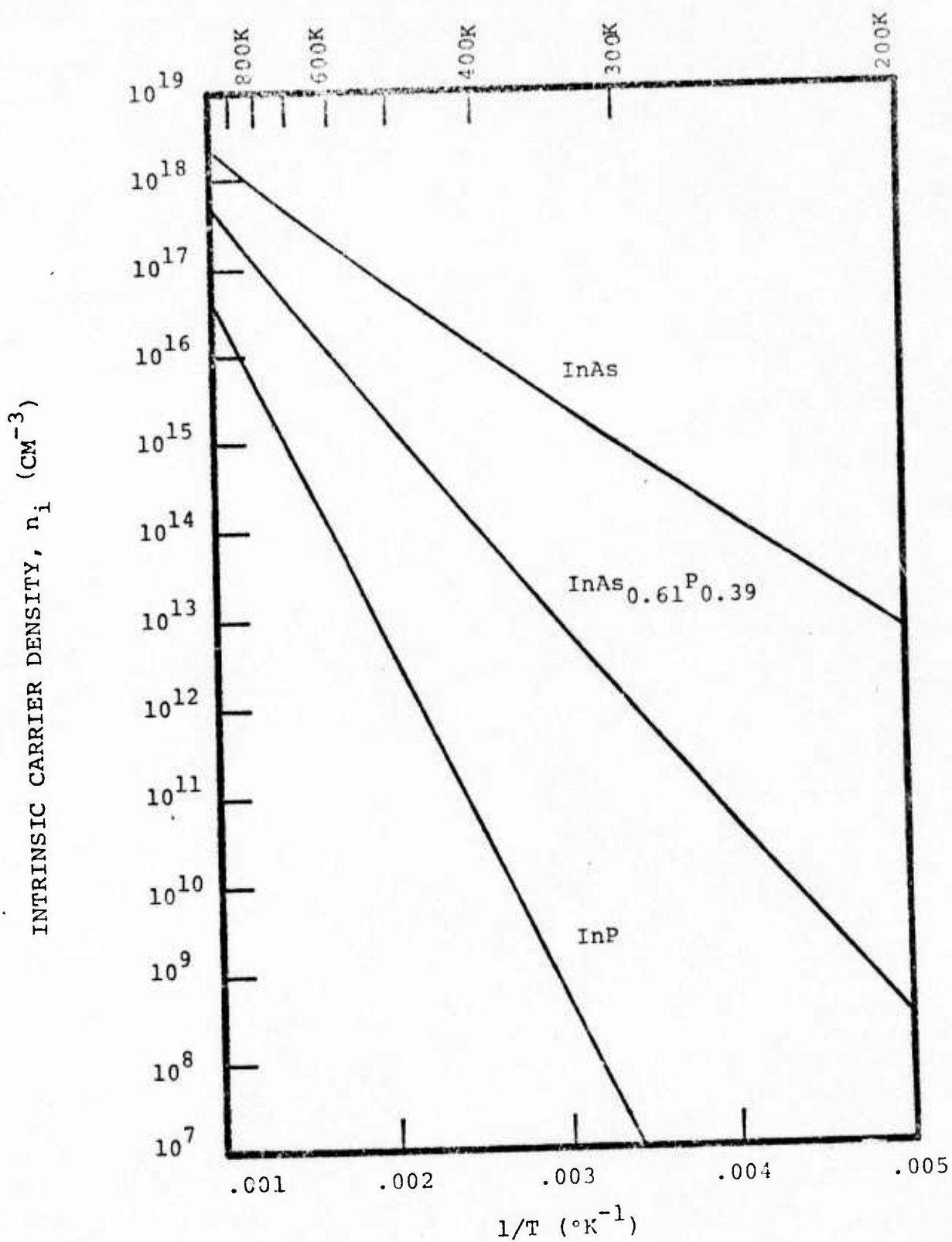valence band are filled and all acceptor levels are also

FIGURE 2.8   INTRINSIC CARRIER DENSITY WITH
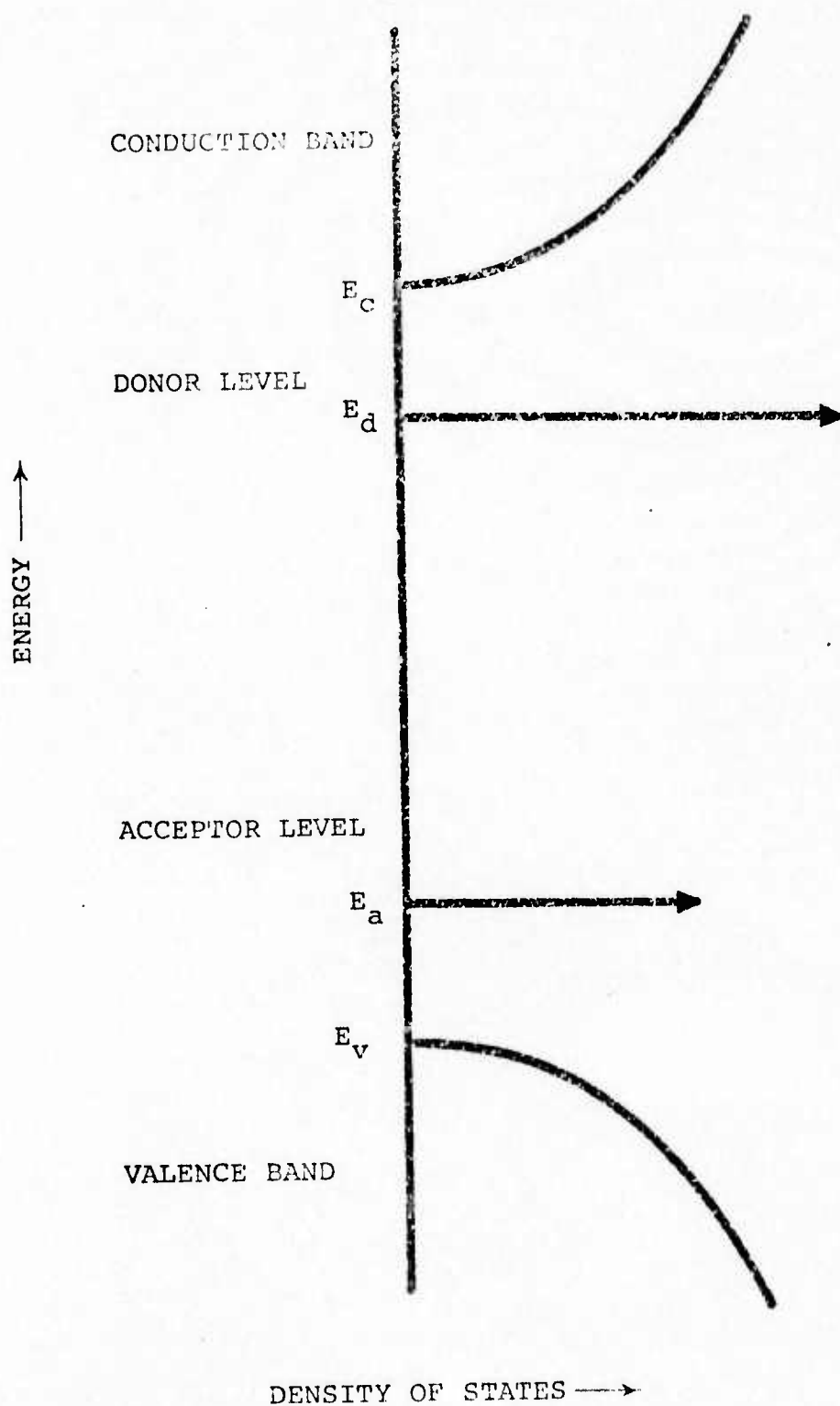INVERSE ABSOLUTE TEMPERATURE

FIGURE 2.9   IDEALIZED DENSITY OF STATES DIAGRAM

filled (ionized). The electrons needed to fill these acceptor states necessarily are drawn from the donor impurities. The donor level is then said to be "compensated" since this leaves only $N_d - N_a$ electrons available to be excited into the conduction band. The conduction electron concentration may be written as

$$n_c = N_d - N_d^o - N_a \qquad (2.17)$$

where N_d^o is the number of unionized or neutral donors. This is given by

$$N_d^o = \frac{N_d}{1 + g \ exp\left[\frac{E_d - E_f}{kT}\right]} \qquad (2.18)$$

where g is the degeneracy factor for the donor level. The number of ionized donors may be found from Eqn. 2.18 and the relation

$$N_d^+ = N_d - N_d^o \qquad (2.19)$$

with the result

$$N_d^+ = \frac{N_d}{1 + g^{-1} \ exp\left[-\frac{E_d - E_f}{kT}\right]} \qquad (2.20)$$

Now assuming that the Fermi level is at least a few kT beneath the conduction band, the conduction electron density may be expressed using Boltzmann statistics as

$$n_c = N_c \exp \left(-\frac{E_c - E_f}{kT} \right) \qquad (2.21)$$

where N_c is the effective density of conduction states.

$$N_c = 2(2\pi m^* kT/h^2)^{3/2} \qquad (2.22)$$

$$N_c = 4.827 \times 10^{15} (m^*)^{3/2} T^{3/2} \qquad (2.23)$$

$$N_c = 3.978 \times 10^{13} T^{3/2} \text{ for InAs}_{0.61}P_{0.39} \qquad (2.24)$$

Equations 2.20 and 2.21 may then be manipulated[27] to obtain

$$\frac{n_c N_d^+}{N_d - N_d^+} = \frac{n_c(n_c + N_e)}{N_d - N_a - n_c} = g N_c \exp \left(-\frac{E_c - E_d}{kT} \right) \qquad (2.25)$$

Milnes[28] has shown that this may be manipulated into a useful expression for the conduction electron density in terms of N_a, N_d and T.

$$n_c = \frac{2(N_d - N_a)}{\Psi + [\Psi^2 + \frac{4(N_d - N_a)}{gN_c} \exp \left(\frac{E_c - E_d}{kT} \right)]^{1/2}} \qquad (2.26)$$

where

$$\Psi = 1 + \frac{N_a}{gN_c} \exp \left(\frac{E_c - E_d}{kT} \right) \qquad (2.27)$$

For low compensation ($N_a \sim 0$), n_c reduces to

$$n_c = \frac{2N_d}{1 + [1 + (4N_d/gN_c) \exp \left(\frac{E_c - E_d}{kT} \right)]^{1/2}} \qquad (2.28)$$

For high compensation

$$n_c \simeq \frac{N_d - N_a}{\psi}$$ (2.29)

Equation 2.26 is plotted in Fig. 2.10 for a donor density
of $5 \times 10^{16} \text{cm}^{-3}$ with varying amounts of compensation from a
deep acceptor level. The effective density of states is
from Eqn. 2.24 and the donors are considered to lie at
4.29meV beneath the conduction band edge with a degeneracy
of g=2. From the curves it is seen that the slopes are
nearly exponential, especially below room temperature, and
the slopes increase with increasing compensation. It may
be shown that increasing the donor concentration will also
result in an increase of the slopes.

2.2c Conduction in the Impurity Levels

The discussion to this point has dealt with electrons
excited from either the valence band or from donor states
into the conduction band where the continuum of empty energy
states permits conduction within the semiconductor. It has
been shown that for temperatures below 300K the main source
of electrons is from the donor impurities. The results of
Eqn. 2.26 shown in Fig. 2.10 indicate that as the temperature
decreases there is an exponential decrease of carriers in the
conduction band which would imply that at very low temperatures
few electrons would be available for conduction and both the
resistivity and Hall coefficient would become infinitely large
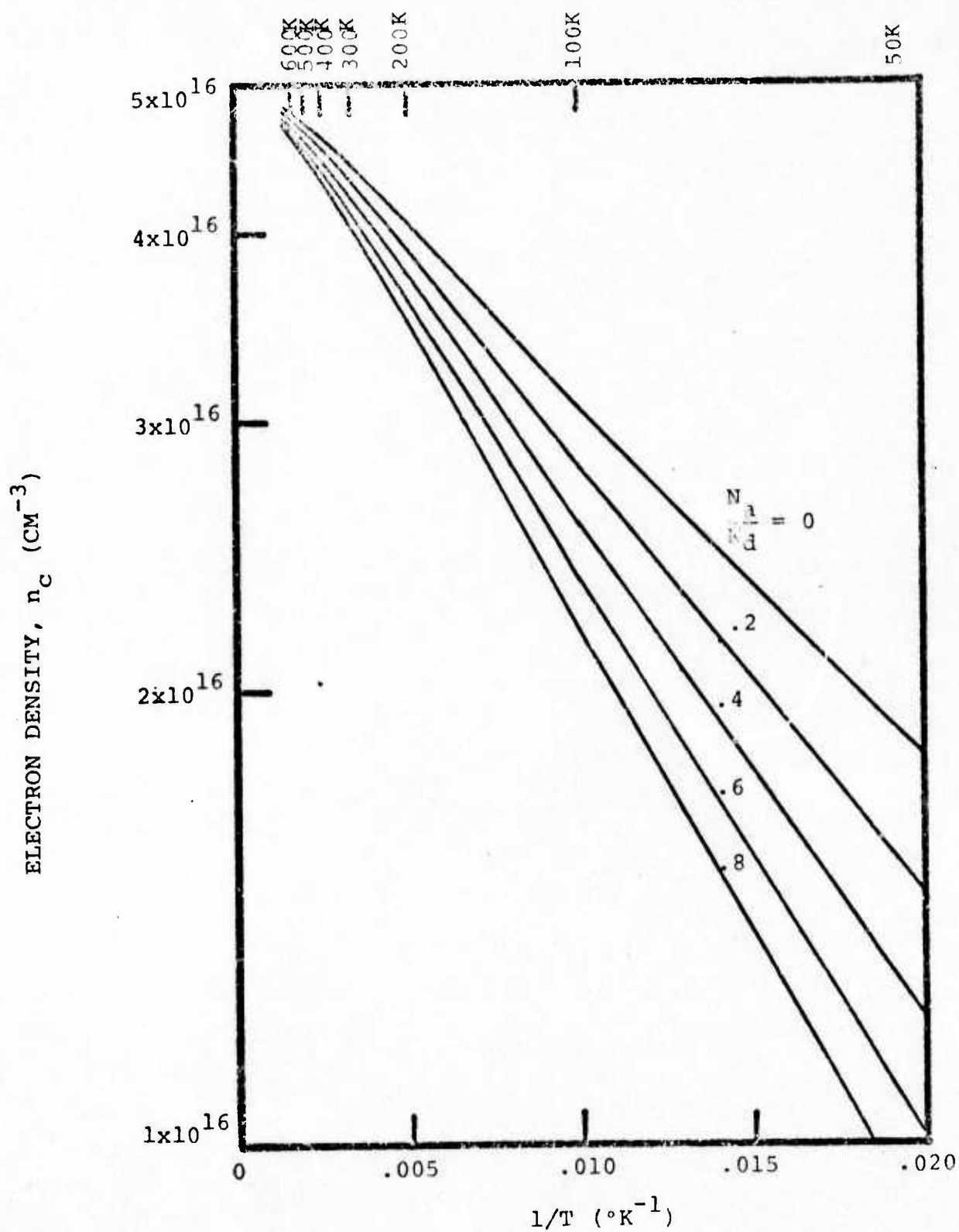near absolute zero. Experimental evidence, however, does not

FIGURE 2.10   COMPENSATION EFFECT ON CONDUCTION
BAND ELECTRONS

always support these predictions. Several investigators[29,30,31] have found that in some samples as the temperature decreases there is an initial decrease in carrier concentration but at some low temperature the carrier concentration begins to rise until it approaches a constant level at the lowest temperatures.

The basic assumption of the carrier statistics presented in Section 2.2b was that the donors were thought to lie at a single energy level implying that the impurities are completely localized states. As the concentration of donor impurities increase, i.e. the average distance between impurity ions decreases, the wave functions of the impurities begin to overlap and the donor states lose their localized nature. Baltensperger[32] has determined the energy band formation for impurities assumed to be in a regular periodic lattice structure. The results of his calculations were presented by Conwell[33] as a function of r_s/a_h^* where r_s is the distance between impurities:

$$r_s = \left(\frac{3}{4\pi N_i}\right)^{1/3} \tag{2.30}$$

and a_h^* is the first Bohr orbit for an electron of mass m^*:

$$a_h^* = \frac{0.53\kappa}{m^*} \, \overset{\circ}{A} \tag{2.31}$$

which for $InAs_{0.61}P_{0.39}$ is $a_h^* = 146.3\overset{\circ}{A}$. The results for the energy levels versus impurity spacing are shown in Fig. 2.11 with a lower abscissa scale added to show corresponding impurity
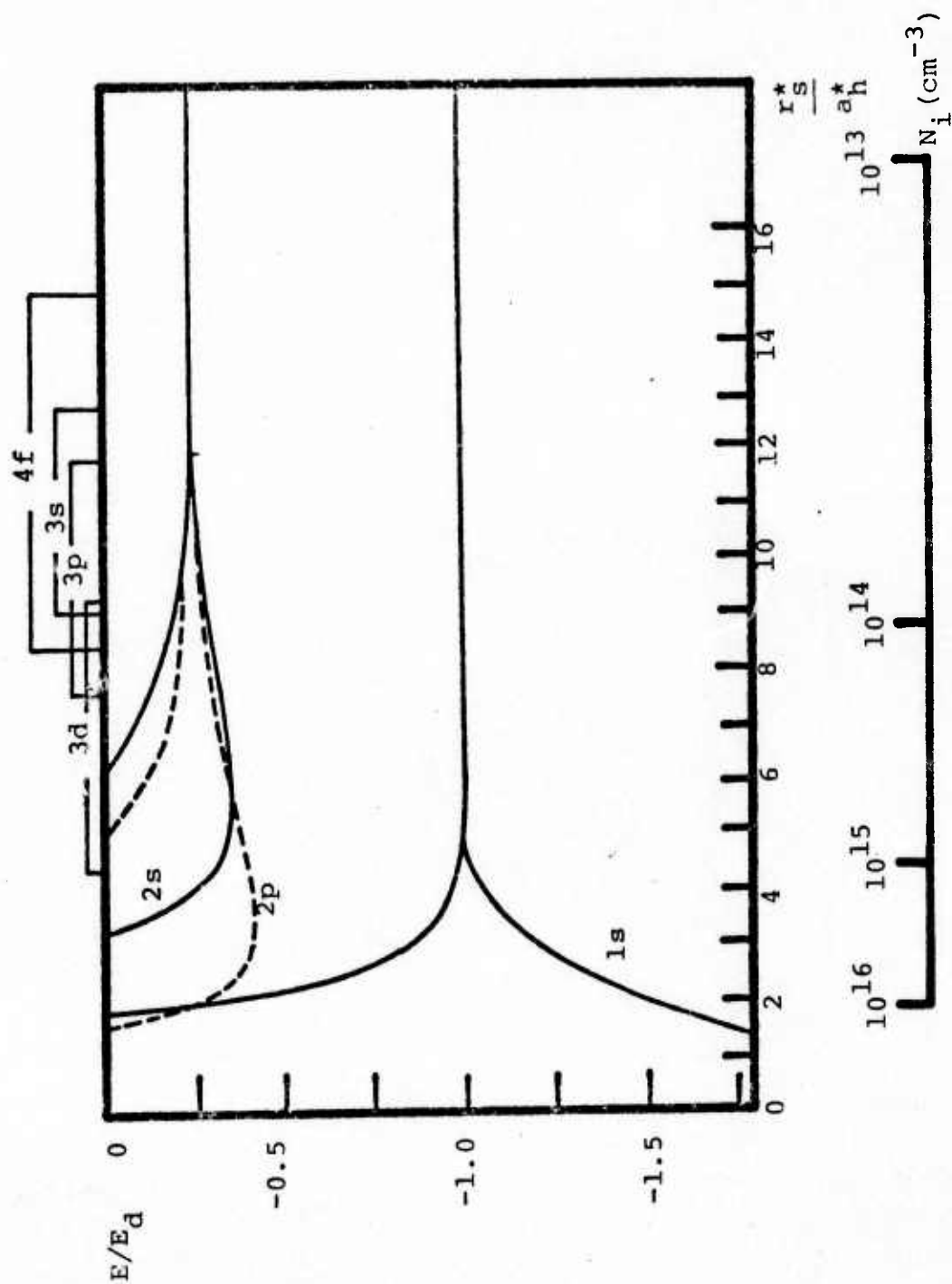
FIGURE 2.11 BAND FORMATION AS A FUNCTION OF THE AVERAGE DISTANCE
BETWEEN IMPURITIES. $E/E_d = 0$ INDICATES OVERLAP WITH
CONDUCTION BAND

concentrations for $InAs_{0.61}P_{0.39}$. At large r_s there is a complete set of discrete energy levels. As the distance decreases, successively lower excited levels overlap and form bands. At $r_s \sim 5 a_h^*$ the ground state begins to spread resulting in the impurity band.

The term 'band' has been used quite freely and although somewhat descriptive of the actual physical situation, it is somewhat misleading. The implication from the term and the foregoing discussion is that the impurity atoms enter the lattice in a regular periodic fashion. This is not justifiable. In fact, it is the randomness of the impurity atoms that has been one of the major barriers to the development of a working theory to describe this phenomenon. The result of this random nature is a band centered about the single state impurity level, E_d. The distribution of states about this level is usually considered to be gaussian with long tails to both low and high energies.[34,35] A band diagram descriptive of the results of an impurity band formation is given in Fig. 2.12. The perturbation (band tail) of the conduction band edge is also a result of the impurities in that they are a disruption to the periodicity of the original crystal structure. The acceptor levels are also portrayed in a gaussian fashion, but this is inconsequential if those levels are considered deep.

Now that an argument has been established for an impurity band it is essential that it contain empty states to account for conduction within that band. Certainly the presence of
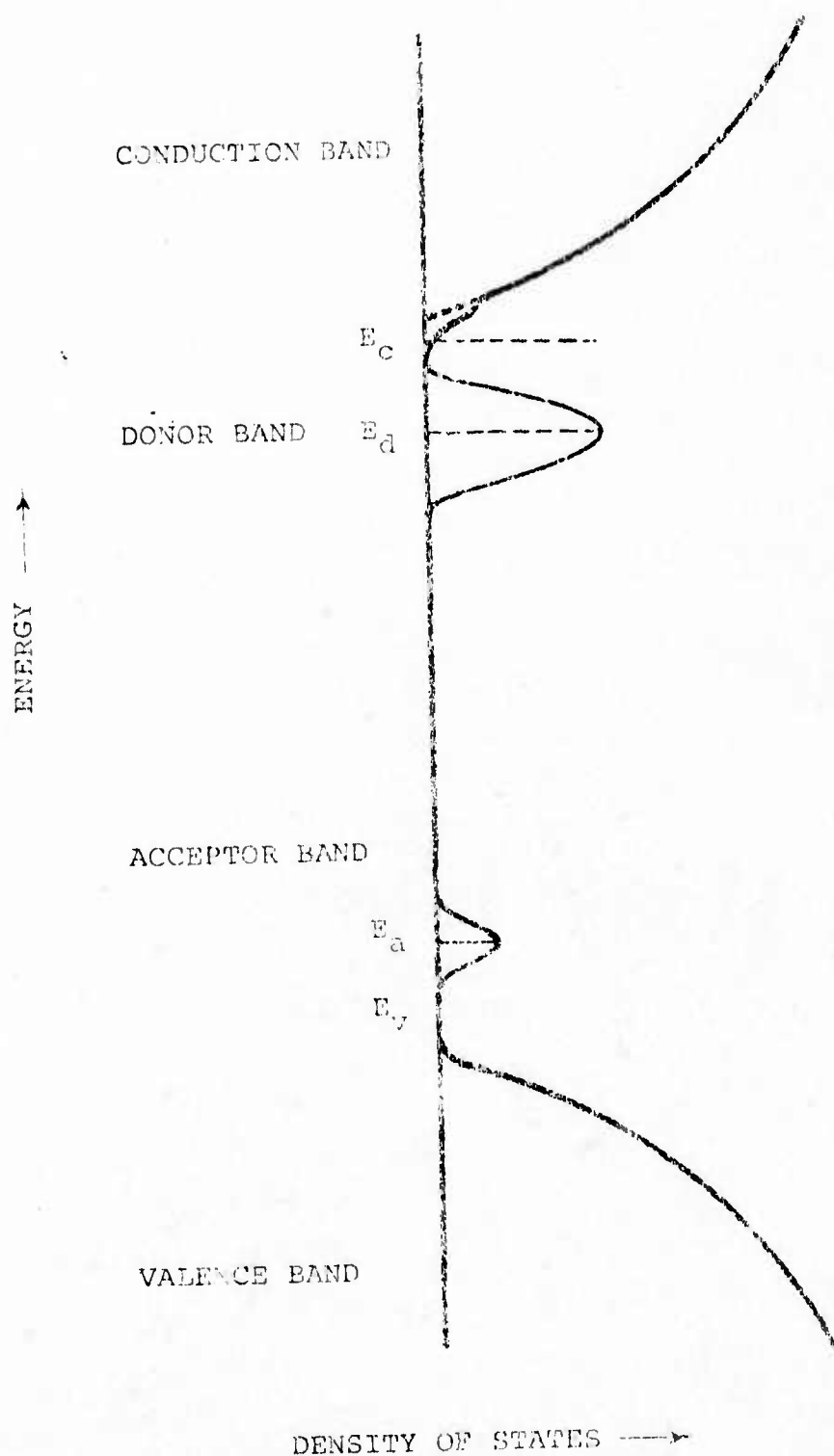
33

FIGURE 2.12 REALISTIC DENSITY OF STATES DIAGRAM

acceptor states will compensate some of the donors but a more basic argument may be made stemming from the difference between a set of discrete levels and a band. In a localized energy state there are two possible ways for an electron to occupy it due to spin degeneracy. This was taken into account in Eqn. 2.26 when the degeneracy factor g=2 was used. With localized states when one spin state is occupied the other state may not be. However, when a band is formed the states are no longer associated with individual atoms so that it may not be known if both spin states of an individual atom are filled or not. Thus in the donor band this results in $2N_d$ states available for occupancy. At absolute zero then, with all the acceptor states filled from the donor levels, there are $N_d + N_a$ empty states in the donor band in which electrons may easily move.

The result of conduction within the donor band has certain consequences. The total number of electrons available for conduction is now constant at $N_d - N_a$. At high temperatures these are all in the conduction band and at absolute zero they are all in the donor band. In the intermediate temperature range, conduction occurs in both bands. The total conductivity is given by[36]

$$\sigma = n_c e \mu_c + n_d e \mu_d \qquad (2.32)$$

and assuming that Hall coefficient expression for intrinsic

conduction may be adapted for this case

$$R_h = \frac{r}{e} \frac{n_c \mu c^2 + n_d \mu d^2}{(n_c \mu_c + n_d \mu_d)^2} \qquad (2.33)$$

The total carrier concentration is

$$n_t = n_c + n_d = N_d - N_a \qquad (2.34)$$

A maximum in the Hall coefficient occurs when

$$n_c \mu_c = n_d \mu_d \qquad (2.35)$$

If the mobility in both the conduction band and donor band are considered to have the same temperature dependence, that is

$$b = \frac{\mu_c}{\mu_d} = \text{constant} \qquad (2.36)$$

then the relationship for $R_{h_{max}}$ may be derived as

$$\frac{R_{h_{max}}}{R_{h_{exh}}} = \frac{(b+1)^2}{4b} \qquad (2.37)$$

$R_{h_{exh}}$ is the Hall coefficient in the exhaustion region and the scattering coefficient is assumed to be unity at all temperatures. It may also be shown[37] from these assumptions that

$$\frac{R_h}{R_{h_{exh}}} = \frac{(x+b^2)(x+1)}{(x+b)^2} \qquad (2.38)$$

where

$$x = \frac{n_d}{n_c} \qquad (2.39)$$

The two relations of Eqns. 2.37 and 2.38 may be solved and from experimental data the concentrations of electrons in the two bands may be found, at least to an approximate degree. From the temperature dependence of electrons in the conduction band found in this manner, the activation energy of electrons may be determined. This will be shown later in Chapter IV.

CHAPTER III

EXPERIMENTAL PROCEDURES

3.1 Epitaxial Growth

The epitaxial samples used for this research were
grown by Dr. John K. Kennedy[38] using a hydride system
similar to Tietjen's. A diagram of the vapor system used
to grow the epitaxial samples is shown in Fig. 3.1. Hydro-
gen is used as the carrier gas and is divided equally be-
tween the HCl and the arsine (AsH_3) and phosphine (PH_3)
mixture. The total hydrogen flow rate controls the rate
of growth and is thus used as a variable for four sets of
samples investigated. As the HCl passes over the indium
boat it transports the indium in the form of a chloride
into the reaction zone where it mixes with the arsine and
phosphine. The high temperature of the reaction zone (950°C)
causes the decomposition of the hydrides into their respective
elements with a by-product of hydrogen. The deposition is
then completed on the substrate at a lower temperature (650-
675°C) in the deposition zone. This growth method allows the
ratio of As to P to be adjusted and maintained accurately
from sample to sample and might also be useful for composition
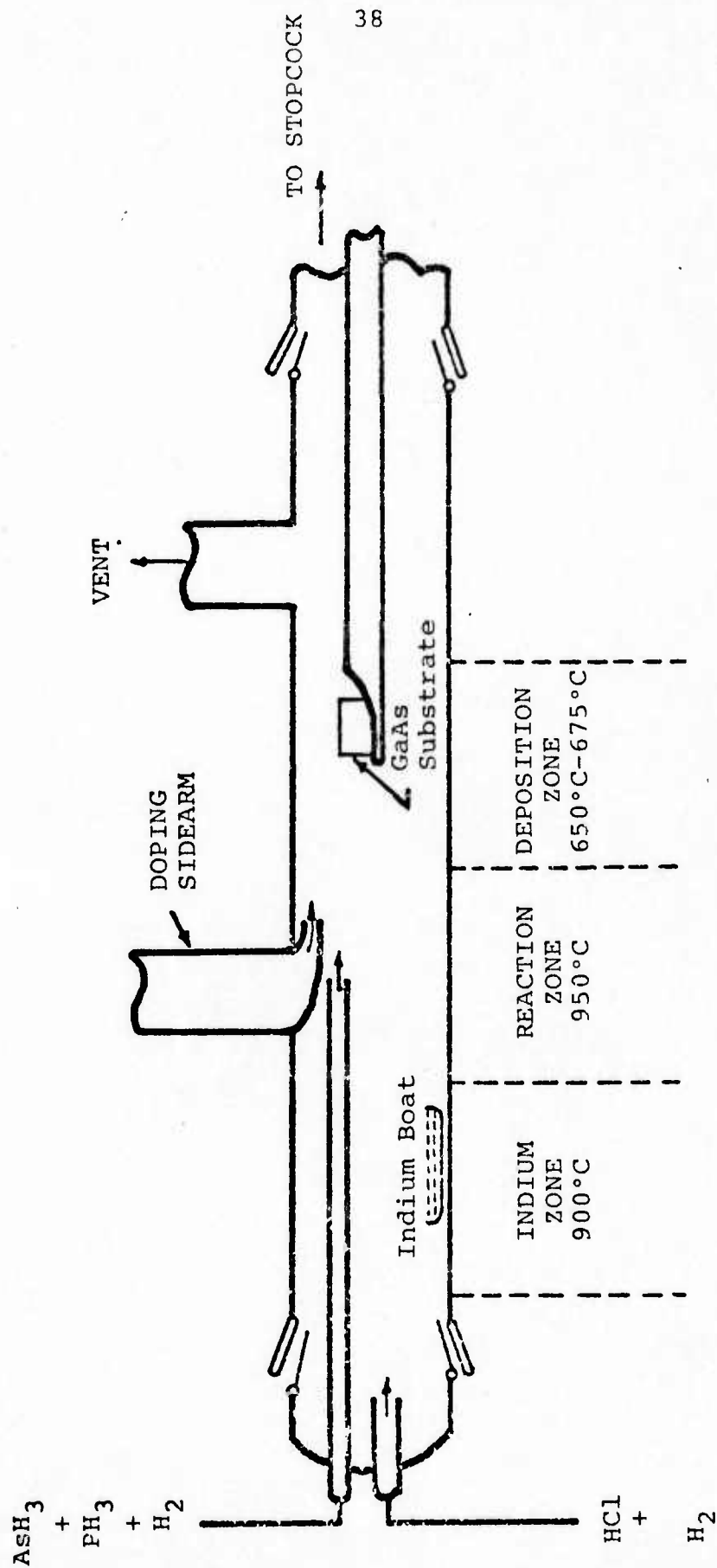grading during a run.

FIGURE 3.1 DIAGRAM OF VAPOR DEPOSITON SYSTEM

The substrates used were Cr doped, semi-insulating GaAs ($\rho > 10^6$ ohm-cm) oriented $5° \pm 0.5°$ off the [001] axis toward the [110] direction. One face was chemically polished to a mirror finish and the other mechanically lapped. In preparation for deposition, each substrate was degreased in trichloroethane and etched for $30 \sim 45$ minutes in Caro's acid (H_2SO_5) using an inclined, rotating Teflon beaker. The substrates were rinsed in baths of deionized water and methanol, then blown dry with filtered helium. After this cleaning procedure they were placed directly into the deposition furnace.

Five sets of samples were grown and investigated. The first set, samples 147-152, were grown at the same hydrogen flow rate but with varying As to P ratio. The other four sets were all of the same composition, $InAs_{0.61}P_{0.39}$, but the hydrogen flow rate was varied within each set and deposition time was varied from set to set resulting in different epitaxial thicknesses. Thus this research investigated changing composition, changing hydrogen flow rate, and changing epitaxial thicknesses. A list of the samples with their compositional and growth parameters is given in Table 3.1.

3.2 Sample Preparation

The epitaxial samples as received from Dr. Kennedy were approximately 1x2 centimeters with epitaxial deposits on both the front and back surfaces. The samples were scribed using a Kulicke and Soffa Model 750 Scriber on the back surface and cleaved to obtain two .5x.5 centimeter samples from

TABLE 3.1 GROWTH PARAMETERS AND EPITAXIAL

THICKNESSES FOR $InAs_{1-x}P_x$

	Sample	Flow Rate (CM^3/MIN)	X	t(μm)
	172	1780	.392	4.27
	173	1530	.392	4.11
	174	1280	.392	4.08
Group I	175	910	.392	3.70
	176	730	.392	2.86
	177	570	.392	2.35
	178	515	.392	2.67
			(avg.	= 3.73)
	164	1780	.392	13.23
	168	1530	.392	10.96
	166	1280	.392	10.91
Group II	169	910	.392	8.62
	167	730	.392	7.24
	170	570	.392	6.50
	171	515	.392	5.33
			(avg.	= 8.97)
	153	1780	.392	23.28
	154	1530	.392	19.26
	155	1280	.392	27.46
Group III	156	910	.392	22.17
	157	730	.392	18.68
	159	515	.392	20.62
			(avg.	= 21.91)
	196	3070	.392	108.75
	197	2430	.392	114.67
Group IV	181	1780	.392	106.08
	186	1530	.392	102.50
			(avg.	= 108.00)
	147	2100	.034	8.87
	148	2100	.100	9.09
	149	2100	.200	11.30
Group V	150	2100	..392	34.28
	151	2100	.624	35.90
	152	2100	.774	46.36
			(avg.	= 24.30)

the center. Excess pieces were used for compositional analysis using an electron microprobe. The epitaxial layer thickness of the sample used was measured using an optical microscope equipped with a micrometer eyepiece. Each side of the sample was measured in several places and the results averaged. These results are given in Table 3.1.

In preparation for mounting conducting leads, each sample was first cleaned in baths of trichloroethylene, acetone, methanol, then finally deionized water. The sample was then soldered with indium onto an Al_2O_3 substrate to provide thermal conduction to the cryostat. Electrical connection was obtained by soldering thin wires, using pure indium, to each corner of the sample. The solder connections were typically 0.2 mm in diameter and each was tested for ohmicity. The other ends of the leads were soldered onto the Al_2O_3 substrate at which point leads from the cryostat were joined. With this arrangement the sample could be inserted and removed from the equipment without disturbing the ohmic contacts on the sample.

3.3 Experimental Apparatus

The experimental arrangement used for most measurements, Fig. 3.2, incorporated a Heli-Tran Model LT-3-110 to attain temperatures continuously variable between 3K to 300K with a normal ±0.1K stability in the lower range. Temperature readings were made using a chromel versus gold with 0.07 atomic percent iron thermocouple read by a Honeywell Model 2783 six-dial potentiometer. Both the thermocouple junction and the

FIGURE 3.2 - Experimental Setup for Measuring Resistivity and Hall Effect

1) Heli-Tran Model LT-3-110 cold tip

2) Varian V-3706 6-inch electromagnet

3) Varian sweep power supply

4) Liquid helium dewar

5) Vacuum pump

6) Bell Model 620 gaussmeter

7) Deionized ice bath

8) Honeywell Model 2783 potentiometer

9) Standard cell

10) Six-volt current source

11) Hewlett-Packard Model 725A DC Micro Volt-Ammeter

12) Control panel

13) Electronic Measurements Model C633 Constant Current
Power Supply
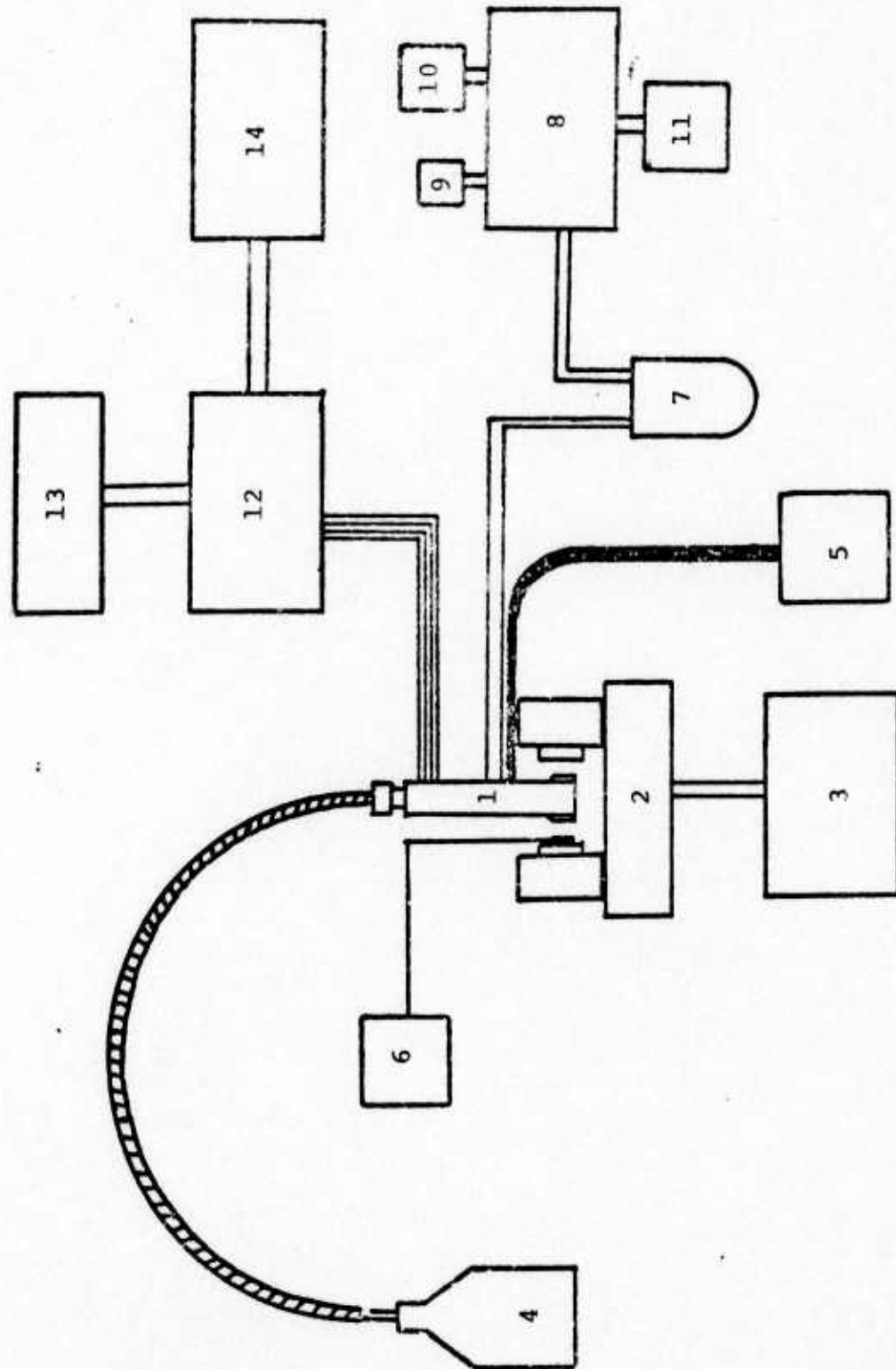
14) Cimron Model 6653A Digital Multimeter

43

FIGURE 3.2

sample were mounted on a copper heat sink in the cryotip - the thermocouple with GE 7031 varnish and the sample with Cry-Con grease.

A uniform magnetic field was provided by a Varian V-3703 electromagnet with six inch pole pieces. Fields up to 6 kilogauss in strength and as low as 10 gauss were used for Hall coefficient and magnetoresistance measurements. The magnetic field was monitored by a Bell 620 gaussmeter.

The thin epitaxial samples were especially suited for measurement using the standard Van der Pauw[39] technique. The four leads from each corner of the sample were connected to a switching control panel which provided the necessary interchange of current and voltage leads and also current reversal. In addition, the magnetic field was reversed during each set of measurements to average out any inhomogeneities in the magnetic field.

An Electronic Measurements C633 constant current supply was used to provide a current of 0.5 milliamperes through the sample. This low current was used to eliminate possible heating effects but yet produce voltages large enough to be read accurately. The voltage across the samples was read by a Cimron 6653A digital multimeter with a resolution of one microvolt.

CHAPTER IV

EXPERIMENTAL RESULTS OF $InAs_{0.61}P_{0.39}$

4.1 Sample Description

Four sets of samples were grown using the methods
described in Chapter III with the arsine to phosphine ratio
adjusted so as to give 0.61 As and 0.39 P. The deposition
time was varied from set to set to obtain different epita-
xial layer thicknesses. For samples of Group I (172-178)
the average thickness was 3.4 μm, for Group II (164-171) the
average was 9.0 μm, for Group III (153-159) the average was
21.9 μm, and for Group IV (196-186) the average was 108.0 μm.

Within each set, the thickness of each sample was some-
what dependent upon the flow rate as shown in Fig. 4.1 for
the first three sets. It might be appropriate at this point
to note that the thicknesses, as given in Table 3.1, are
averages of numerous measurements made on each sample and
that some samples, especially the thicker ones, were not of
uniform thickness. The thicker samples also showed a greater
density of visible surface defects in the form of hillocks.
It is difficult to estimate to what extent these problems af-
fected the reliability of the experimental results.

The alloy composition was verified using an electron
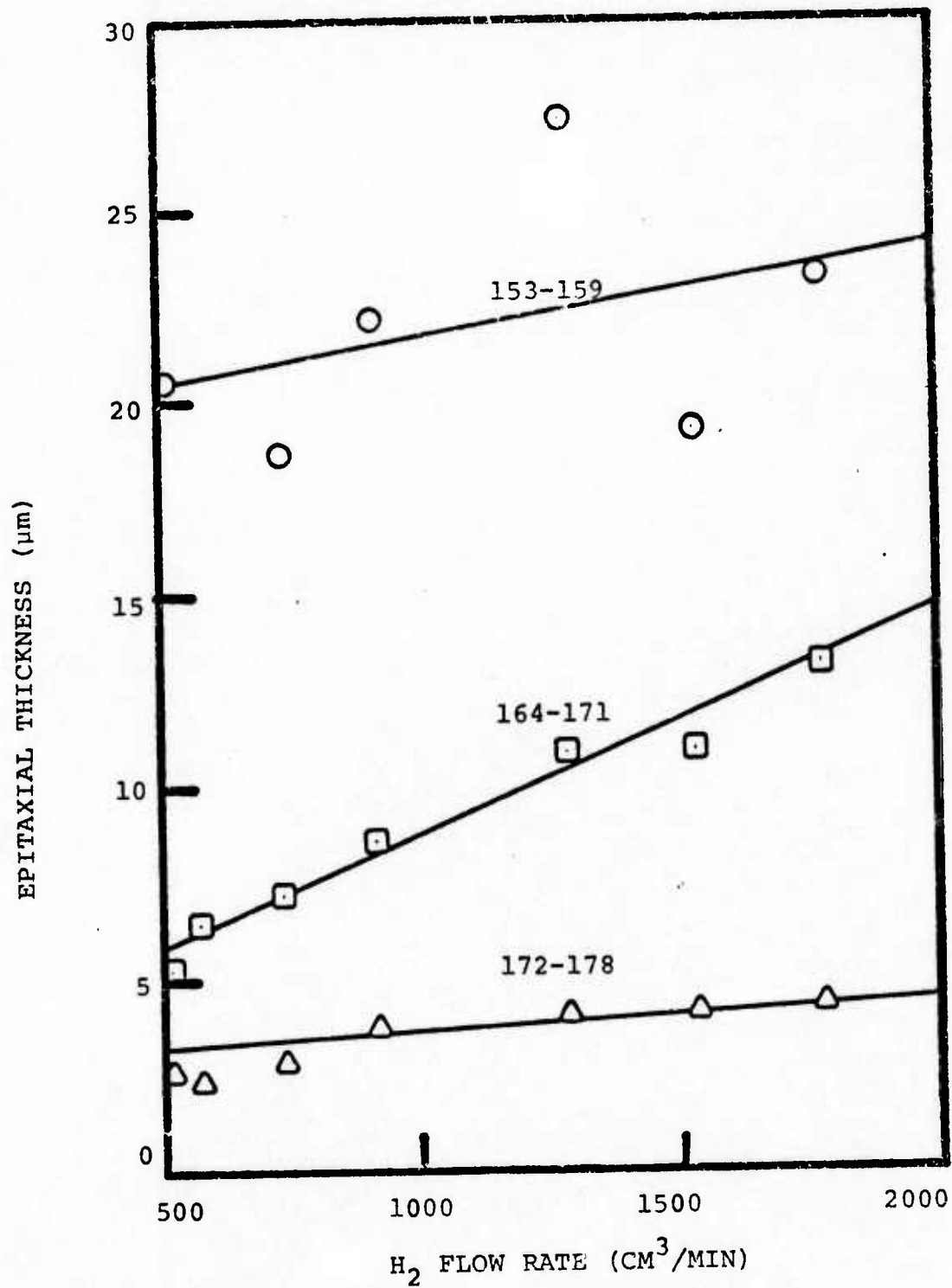microprobe. The results of this analysis showed significant

FIGURE 4.1   EPITAXIAL THICKNESS VARIATION WITH
HYDROGEN FLOW RATE

scatter as illustrated in Fig. 4.2. However, the average of all samples gives a composition of InAs$_{.616}$P$_{.384}$ which is close to the value prescribed for these samples.

4.2 Resistivity Data

Resistivity measurements were made on samples of each group over the temperature range from 4.2K to 300K. Some samples of Groups I and IV were measured only from liquid nitrogen temperatures to room temperature in an effort to conserve liquid helium. The results of these measurements are graphed versus inverse absolute temperature in Figs. 4.3-4.7.

The resistivity curves show, in general, three regions of interest. At the highest temperatures most curves, especially those of the thick samples in Groups III and IV, show an exponential decrease with decreasing temperature until approximately 100K which is expected from the normal band conduction process. After reaching a minimum, the resistivity increases exponentially with decreasing temperature in the second region of interest. At approximately 20K, the resistivity begins to saturate and varies linearly with temperature down to the lowest temperatures measured. This linear variation is shown more clearly for samples of each group in Figs. 4.8-4.11. The resistivity curves for these samples are similar to those found for other semiconductors such as Ge[40,41] and InSb.[42,43]

The resistivity in the two low temperature regions below the resistivity minimum may be approximated by the equation
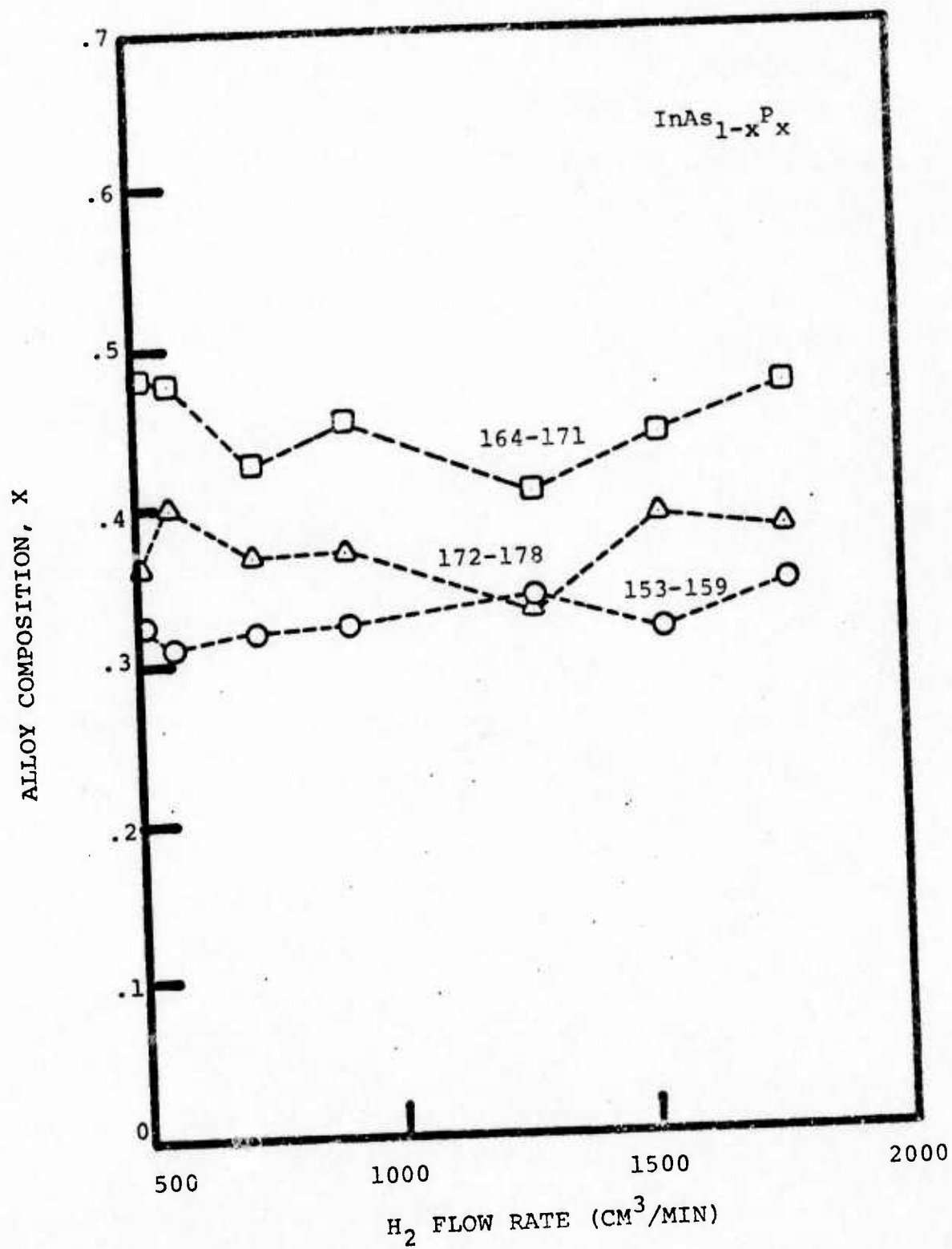
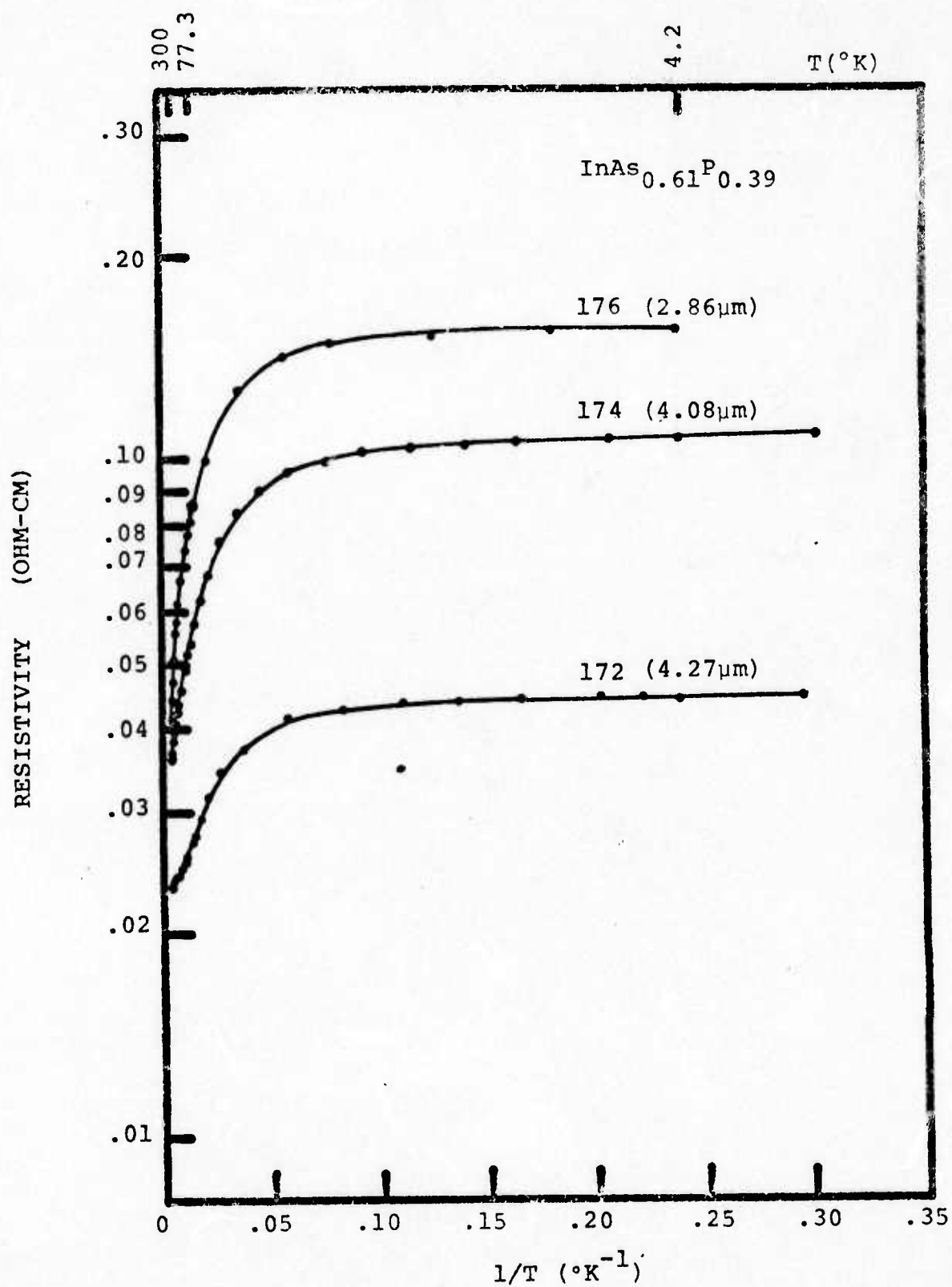FIGURE 4.2   ALLOY COMPOSITION FOR THREE SETS OF
SAMPLES.

FIGURE 4.3   RESISTIVITY OF SAMPLES 172, 174, 176
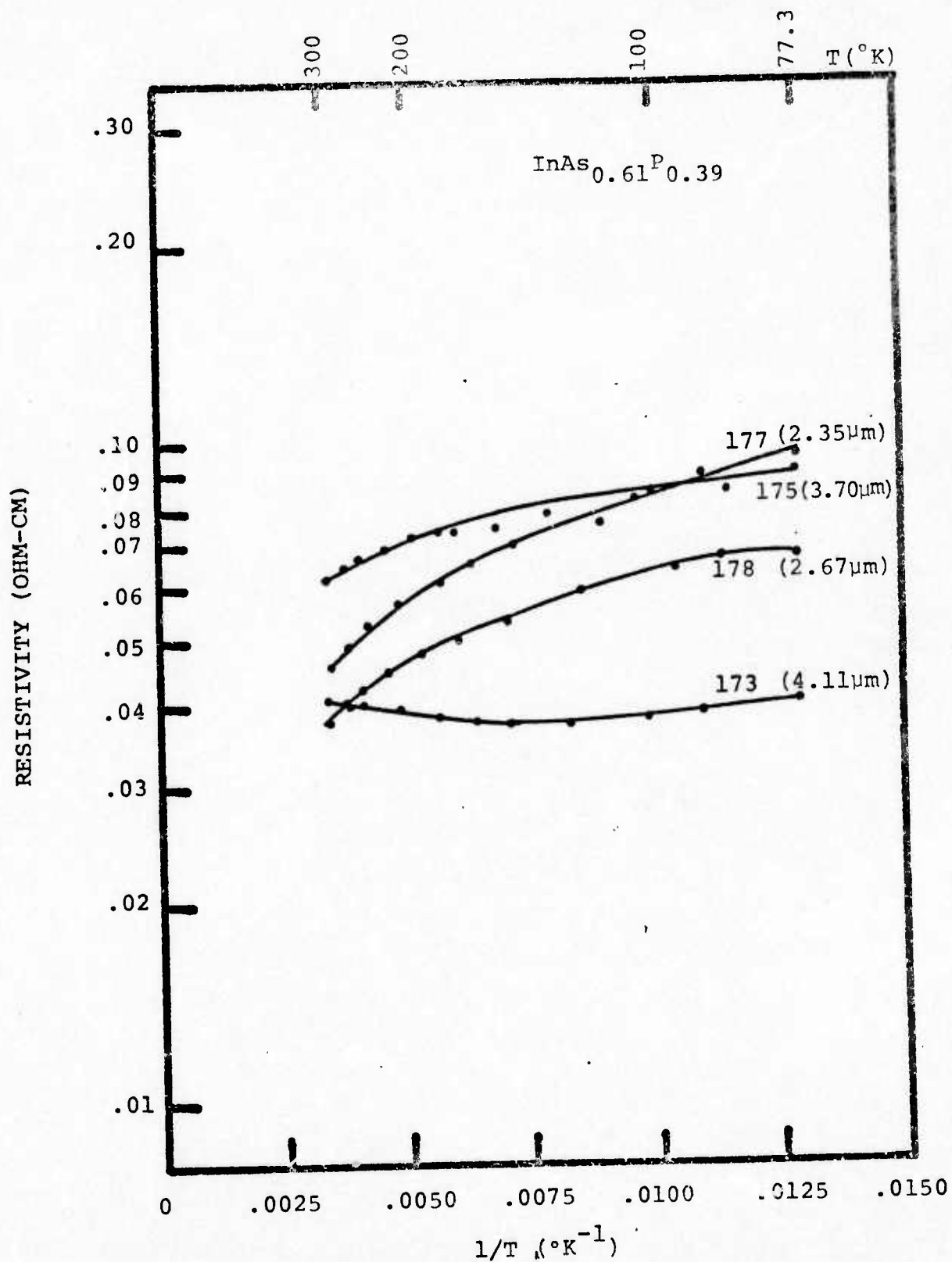VERSUS INVERSE TEMPERATURE

FIGURE 4.4   RESISTIVITY OF SAMPLES 173, 175, 177, 178, VERSUS INVERSE TEMPERATURE
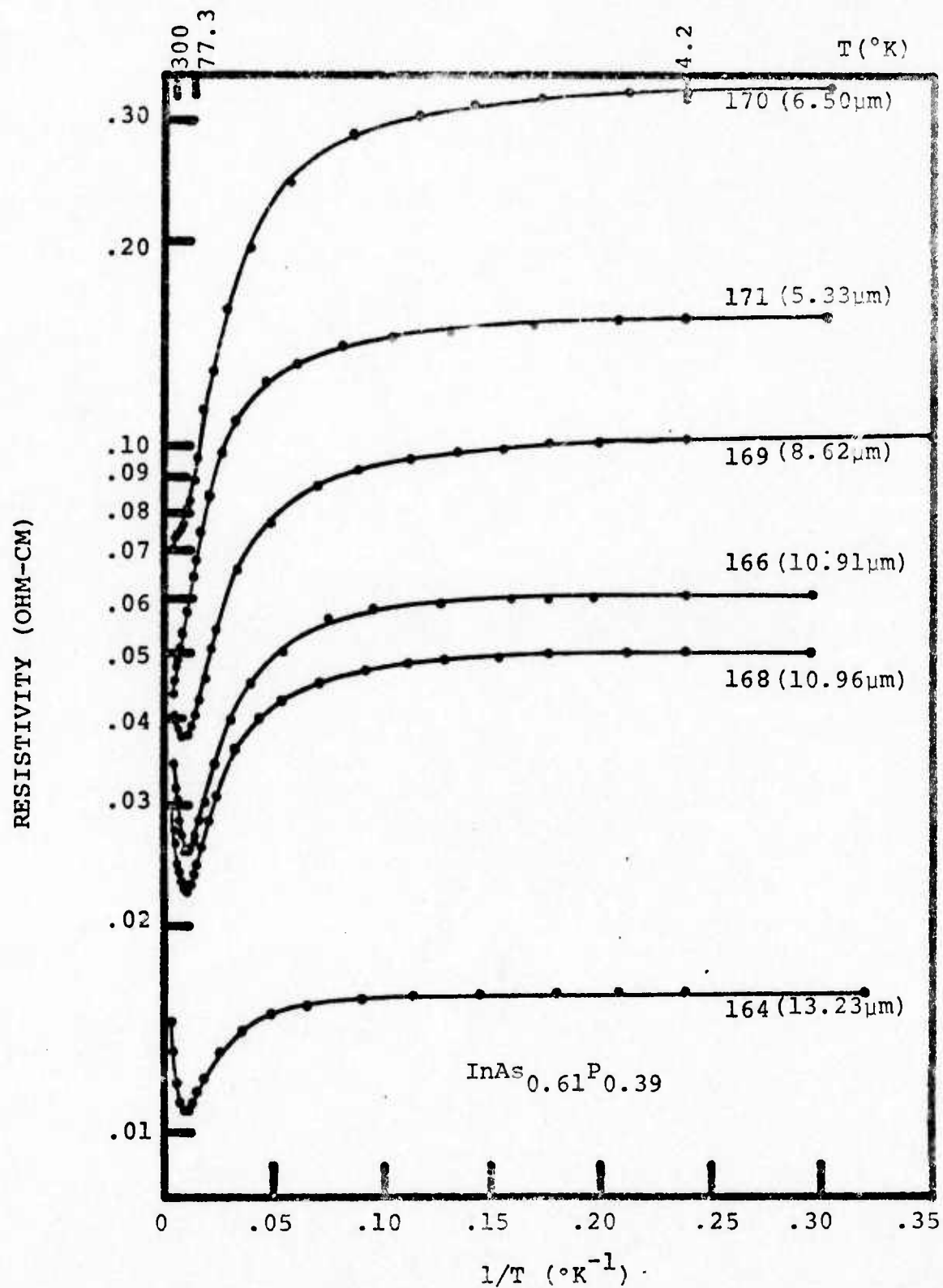
FIGURE 4.5   RESISTIVITY OF SAMPLES 164-171
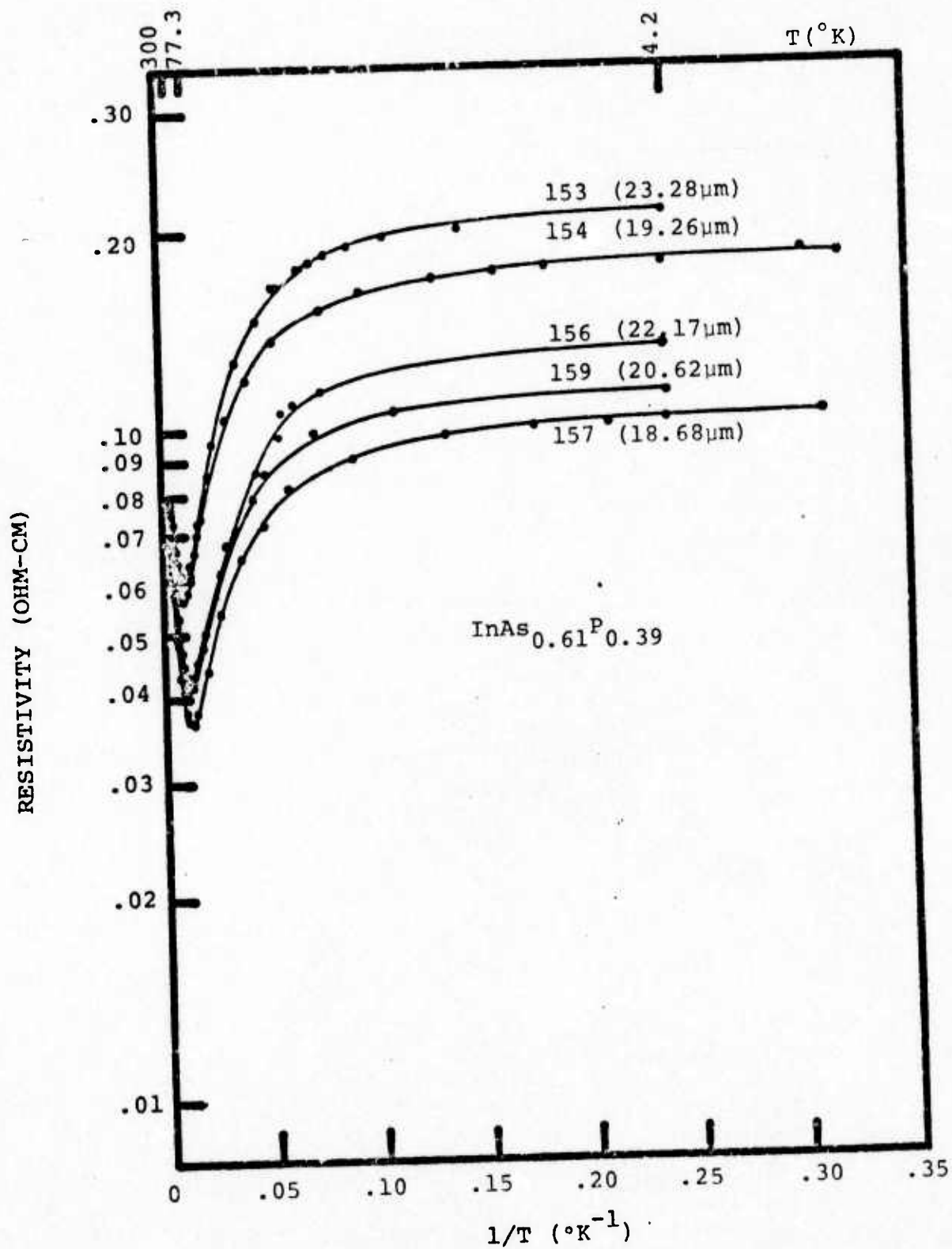VERSUS INVERSE TEMPERATURE

FIGURE 4.6   RESISTIVITY OF SAMPLES 153-159 VERSUS
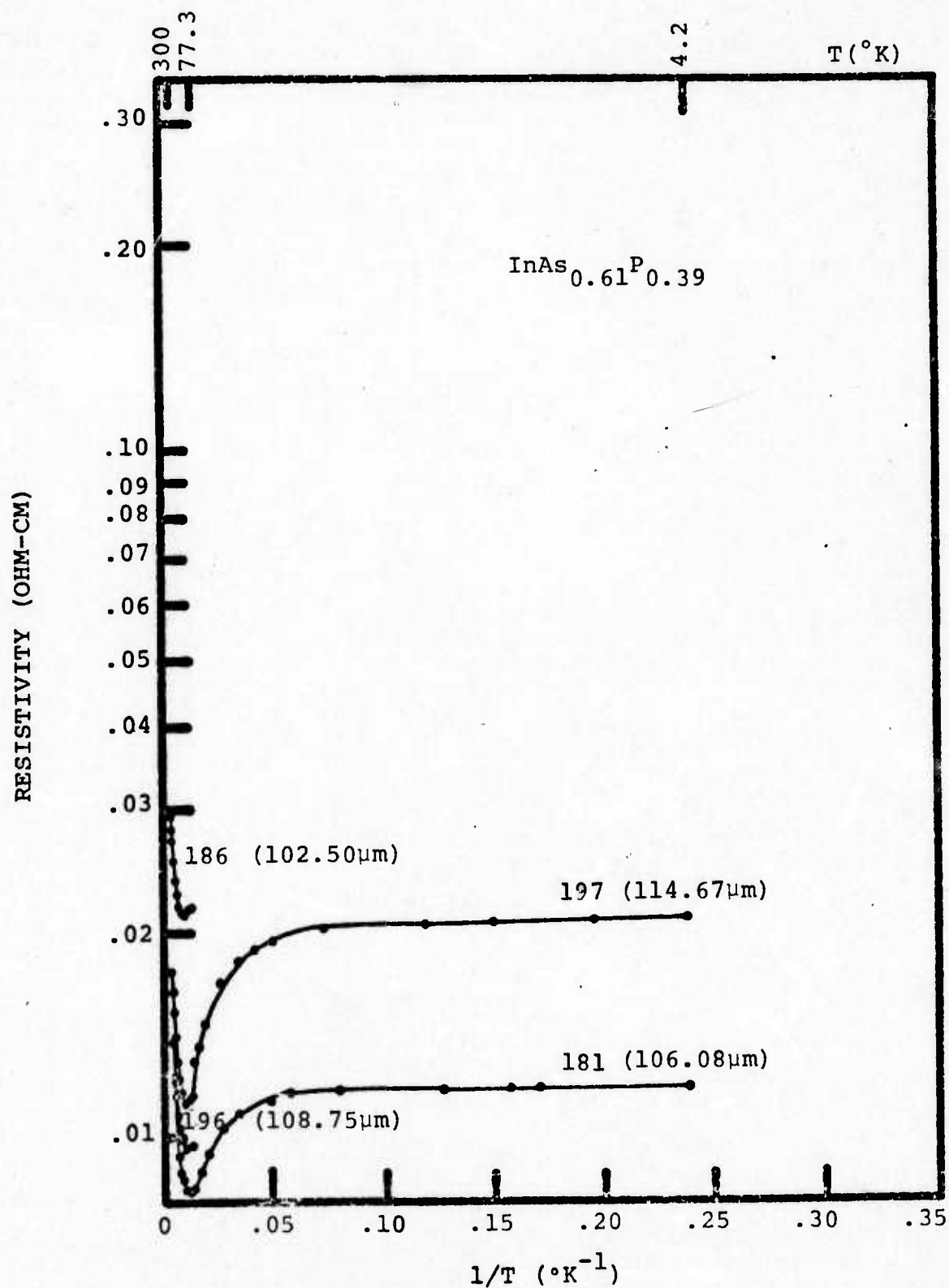INVERSE TEMPERATURE

FIGURE 4.7   RESISTIVITY OF SAMPLES 196-186
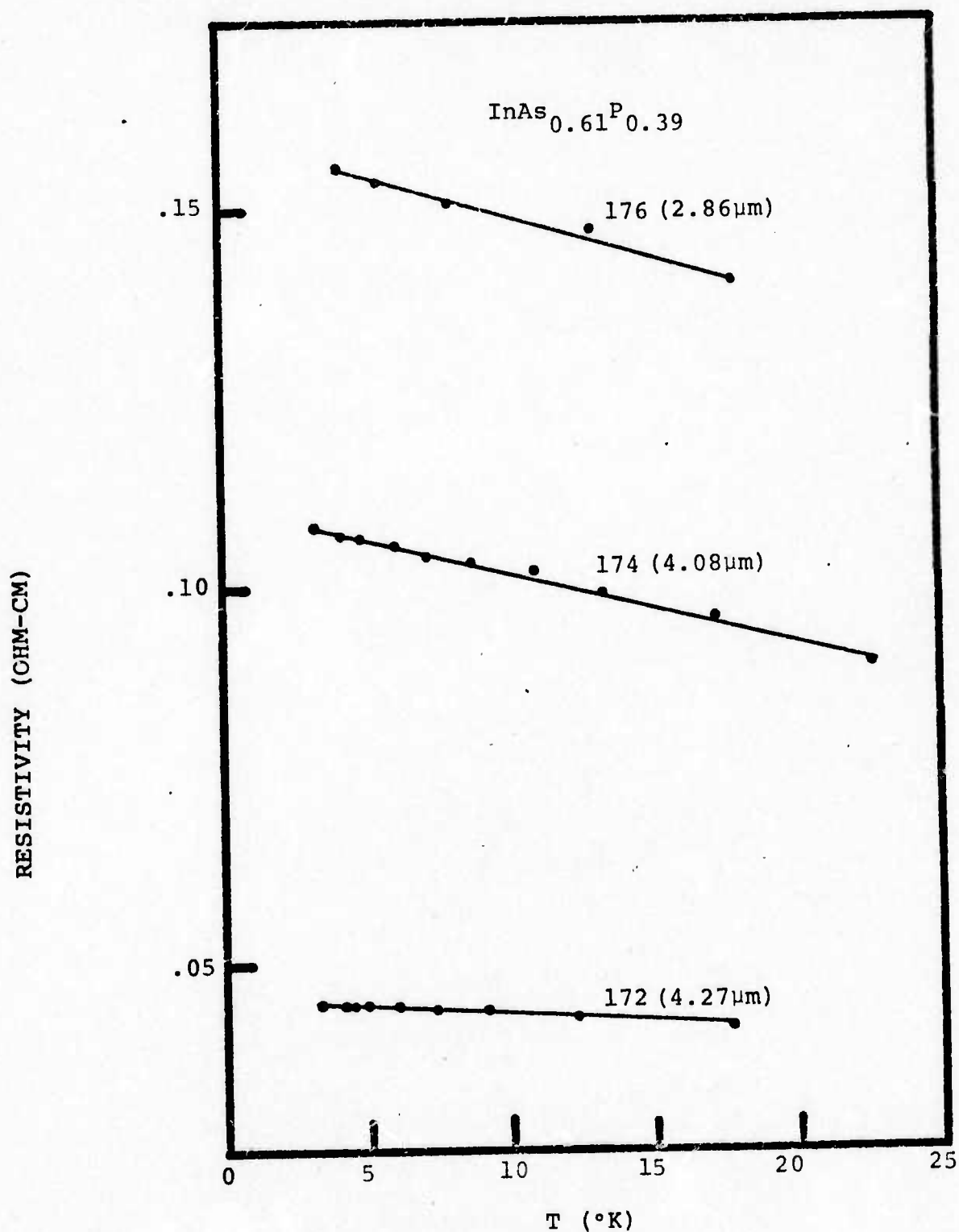VERSUS INVERSE TEMPERATURE

54

FIGURE 4.8 LINEAR VARIATION OF RESISTIVITY FOR
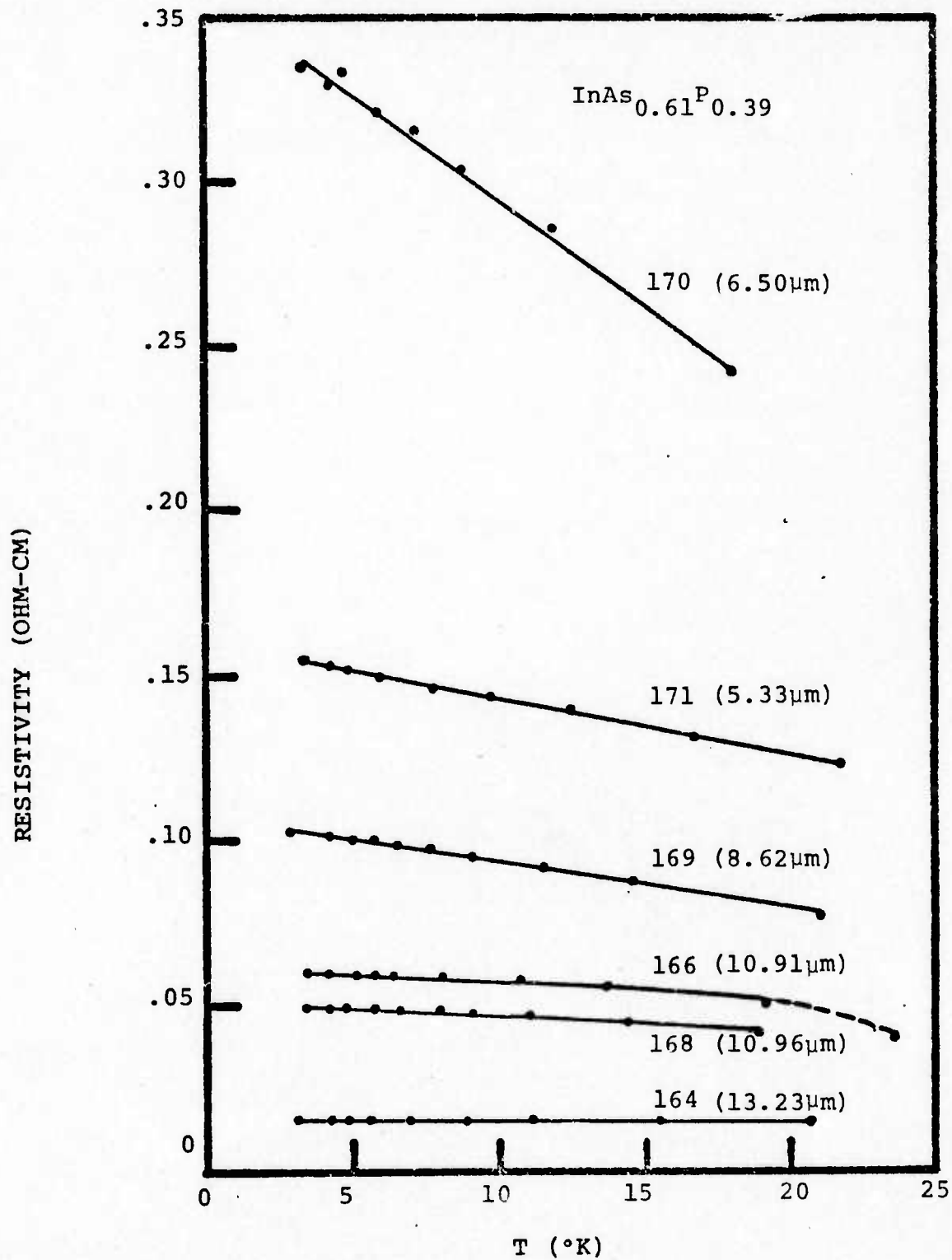SAMPLES 172, 174, 176

FIGURE 4.9   LINEAR VARIATION OF RESISTIVITY FOR
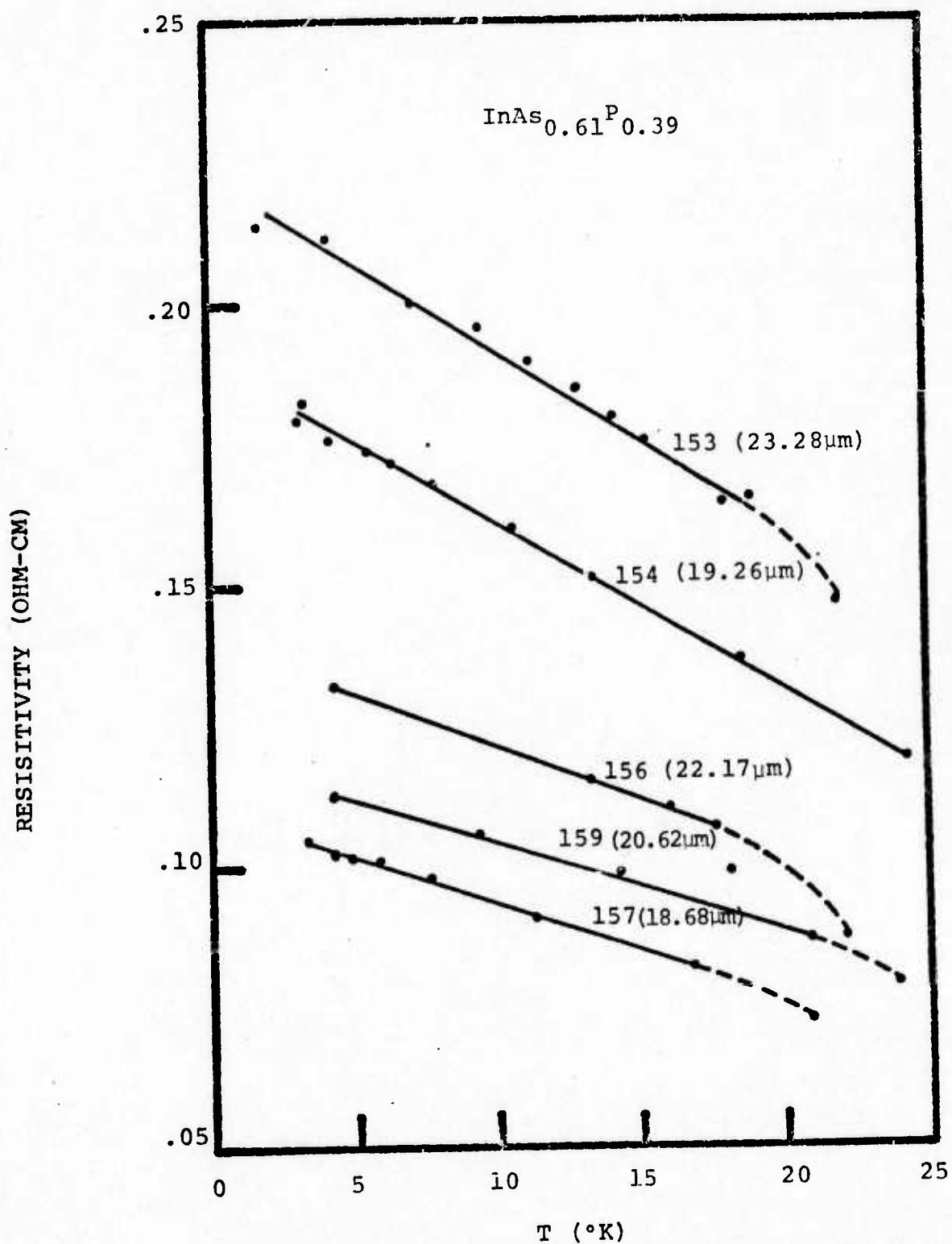   SAMPLES 164-171

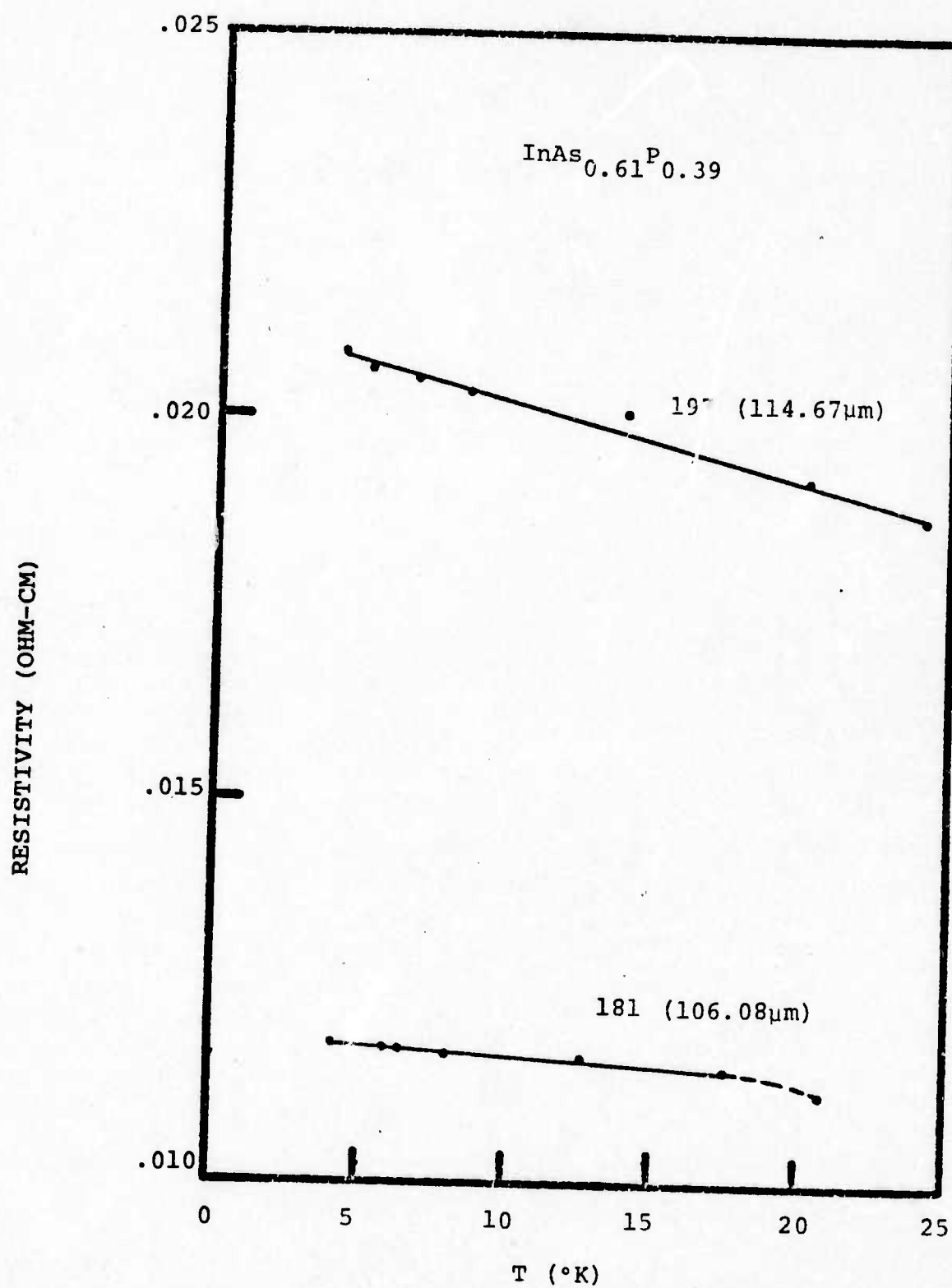FIGURE 4.10   LINEAR VARIATION OF RESISTIVITY FOR
SAMPLES 153-159

FIGURE 4.11   LINEAR VARIATION OF RESISTIVITY FOR
SAMPLES 181, 197

$$\rho^{-1} = C_2 \exp(-E_2/kT) + C_3 T + C_4 \qquad\qquad (4.1)$$

where the first term represents the exponential increase
and the other two terms describe the slow linear increase
at the lowest temperatures. This equation was fitted to the
resistivity data using a least squares approximation to
determine the parameters C_2, C_3, C_4 and the conductivity
activation energy, E_2. The results of these calculations
are listed in Table 4.1. Of special interest are the results
for E_2. These are plotted in Fig. 4.12 against the hydrogen
flow rate. For the thin samples the activation energy shows
a sharp increase with decreasing flow rate. As the epitaxial
thickness increases, the activation energy changes its depend-
ence until, for the thick samples, it shows a decrease with
decreasing flow rate. This is further borne out by the results
for the 100 μm samples (197 and 181) which were not plotted.

One other point of interest is the movement of the resis-
tivity minimum with changes in thickness. For the thinnest
samples (172-178), this minimum occurs at a temperature higher
than 300K which was the upper limit of our equipment. The
9 μm samples (164-171) showed, on an average, a minimum at
about 170K. The other two groups (153-159 and 196-186) both
showed minimums at around 100K. This might be attributed to
the effects of a transition layer between the GaAs substrate
and the $InAs_{1-x}P_x$ epilayer. If the interface layer is of the
order of a micron it would significantly affect the character-
istics of the 3 μm samples, but become less significant as

TABLE 4.1   CONDUCTIVITY PARAMETERS

$$\rho(T)^{-1}= C_2 \; \exp(-E_2/kT) \; + \; C_3 T \; + \; C_4 \qquad (T<100K)$$

| Sample	Flow Rate	C_2	E_2 (meV)	C_3	C_4
172	1780	45.8	1.48	.125	21.93
173	1530	31.7	1.62		
174	1280	30.2	3.16	.084	8.99
175	910	17.9	3.40		
176	730	30.1	7.01	.049	6.22
177	570	37.5	13.70		
178	515	48.1	14.70		
164	1780	109.1	1.26	.380	81.87
168	1530	58.7	2.19	.341	24.97
166	1280	53.7	2.36	.279	20.69
169	910	35.7	2.47	.239	11.95
170	570	18.5	3.47	.122	3.42
171	515	26.9	3.63	.119	8.16
153	1780	25.0	3.13	.147	5.52
154	1530	26.1	3.04	.176	6.70
155	1280	33.1	2.04	.237	12.56
156	910	30.9	1.85	.180	9.31
157	730	39.4	2.46	.305	11.59
159	515	29.7	1.72	.213	10.76
197	2430	107.0	2.01	.236	47.15
181	1780	155.0	1.73	.151	84.11
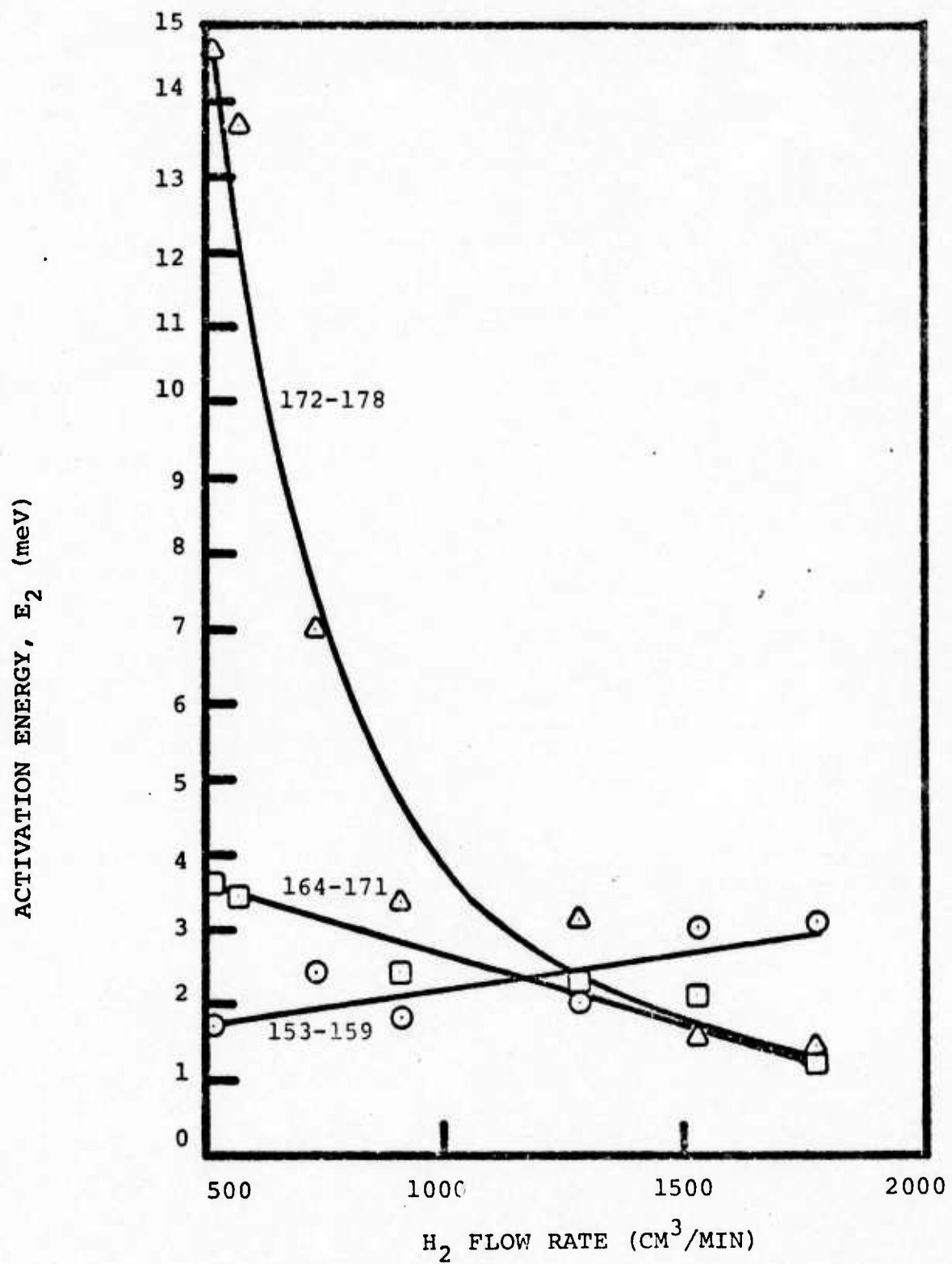
FIGURE 4.12   VARIATION OF ACTIVATION ENERGY, E_2, WITH FLOW RATE

the thickness of the epilayer increases.

4.3 Hall Coefficient and Carrier Concentration

The Hall coefficient, R_h, was measured for each of these four groups of samples as both a function of temperature and as a function of magnetic field strength. The temperature variations are plotted versus inverse absolute temperature in Figs. 4.13-4.17 from 4.2K to 300K. The magnetic field strength used was 5 kilogauss which is not quite the high field limit but should introduce little error since the field dependence was slight except at temperatures around 60K.

The temperature dependence of the Hall coefficient shows a sharp increase with decreasing temperature from 300K to about 60K which may be attributed to normal band conduction. However, at $T \sim 60K$ a maximum is reached and the Hall coefficient begins to decrease until approximately T=20K at which point the Hall coefficient becomes relatively constant. For each sample the low temperature value is very close to the value of the Hall coefficient at 300K.

This type of behavior may be explained by the concept of a donor band presented in Section 2.2c. From Eqn. 2.33 the limits for high temperature may be seen by assuming all available donor electrons are ionized into the conduction band. Thus $n_c = N_d - N_a$ and $n_d = 0$. The Hall coefficient is then at high temperatures

$$R_h = \frac{r_1}{en_c} \qquad \text{(high temp)} \qquad (4.2)$$
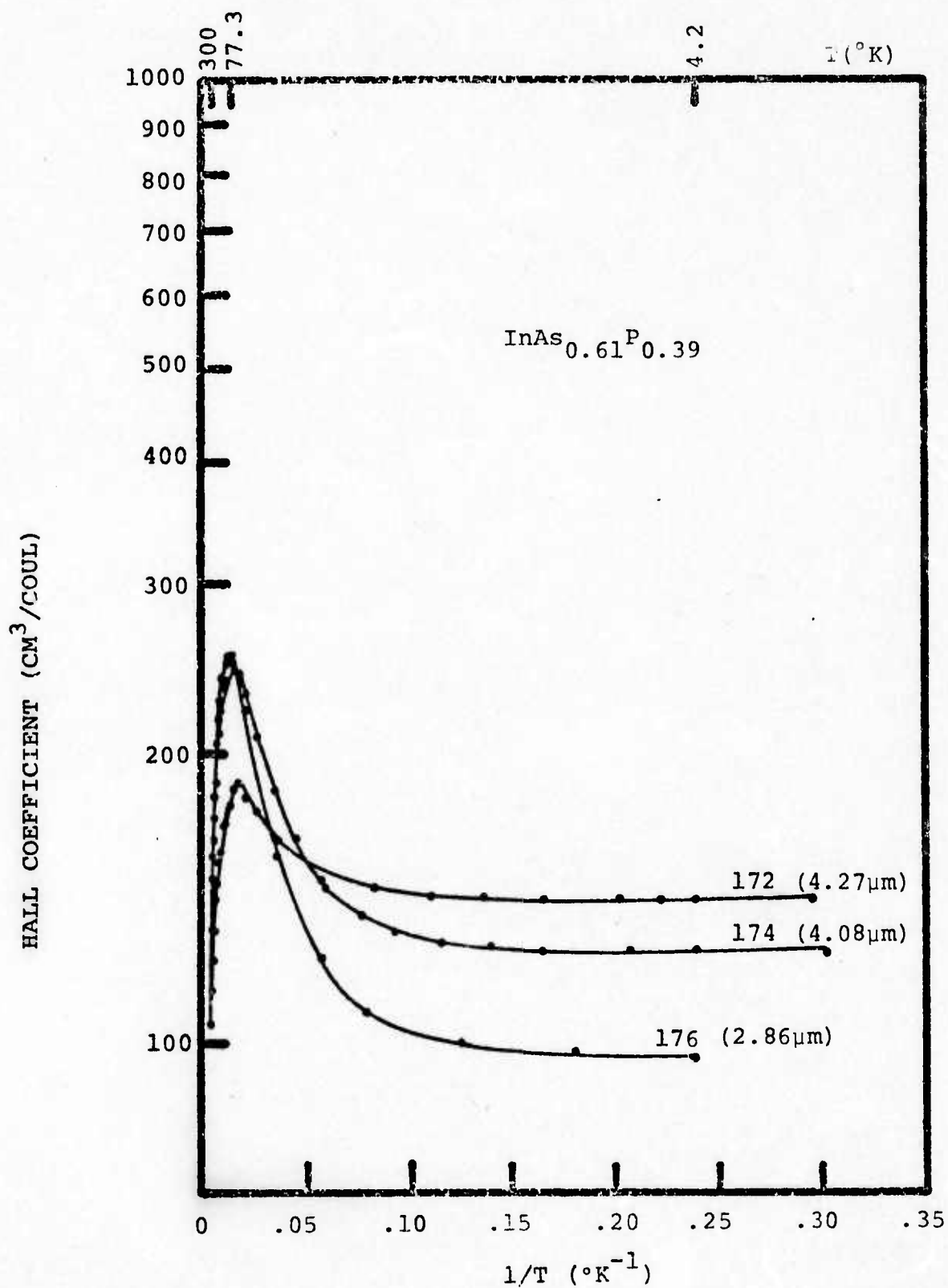
where r_1 is the scattering factor.

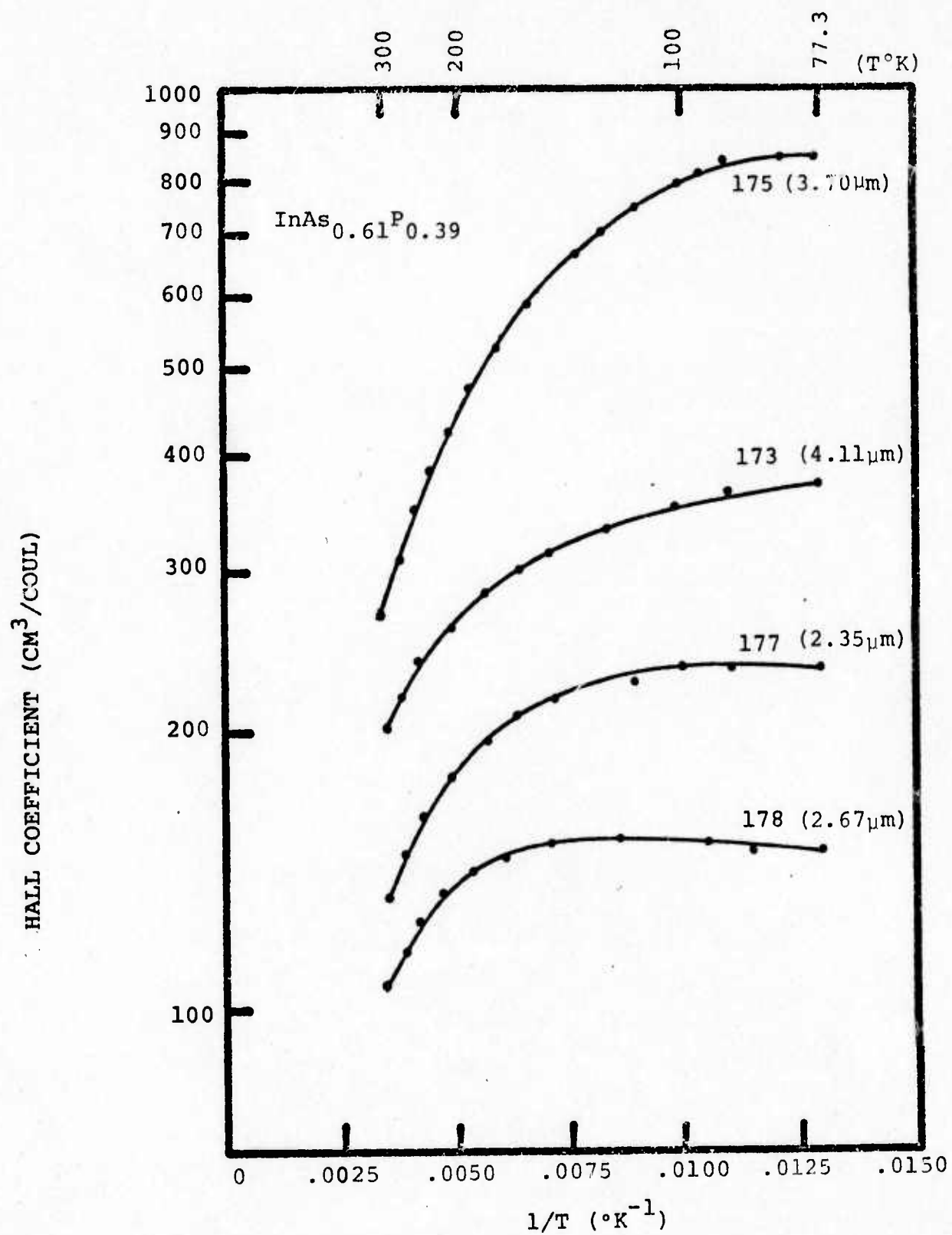FIGURE 4.13 HALL COEFFICIENT OF SAMPLES 172, 174, 176

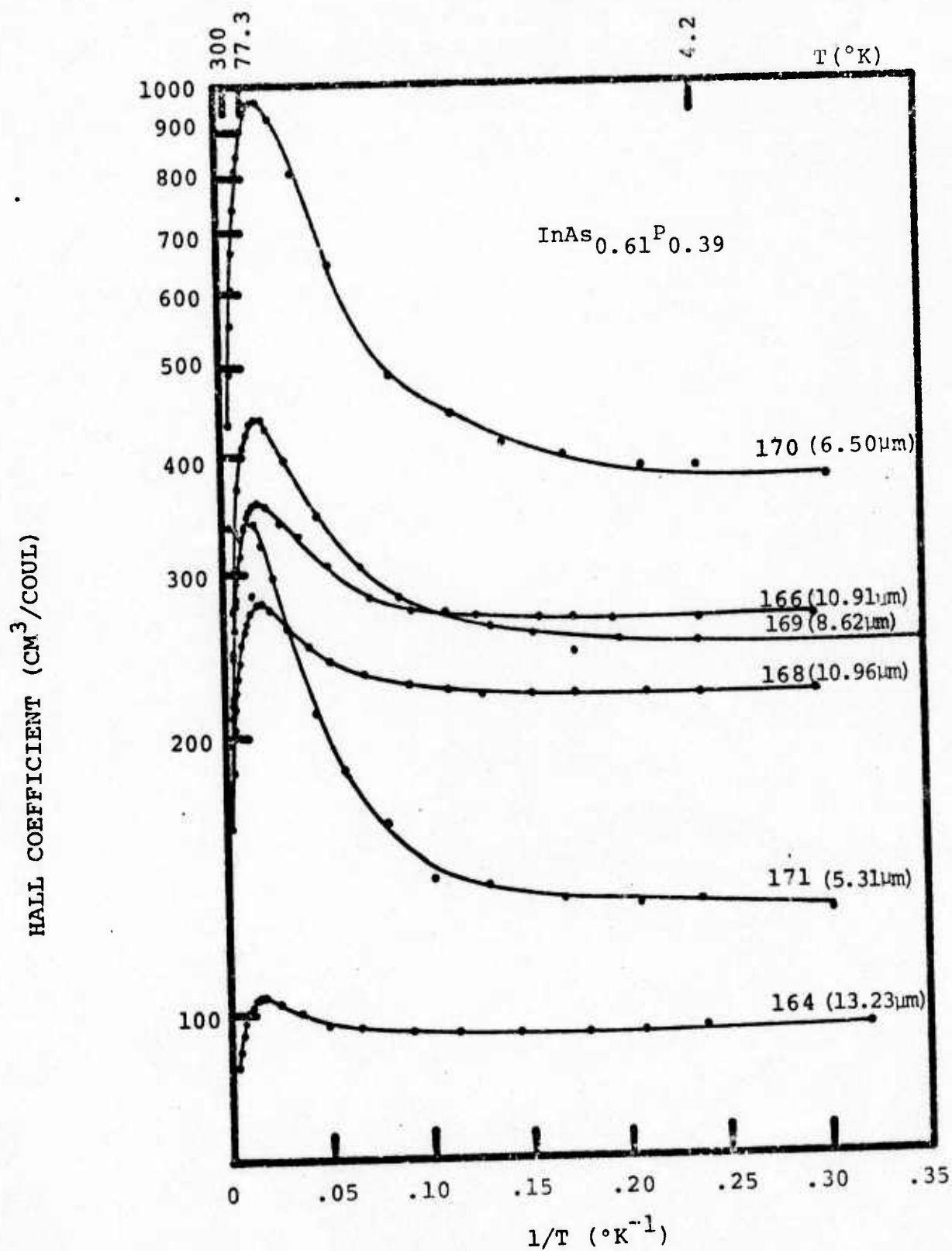FIGURE 4.14   HALL COEFFICIENT OF SAMPLES 173, 175, 177, 178
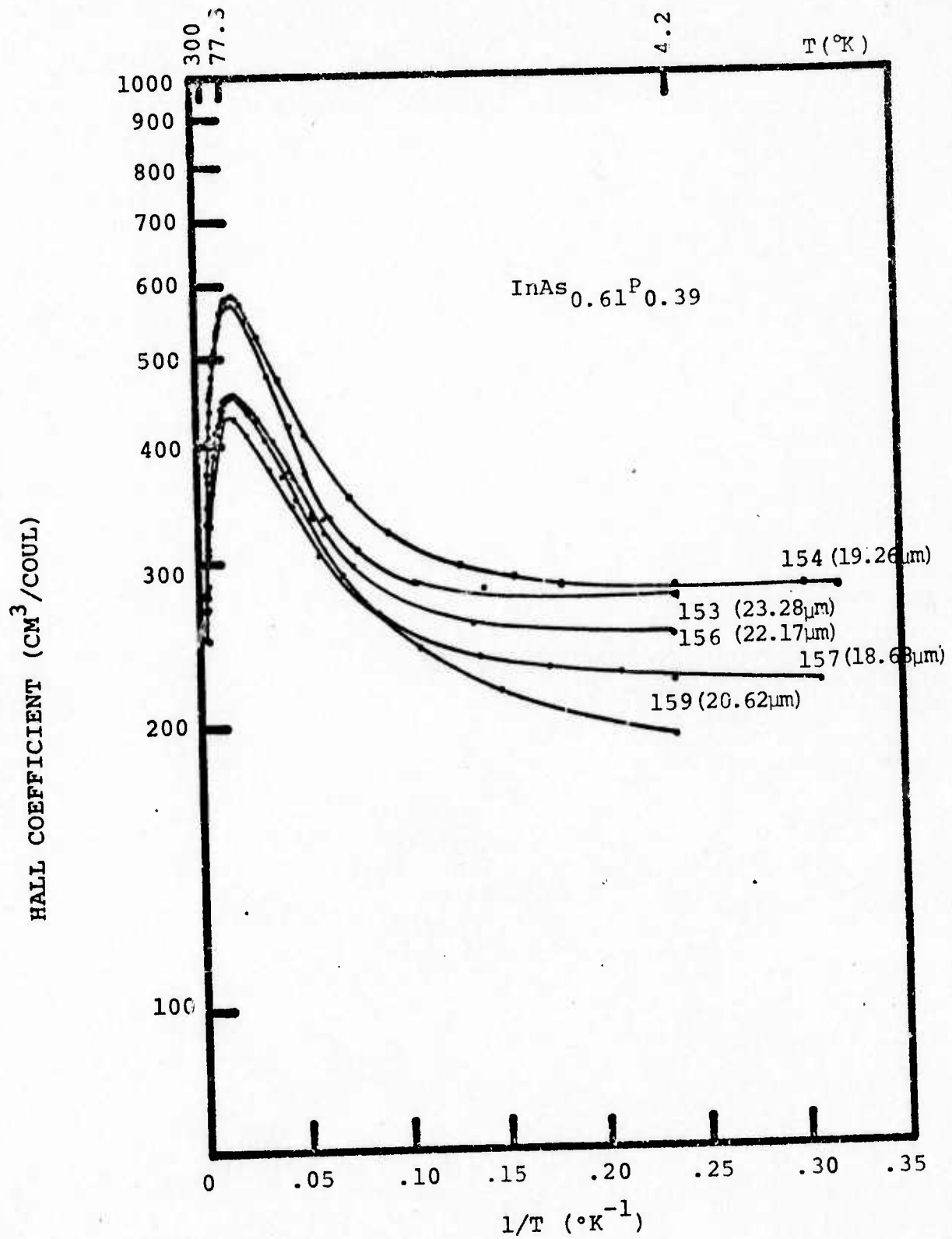
FIGURE 4.15   HALL COEFFICIENT OF SAMPLES 164-171.
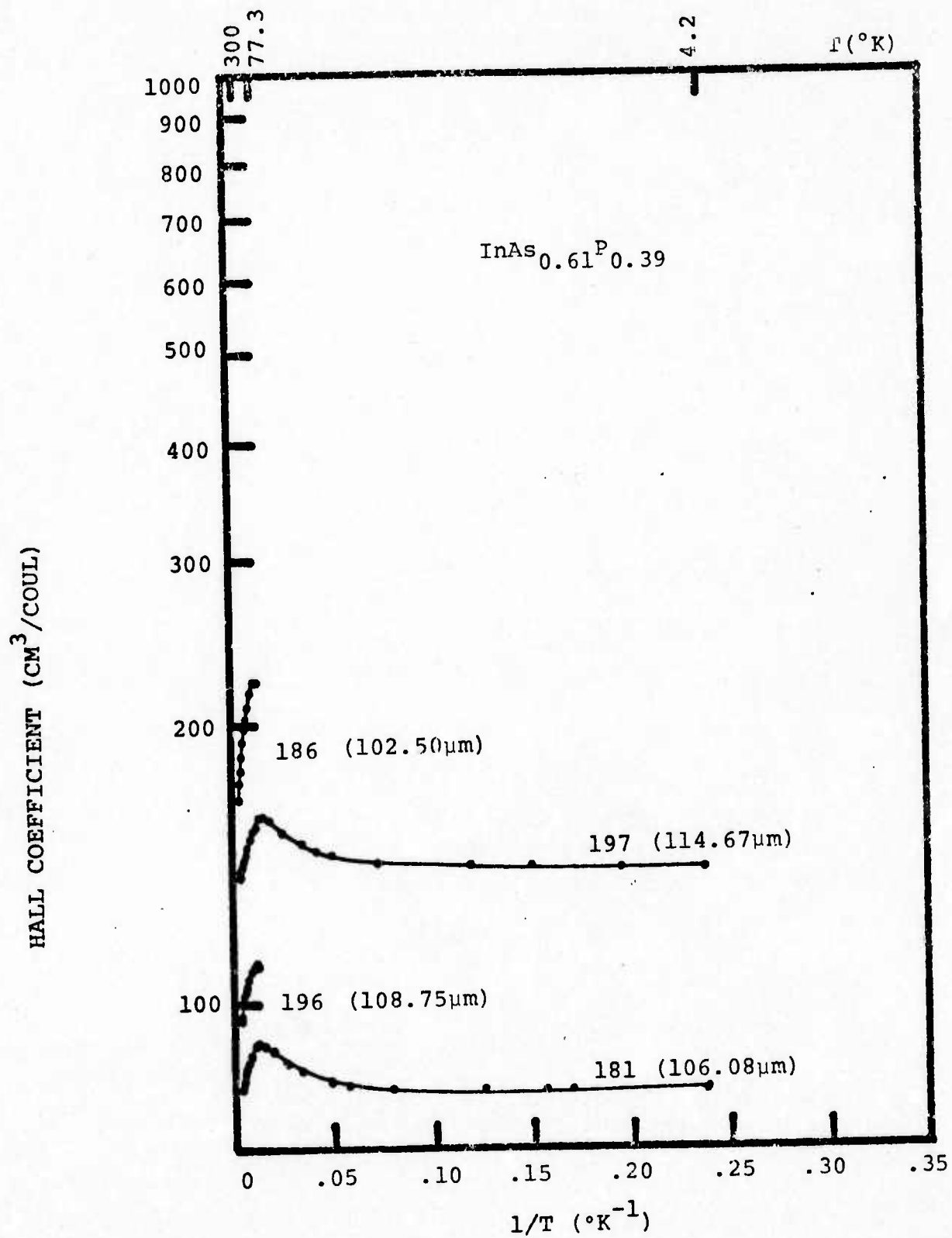
FIGURE 4.16   HALL COEFFICIENT OF SAMPLES 153-159

FIGURE 4.17 HALL COEFFICIENT OF SAMPLES 196-186

At low temperatures all the excited electrons have dropped back into the donor band so that $n_c = 0$ and $n_d = N_d - N_a$.

$$R_h = \frac{r_2}{en_d} \qquad \text{(low temp)} \qquad (4.3)$$

Eqns. 4.2 and 4.3 are identical except for the scattering factor which might be assumed to be unity in each case without causing much error. The Hall coefficients at both high and low temperatures should then be equal and given by

$$R_h = \frac{1}{e(N_d - N_a)} \qquad (4.4)$$

The free electron concentration was calculated from the single band equation:

$$n_h = \frac{r}{eR_h} \qquad (4.5)$$

Here again, the scattering factor, r was assumed to be unity. From experimental data for these samples the Hall coefficient showed little dependence on the magnetic field strength. The greatest error introduced by assuming r=1 should be less than about 10 percent and only present in the intermediate temperature range. The results from Eqn. 4.5 are shown in Figs. 4.18 to 4.22 for $InAs_{0.61}P_{0.39}$. These curves show that all the samples had rather high impurity content especially since there was no intentional doping involved in the growth process. Only two samples (170 and 175) fell into the $10^{15} cm^{-3}$ concen-
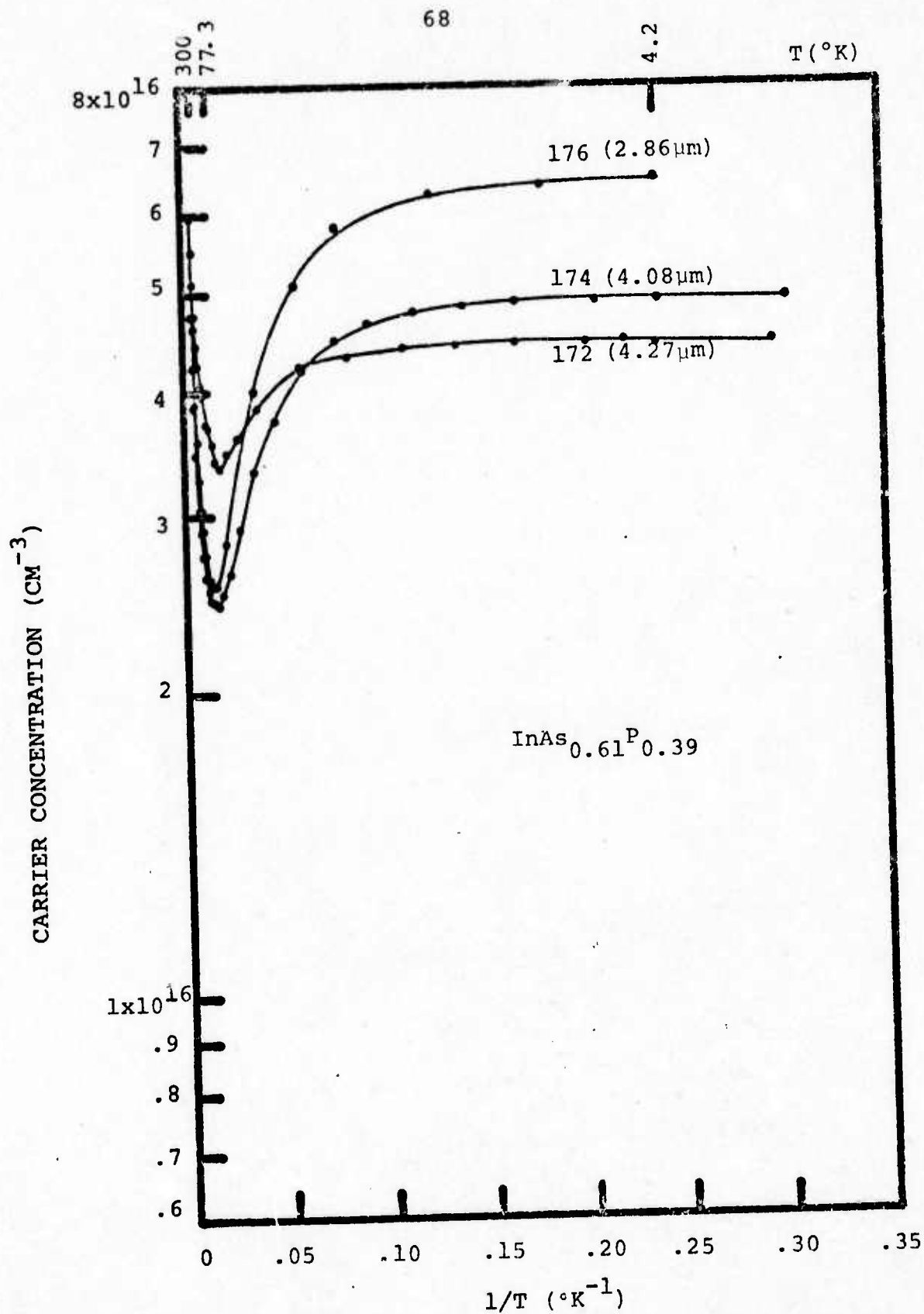
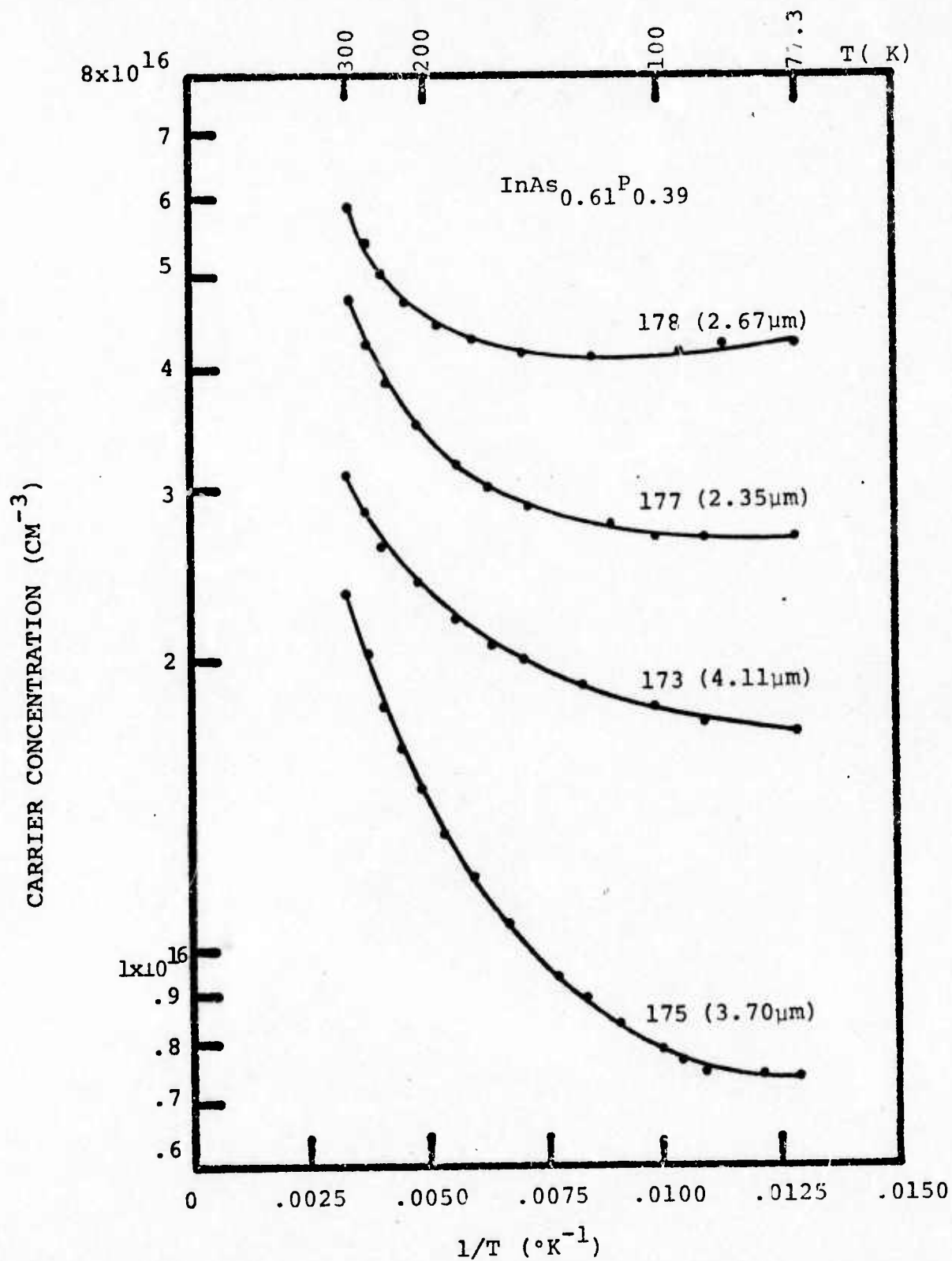FIGURE 4.18   CARRIER CONCENTRATION OF SAMPLES 172, 174, 176

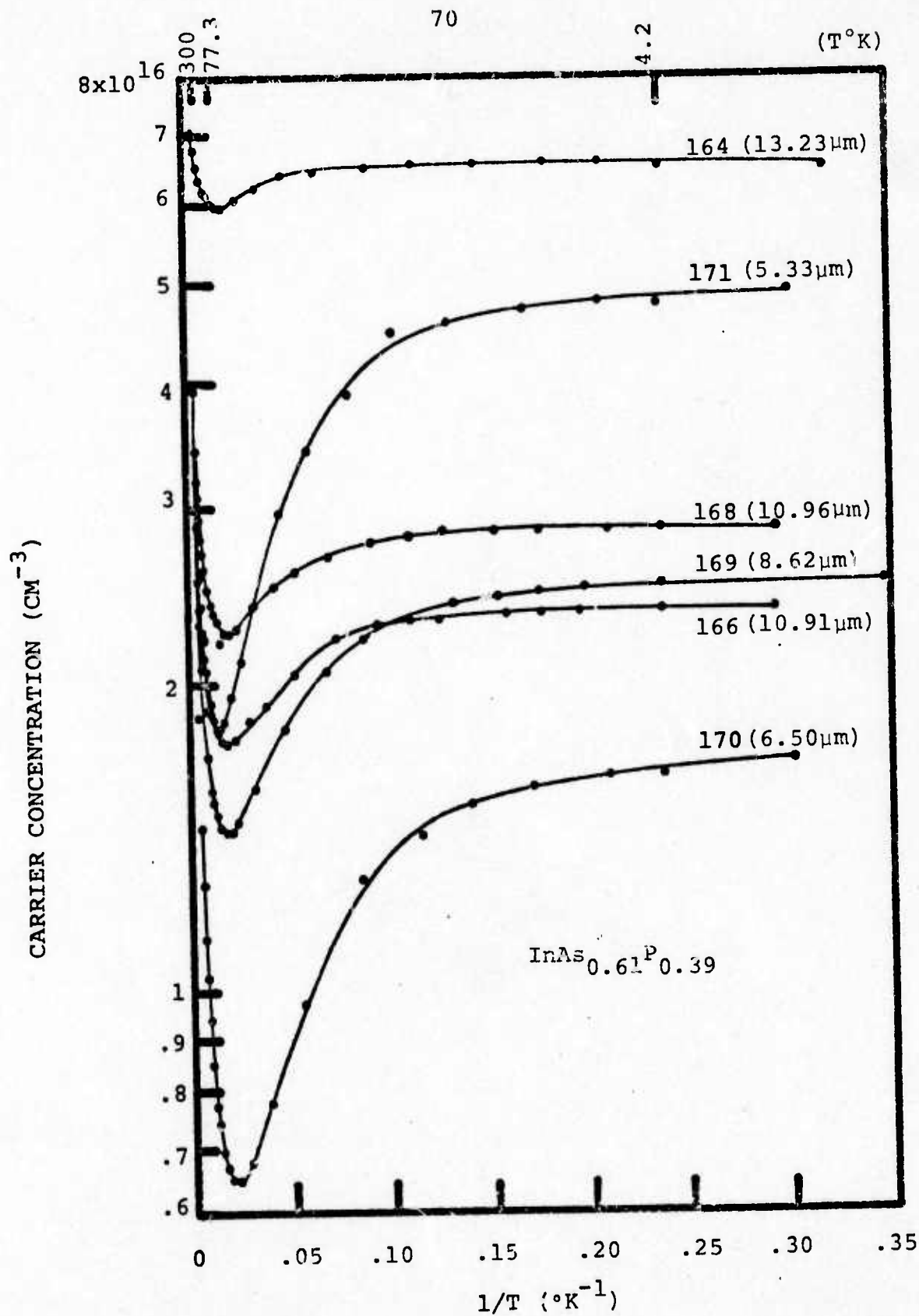FIGURE 4.19   CARRIER CONCENTRATION OF SAMPLES 173,
175, 177, 178

FIGURE 4.20   CARRIER CONCENTRATION OF SAMPLES
164-171
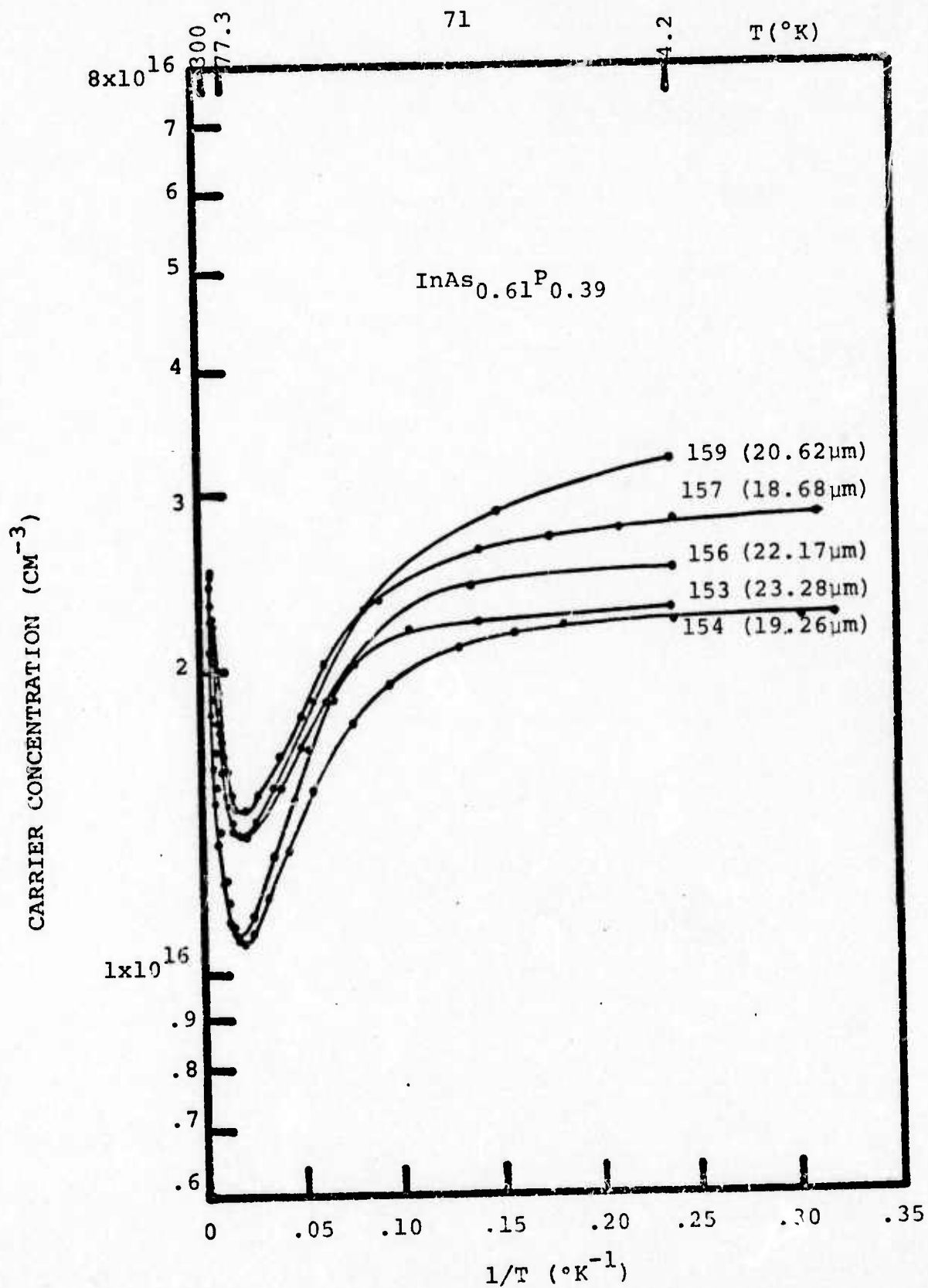
FIGURE 4.21   CARRIER CONCENTRATION OF SAMPLES
153-159
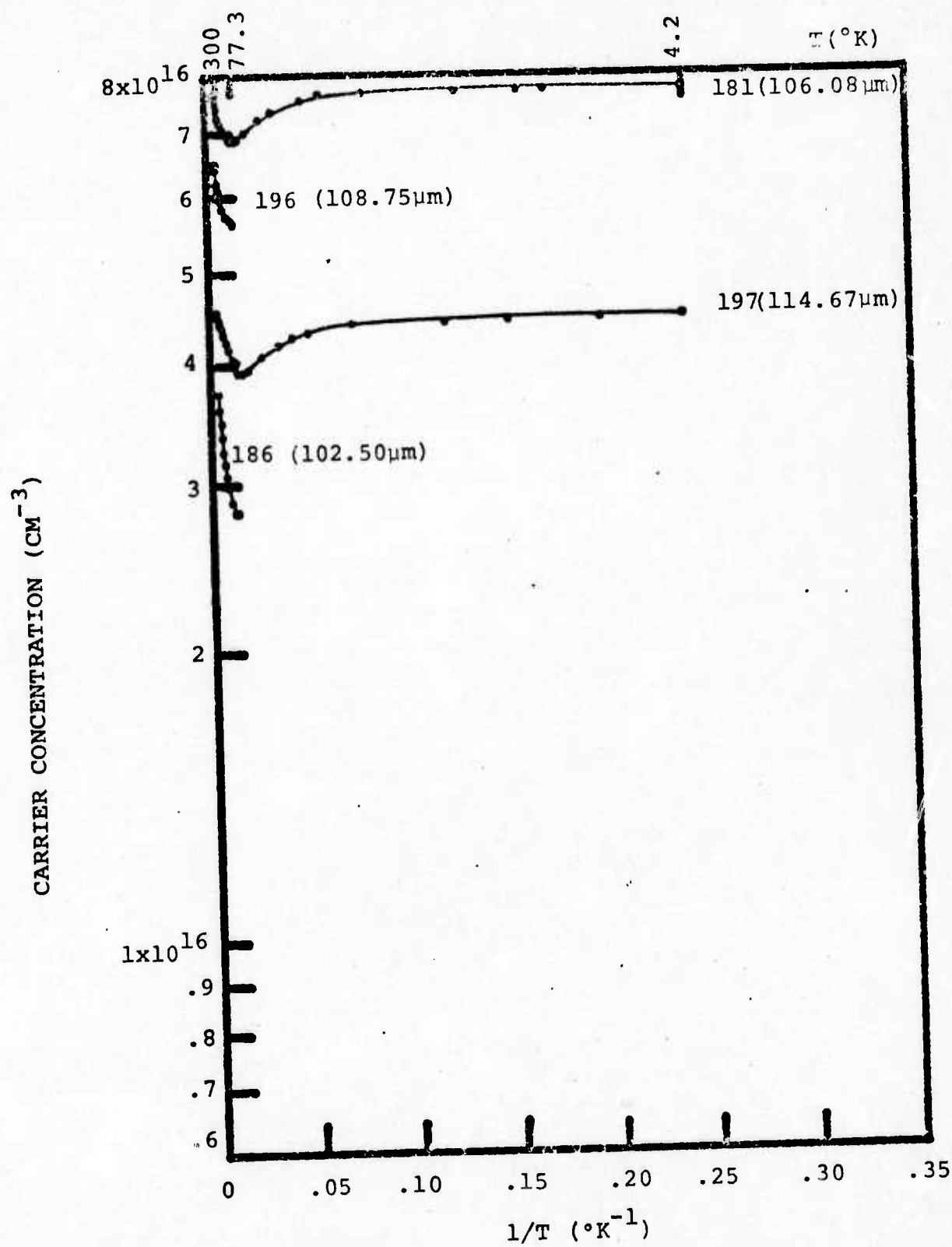
FIGURE 4.22 CARRIER CONCENTRATION OF SAMPLES 196-186

tration range and then only at their minimum points.

The curves in Figs. 4.18-4.22 are, of course, showing the effects of electrons in both the conduction and impurity bands. The actual electron concentrations must be derived from a more rigorous equation such as Eqn. 2.33. This was done for each of the samples by using Eqn. 2.37 to first determine b, the ratio of the mobility in the conduction band to the mobility in the donor band. The result for b was then used in Eqn. 2.38 to determine x, the ratio of free donor electrons to free conduction electrons. This analysis provided the variation of conduction electrons and donor electrons with temperature and the results are illustrated in Figs. 4.23 to 4.26 for a sample from each group (172, 164, 153 and 181) along with n_h from Eqn. 4.5.

The results from this method show both the exponential decrease of the conduction band electrons with temperature and the constant concentration of electrons (N_d-N_a) in the donor band at low temperatures. A different analysis of similar curves from GaAs samples was made by Berg.[44] The approach involved curve fitting to provide the best scattering factor, r. The results were extremely similar to those obtained here for $InAs_{0.61}P_{0.39}$ by this approximate method.

The importance of separating the concentration of electrons from each band is that the temperature variation of the conduction band electrons may now be seen. The exponential decrease is clearly evident in Figs. 4.23 to 4.26 and was

FIGURE 4.23   ELECTRON CONCENTRATION IN THE CONDUCTION AND DONOR BANDS FOR SAMPLE 172
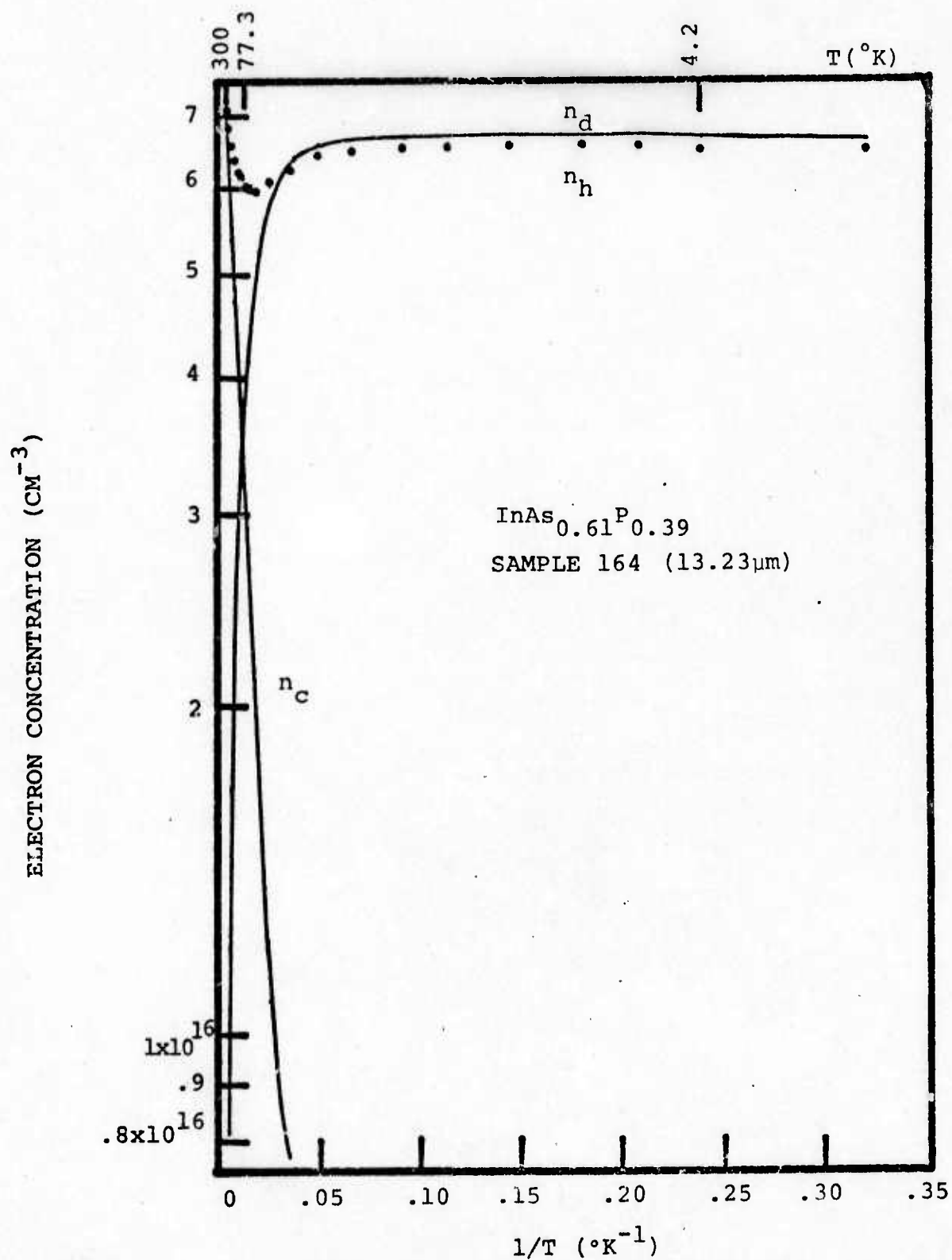
FIGURE 4.24   ELECTRON CONCENTRATION IN THE CONDUCTION
AND DONOR BANDS FOR SAMPLE 164

ELECTRON CONCENTRATION (CM^{-3})

300
77.3
4.2
$T (°K)$

n_d

n_h

2.0

$1x10^{16}$

.9

.8

.7

.6

n_c

.5

.4

$.3x10^{16}$

$InAs_{0.61}P_{0.39}$
SAMPLE 153 (23.28μm)

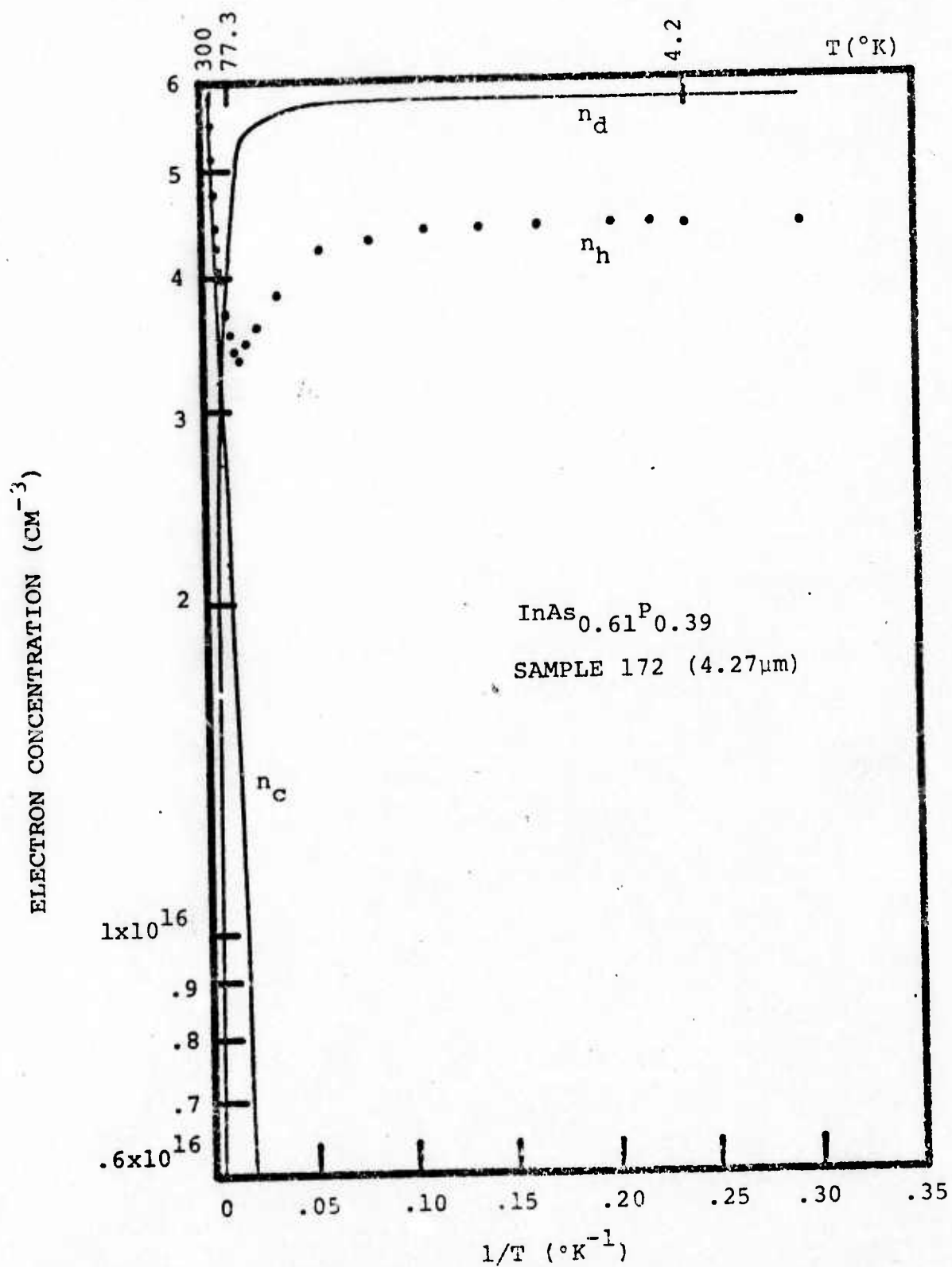0   .05   .10   .15   .20   .25   .30   .35

$1/T (°K^{-1})$
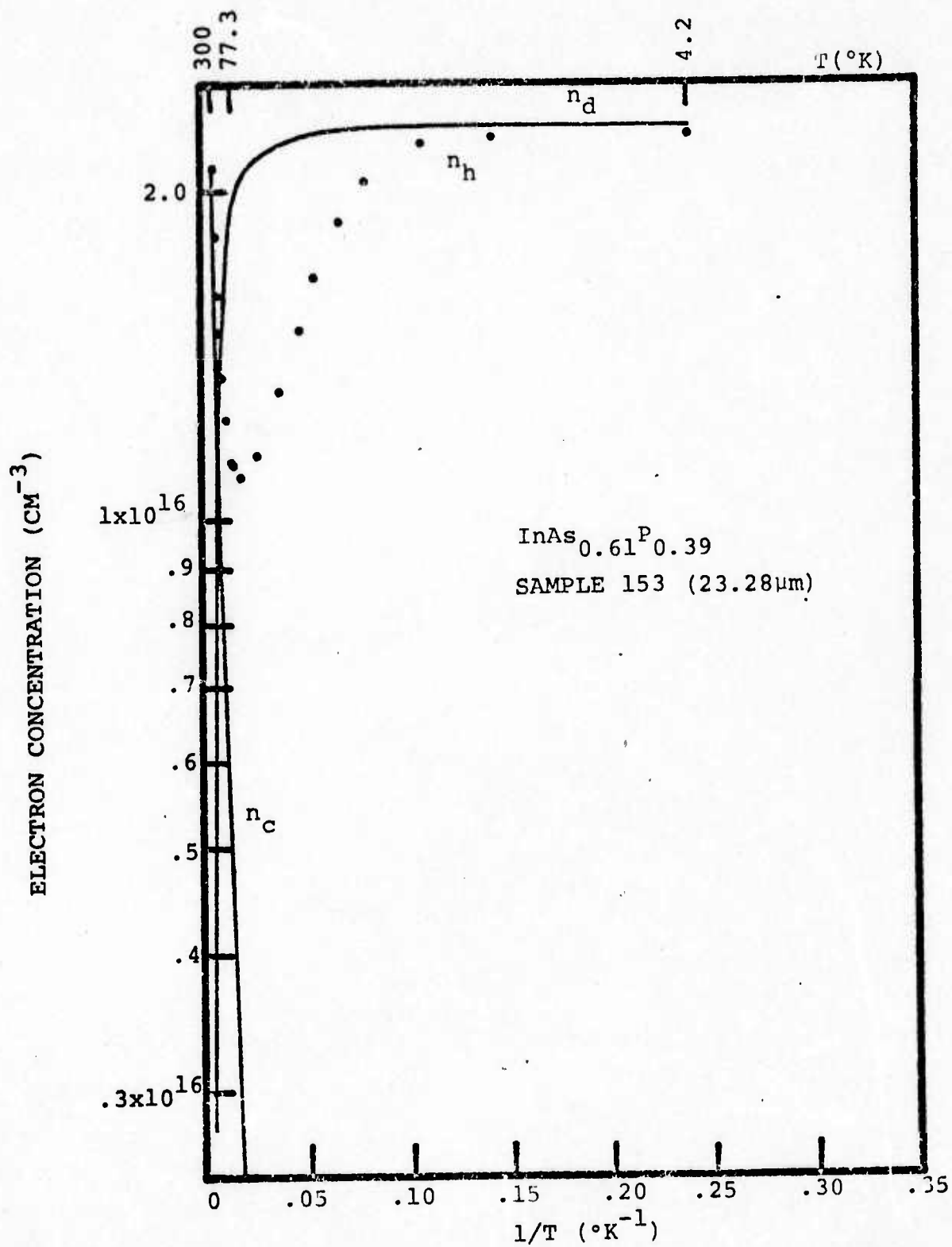
FIGURE 4.25 ELECTRON CONCENTRATION IN THE CONDUCTION
AND DONOR BANDS FOR SAMPLE 153
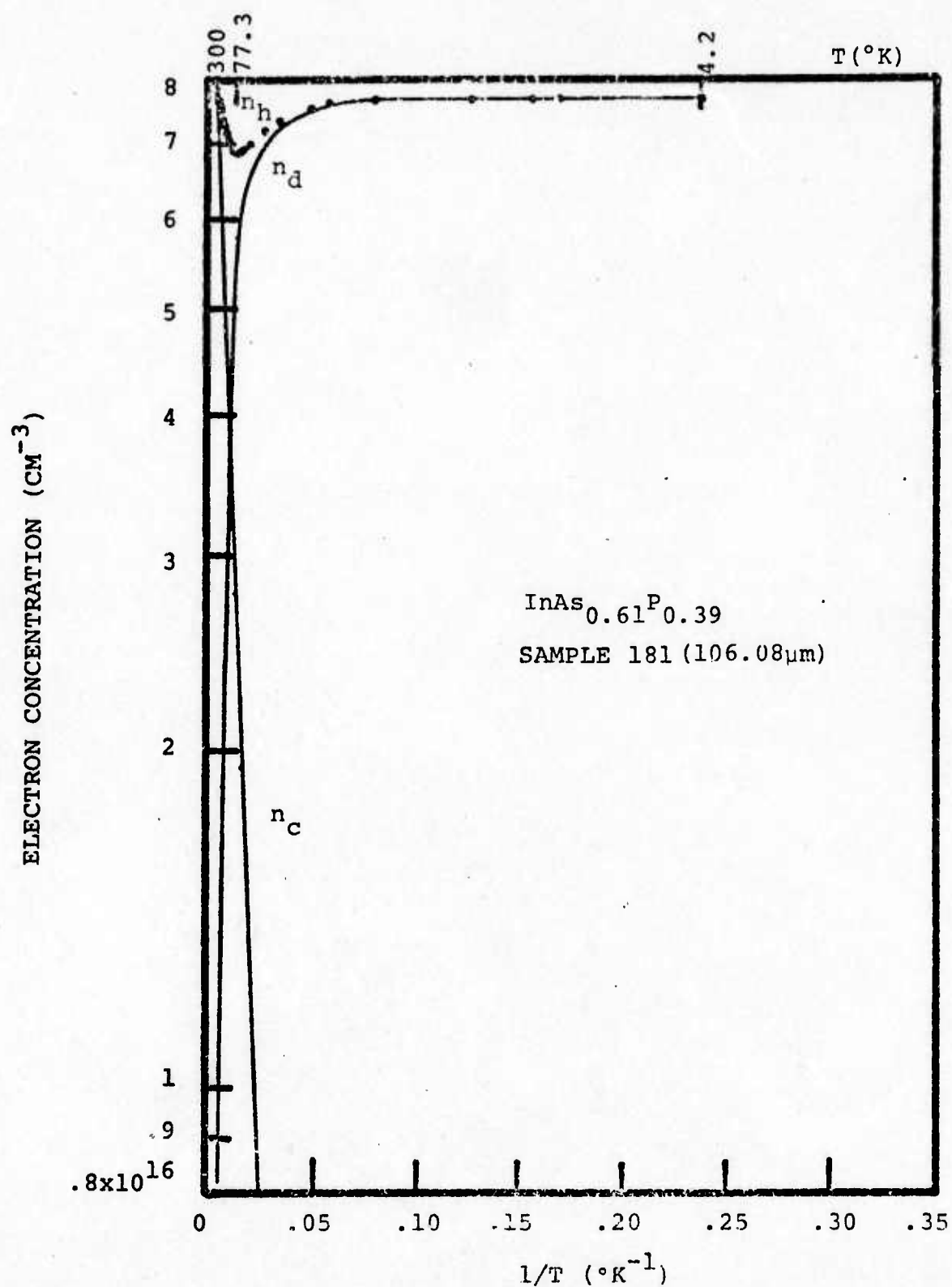
FIGURE 4.26   ELECTRON CONCENTRATION IN THE CONDUCTION
AND DONOR BANDS FOR SAMPLE 181

fitted by least squares to an exponential of the form

$$n_C = A_C \exp(-E_{C_1}/kT) \qquad (4.6)$$

The results for A_C and E_{C_1} obtained by this method are listed in Table 4.2 along with b, the mobility ratio. It should be noted that samples 173, 175, 177, 178, 196 and 186 were only measured from 77.3 to 300K. Because of their incomplete curves the analysis is only an approximation. The values for E_{C_1} show definite trends and are plotted in Fig. 4.27 for the first three groups of samples. For the 3 μm (172-178) and 9 μm (164-171) samples there is an almost linear decrease of E_{C_1} with increasing flow rate. For the 22 μm (153-159) samples the value of E_{C_1} increases with increasing flow rate. Similar type trends were observed in the analysis of resistivity (Fig. 4.12). Again the sample characteristics seemed to be governed by not only the hydrogen flow rate but also the epitaxial thickness. The interpretation of these trends in E_{C_1} is not so clear cut as indicated by Section 2.3b. The exponential dependence of the conduction electrons is described by Eqn. 2.26. The slopes of the curves generated from this equation (Fig. 2.12) are varied by changes in the total impurity level and by changes in the compensation ratio. Thus an increase in E_{C_1} indicates an increase in the impurities, an increase in the compensation, or some combination of these two.

TABLE 4.2

	$\underline{b}(\mu_c/\mu_d)$	$\underline{A_c}$	$\underline{E}_{c_1}$ (meV)
172	4.94	9.74	14.76
173*	5.18	5.72	17.83
174	5.82	8.77	19.37
175*	10.57	5.45	24.67
176	8.42	10.26	24.45
177*	4.90	11.95	25.31
178*	3.48	15.45	26.74
164	2.39	8.76	6.90
168	4.04	4.17	8.62
166	4.37	3.81	10.59
169	6.31	4.20	12.59
170	9.49	2.65	15.06
171	8.72	5.52	15.99
153	6.31	4.43	20.95
154	6.31	4.33	18.68
155	5.74	5.92	16.69
156	5.14	4.09	14.71
157	5.63	3.80	13.71
159	7.36	3.58	13.61
196*	2.20	8.98	9.62
197	2.23	5.70	6.00
181	2.01	10.81	8.49
186*	3.04	5.94	12.85

*indicates analysis from incomplete data
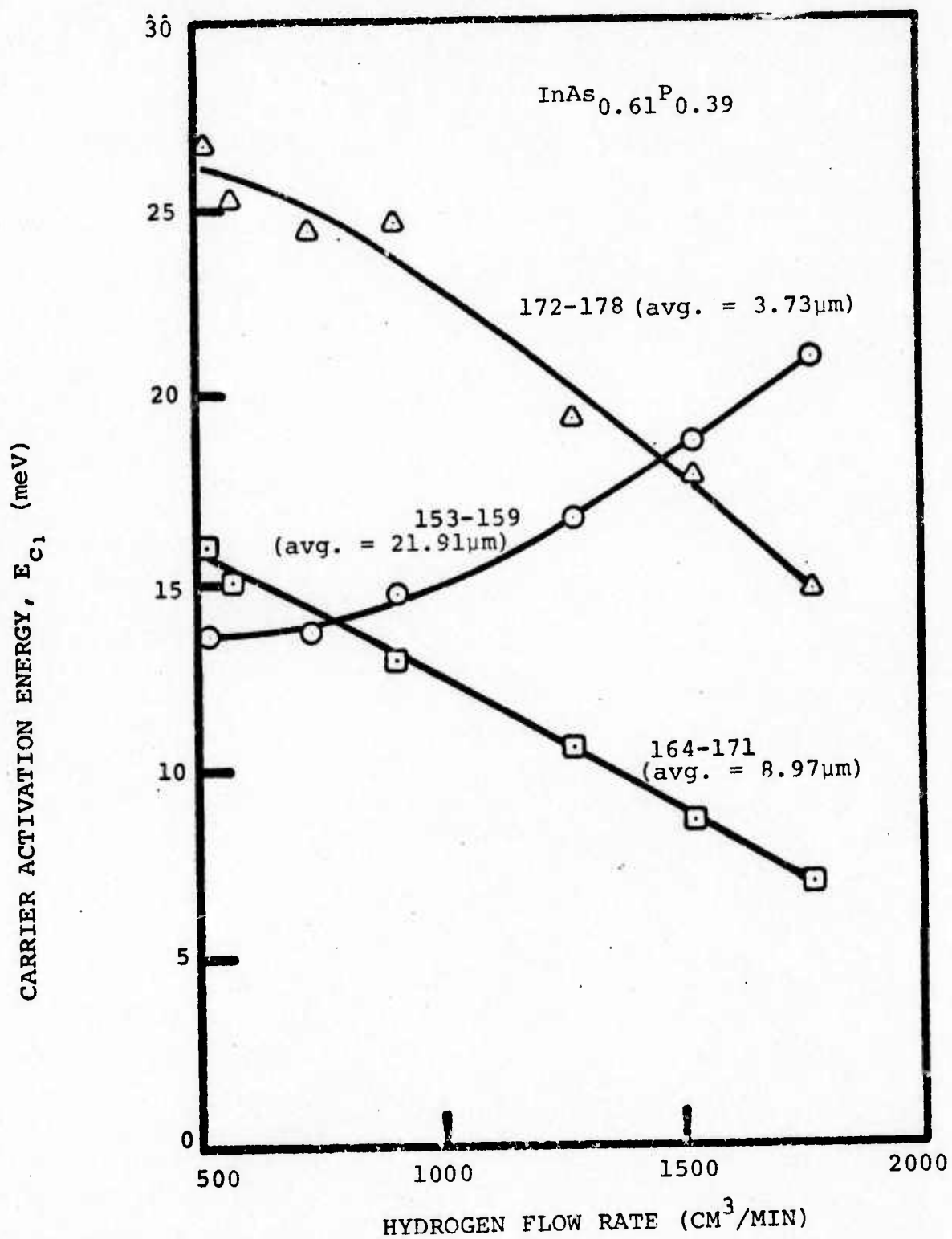
FIGURE 4.27   CARRIER ACTIVATION ENERGY, E_{c_1}, VERSUS
HYDROGEN FLOW RATE

4.4 Mobility

The mobility of electrons in $InAs_{0.61}P_{0.39}$ may be calculated from the resistivity and Hall coefficient data by the following relation

$$\mu_h = \frac{R_h}{\rho} \tag{4.7}$$

This is called the Hall mobility. The actual drift mobility may be found by dividing μ_h by the scattering factor r. Since r is assumed to be unity for all temperatures the two mobilities are assumed equal for convenience. The experimental curves derived by using Eqn. 4.7 are shown in Figs. 4.28 to 4.32 plotted against inverse absolute temperature. The curves show a sharp initial increase with decreasing temperature until a peak is reached at approximately 100K. The mobility then falls exponentially until around 20K. For temperatures below 20K the mobility becomes almost constant. These curves are seen to compare well with Fig. 2.7 which is the theoretical mobility derived from a combination of polar optical phonon, ionized impurity, and neutral impurity scattering. The agreement indicates these three scattering mechanisms contribute to the mobility in the epitaxial layers.

The high temperature portion of the mobility curves may be best approximated by a power equation such as

$$\mu = aT^{-\beta} \tag{4.8}$$

A least squares fit of the mobility data from 300 to 200K
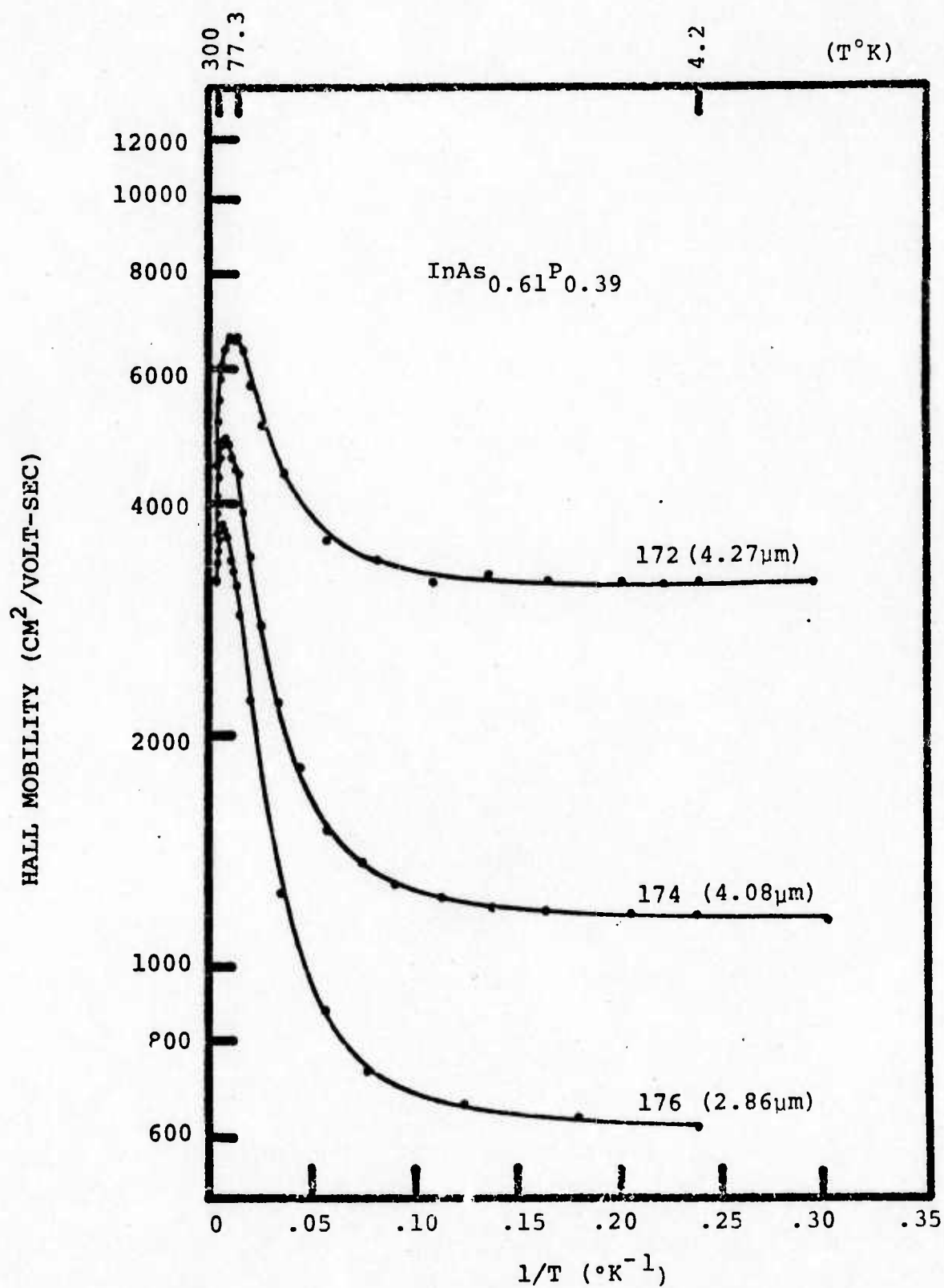
FIGURE 4.28   HALL MOBILITY OF SAMPLES 172, 174, 176
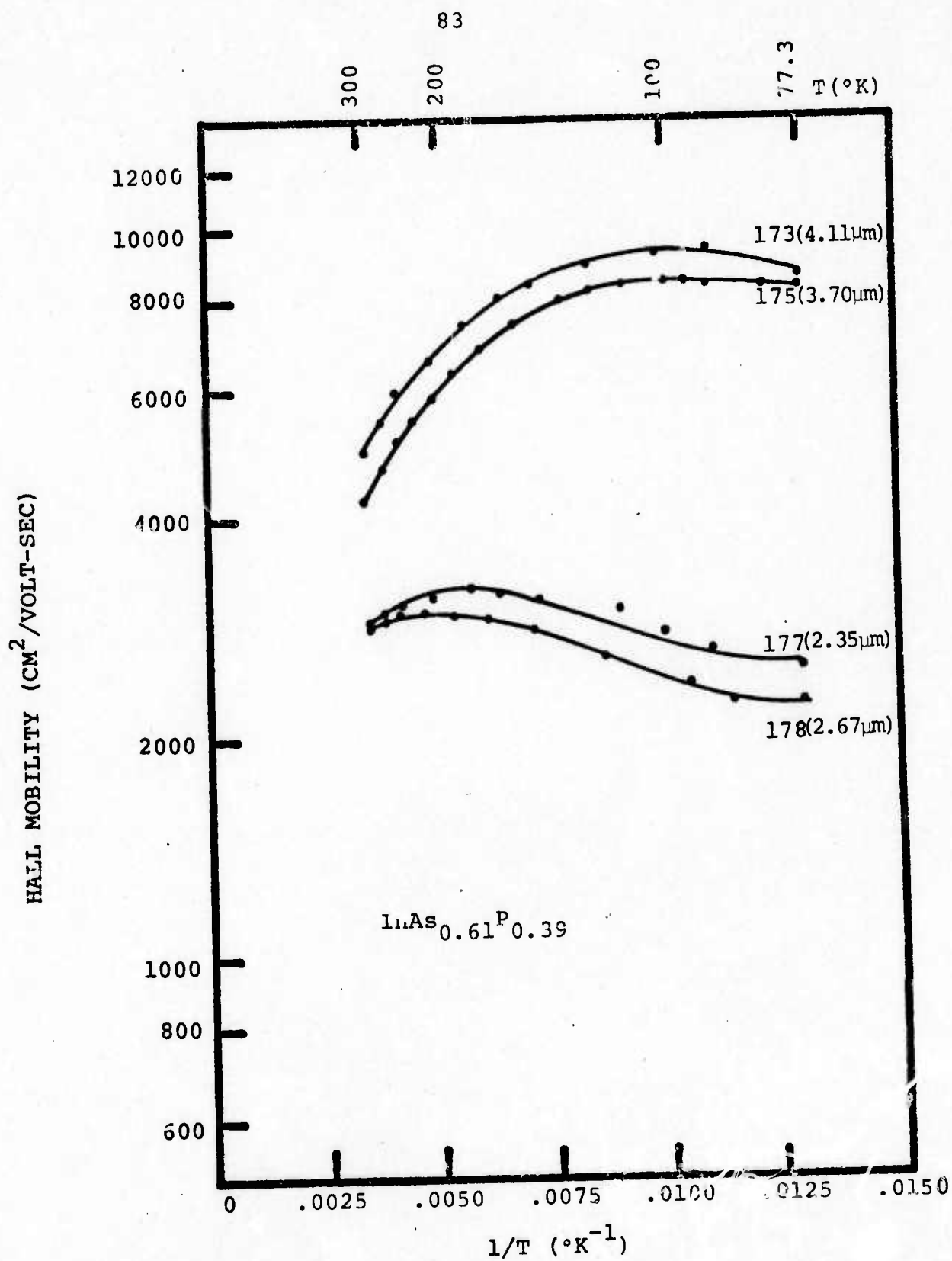
FIGURE 4.29   HALL MOBILITY OF SAMPLES 173, 175, 177, 178
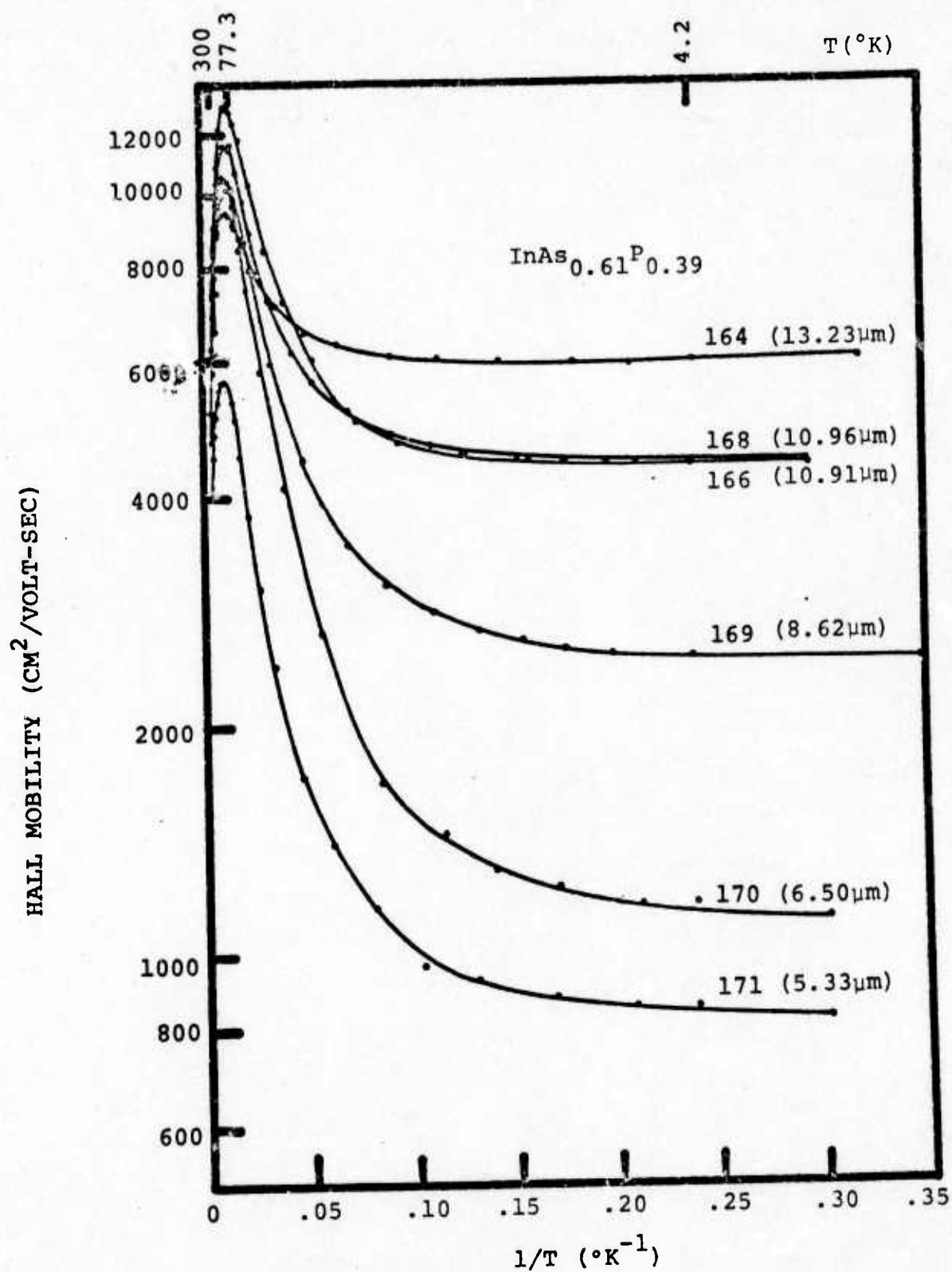
FIGURE 4.30 HALL MOBILITY OF SAMPLES 164-171
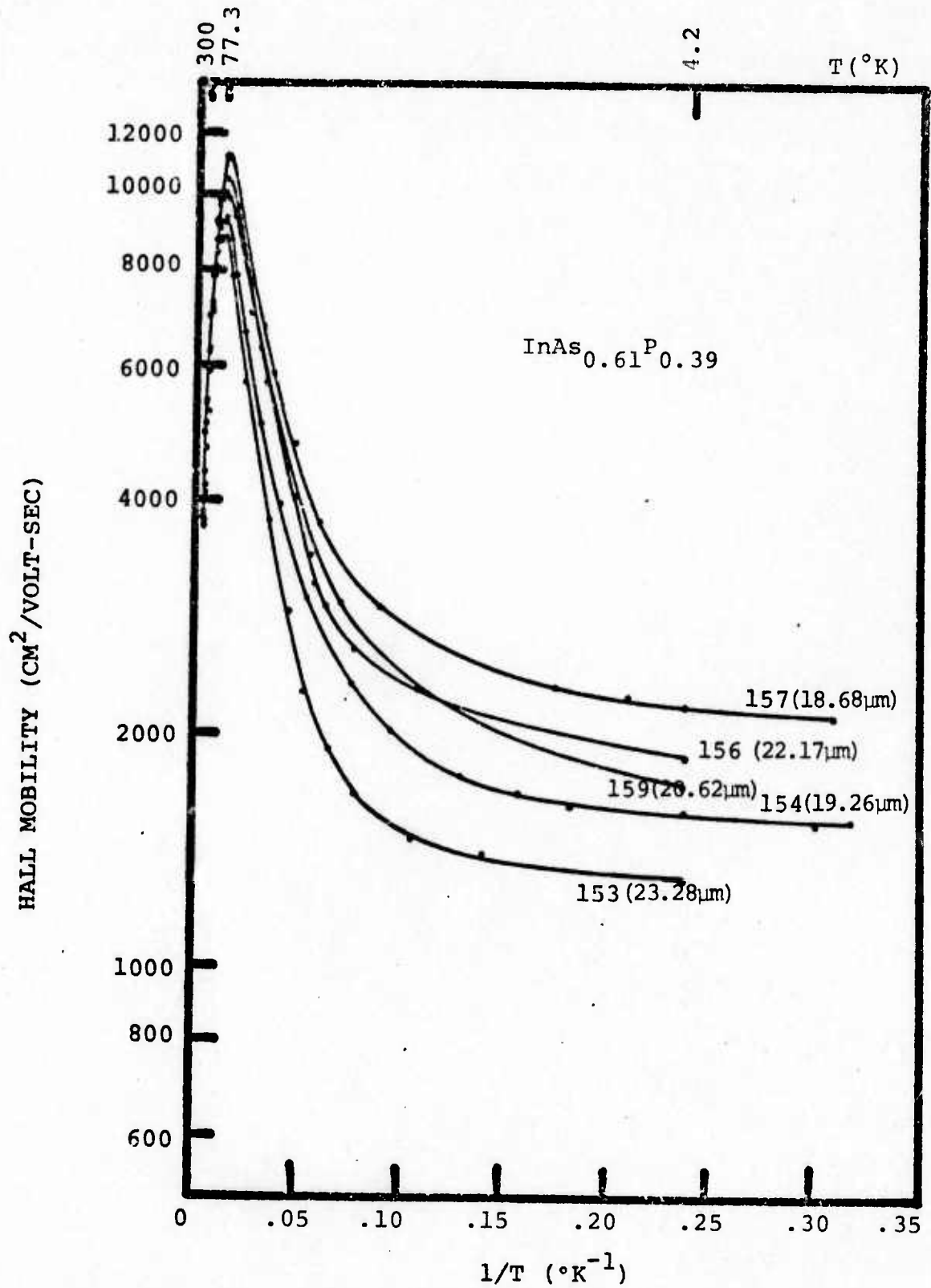
FIGURE 4.31   HALL MOBILITY OF SAMPLES 153-159
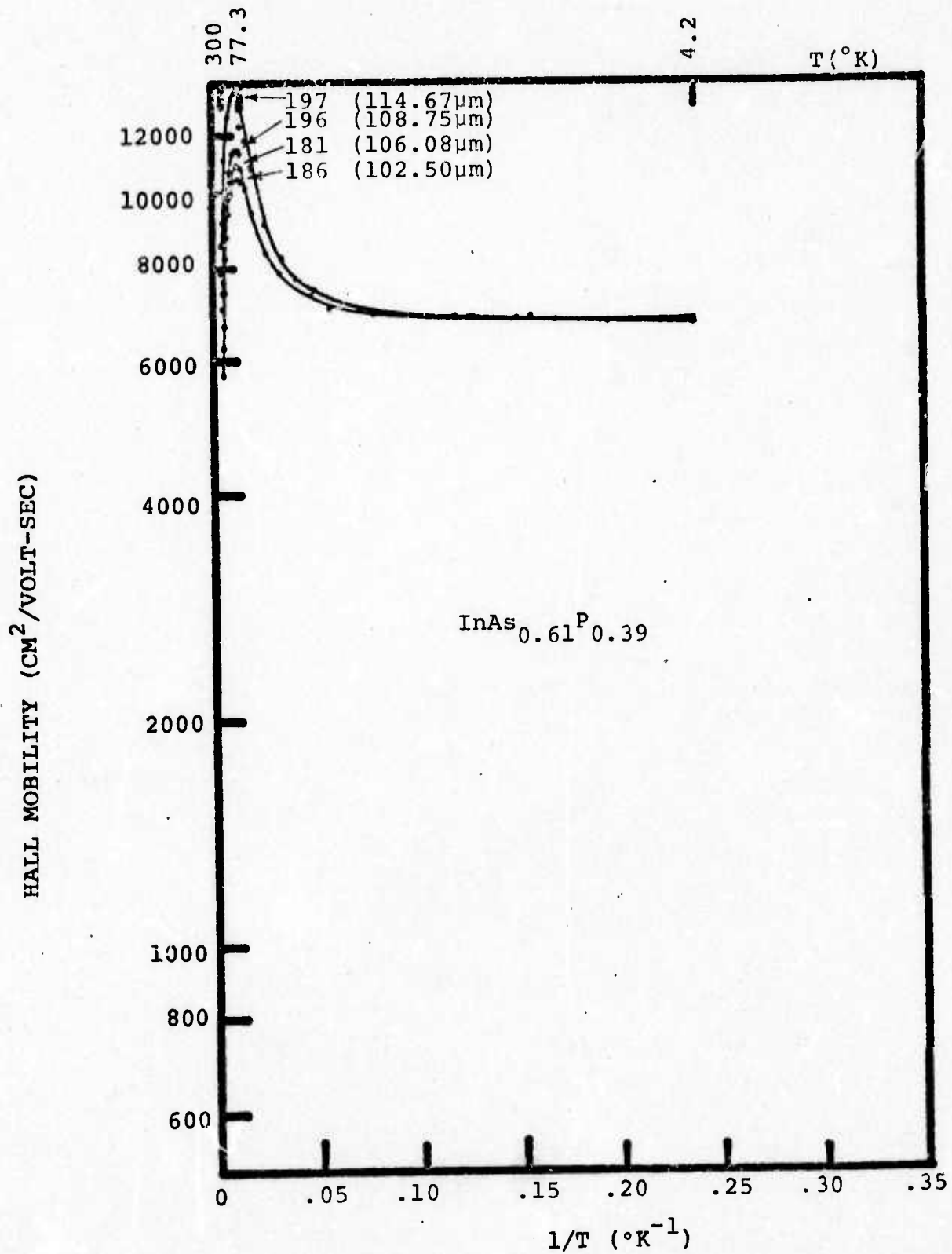
FIGURE 4.32   HALL MOBILITY OF SAMPLES 196-186

was made for each sample to determine the parameters a and β. From the theoretical dependence of β on the impurity concentration, N_i (shown in Fig. 2.5), the values for total impurities contained in each sample could be found. Because of the approximations, it should be emphasized again that the value obtained will also be only approximate. With the relations

$$N_i = N_d + N_a \qquad (4.9)$$

$$n_{max} = N_d - N_a \qquad (4.10)$$

the concentration of donor and acceptor impurities could be found. A list of the values derived from this analysis of the mobility curves is contained in Table 4.3.

Some general trends in these results should be noted and compared to the results from the carrier concentration analysis. The total impurity concentration and donor compensation in samples 172-178 show an increase with decreasing flow rates. This is directly correlated to the increase of E_{c1} with decreasing flow rate in Fig. 4.27. The samples 164-171 show a similar increase in compensation but some scatter in the impurity concentration. The samples 153-159 show both a decreasing impurity concentration and a decreasing compensation level with decreasing flow rate which corresponds also to the decrease in E_{c1} with decreasing flow rate. The last set (196-186) shows too much scatter to see definite trends.

TABLE 4.3

Sample	a	β	$N_i (cm^{-3})$	$N_d (cm^{-3})$	$N_d (cm^{-3})$	Na/Nd
172	1.31×10^5	.59	12.65×10^{16}	9.31×10^{16}	3.34×10^{16}	.36
173	5.15	.82	8.65	5.88	2.77	.47
174	.71	.52	13.40	9.14	4.26	.47
175	51.60	1.25	3.80	3.07	.73	.24
176	.23	.35	19.11	12.79	6.32	.49
177	.16	.30	20.56	12.65	7.92	.63
178	.12	.25	22.35	14.12	8.24	.58
164	1.37	.55	13.74	10.41	3.33	.32
168	5.41	.79	9.00	6.21	2.79	.45
166	8.64	.86	7.91	5.40	2.51	.47
169	5.53	.82	8.49	5.74	2.75	.48
170	8.48	.91	7.40	4.63	2.77	.60
171	.94	.55	13.30	9.09	4.21	.46
153	8.48	.95	5.91	4.10	1.81	.44
154	8.10	.92	6.27	4.26	2.01	.47
155	4.39	.83	7.38	5.59	1.79	.32
156	18.90	1.09	5.05	3.78	1.27	.33
157	17.60	1.07	5.15	4.00	1.15	.29
159	16.50	1.07	5.15	4.19	.96	.23
196	3.01	.66	11.17	8.78	2.39	.27
197	3.97	.69	10.60	7.58	3.02	.10
181	2.76	.65	11.25	9.49	1.76	.19
186	6.25	.83	8.44	6.10	2.34	.38

CHAPTER V

EXPERIMENTAL RESULTS OF $InAs_{1-x}P_x$

5.1 Sample Description

A fifth set of samples were grown using the methods described in Chapter III with the arsine to phosphine ratio varied so as to produce samples of varying composition. These samples (147-152) were grown at a constant hydrogen flow rate of 2100 cm^3/min on semi-insulating GaAs substrates. Though the deposition time for each sample was held constant, the resultant epitaxial thicknesses were seen to be strongly dependent on the composition. A plot of this experimental variation from Table 3.1 is shown in Fig. 5.1 where it is seen that the growth of phosphorus-rich layers is strongly favored. From the results of $InAs_{0.61}P_{0.39}$, it would be expected that this thickness variation would affect the transport characteristics of these samples due to the interface states.

Another noticeable physical variation was the quality of the surfaces of the epitaxial layers. The surfaces definitely degenerated as the phosphorus content increased. The surfaces of the arsenic-rich samples (147, 148) could be characterized as dull but yet smooth. As the phosphorus content increased the surfaces tended to become more shiny
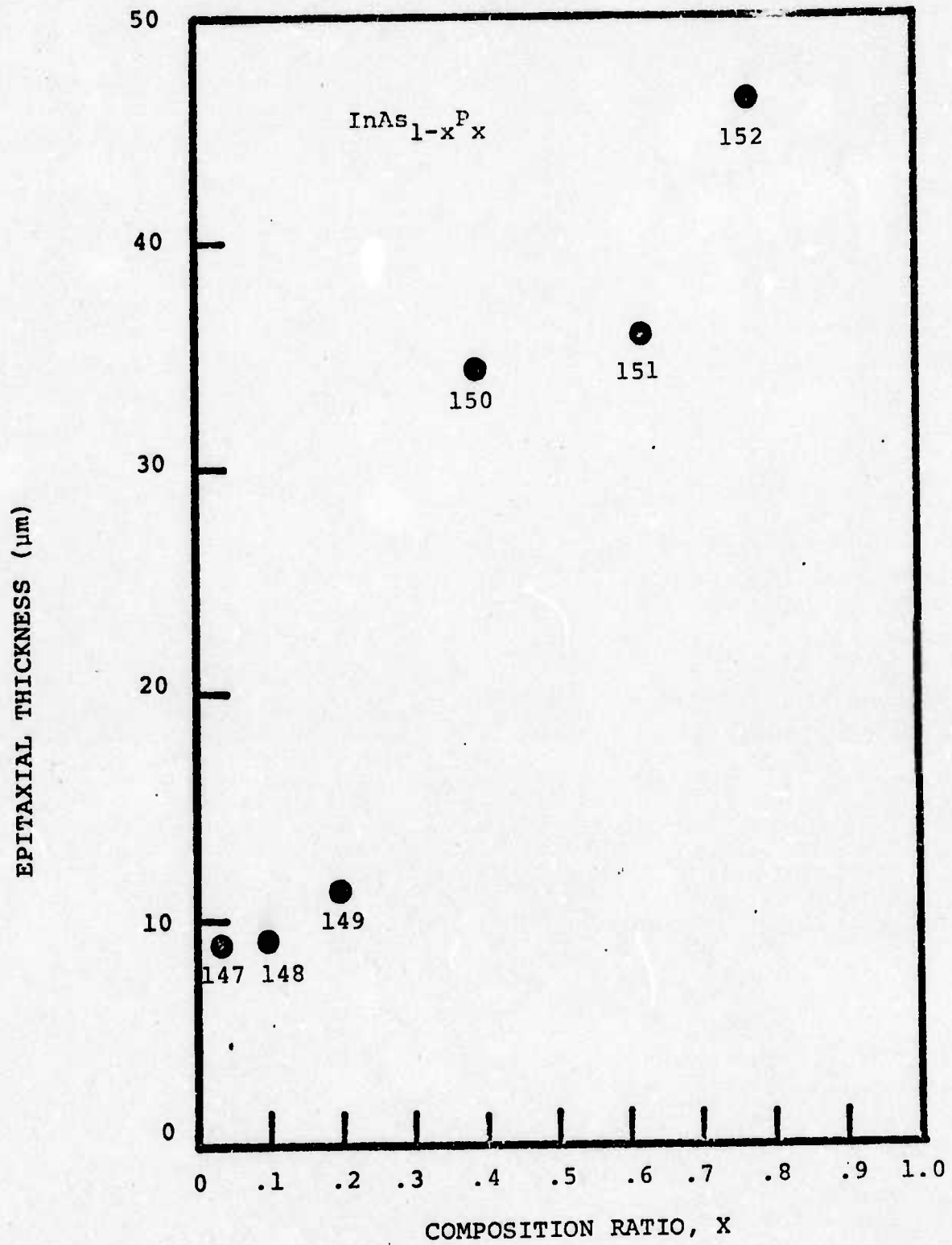
FIGURE 5.1 VARIATION OF EPITAXIAL THICKNESS WITH ALLOY COMPOSITION

but were plagued by large surface irregularities (hillocks).

5.2 Resistivity Data

Resistivity measurements were made on the samples of Group V over the temperature range from 4.2K to 300K. The results of these measurements are shown in Fig. 5.2 as functions of inverse absolute temperature. The results show an increase of resistivity from 0.15 ohm-cm for sample 147 to 0.1 ohm-cm for sample 152 at room temperature. As functions of inverse temperature, the curves decrease exponentially from 300K to 200K, reach a minimum at approximately 80K, then increase exponentially until 20K where they saturate and show a slight linear dependence with decreasing temperature.

The resistivity in the low temperature region below 80K may be approximate by the equation

$$\rho^{-1} = C_2 \exp \left(-E_2/kT\right) + C_3 T + C_4 \qquad (5.1)$$

A least squares fit was used to determine the constants C_2, C_3, C_4 and the conductivity activation energy E_2. The results of this fit are listed in Table 5.1 and a plot of the activation energy E_2 is shown in Fig. 5.3 as a function of the alloy composition.

5.3 Hall Coefficient and Carrier Concentration

The Hall coefficient was measured for this set of samples at a magnetic field strength of 5 kilogauss over
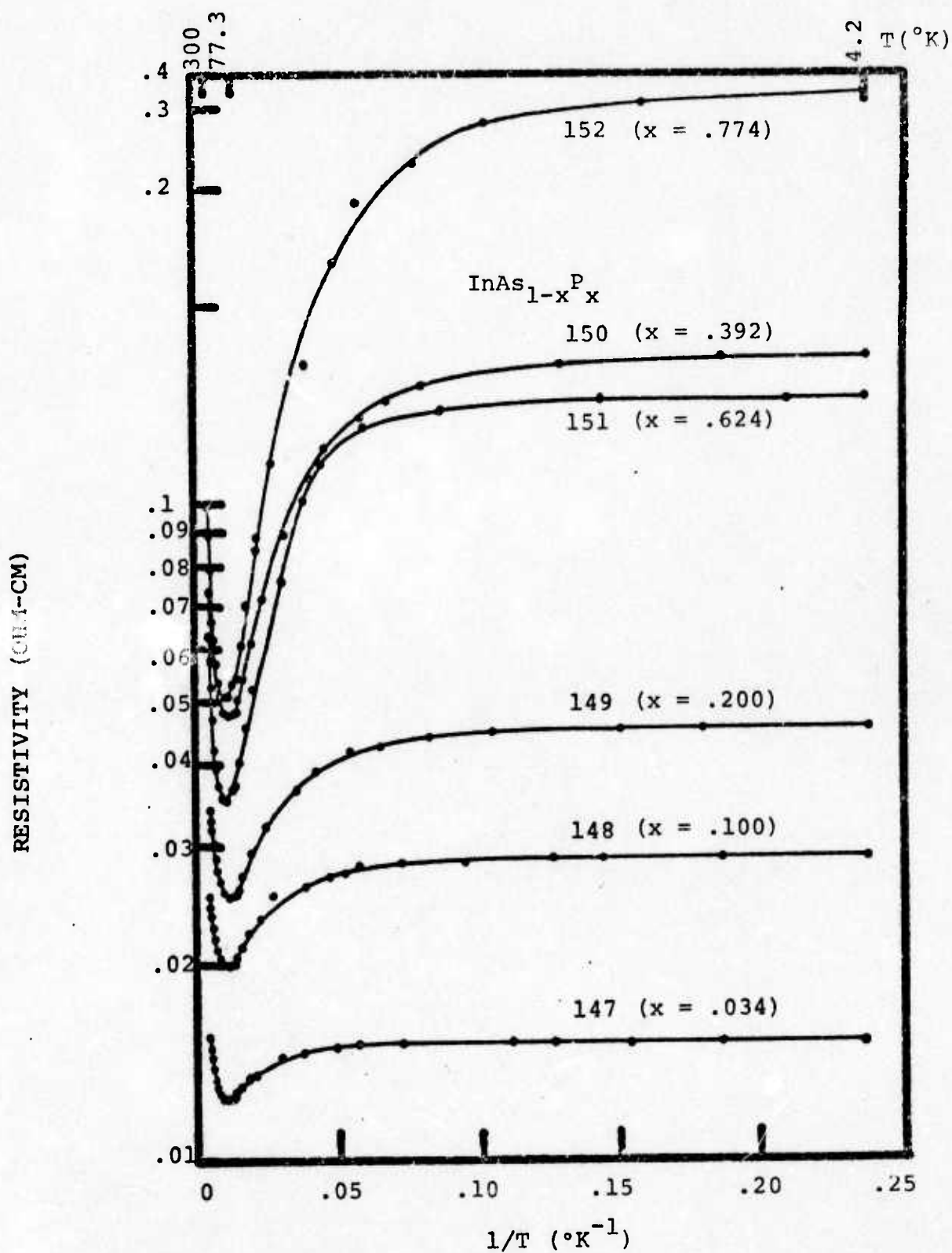
FIGURE 5.2   RESISTIVITY OF SAMPLES 147-152
WITH INVERSE TEMPERATURE

TABLE 5.1

CONDUCTIVITY PARAMETERS

$$\rho(T)^{-1} = C_2 \exp(-E_2/kT) + C_3 T + C_4 \qquad (T < 80K)$$

SAMPLE	X	C_2	E_2 (meV)	C_3	C_4
147	.034	86.9	0.68	.077	65.31
148	.100	60.9	1.46	.090	33.97
149	.200	52.7	2.36	.092	21.44
150	.392	34.8	3.59	.107	5.42
151	.624	54.5	4.82	.057	6.62
152	.774	38.8	5.10	.084	1.93
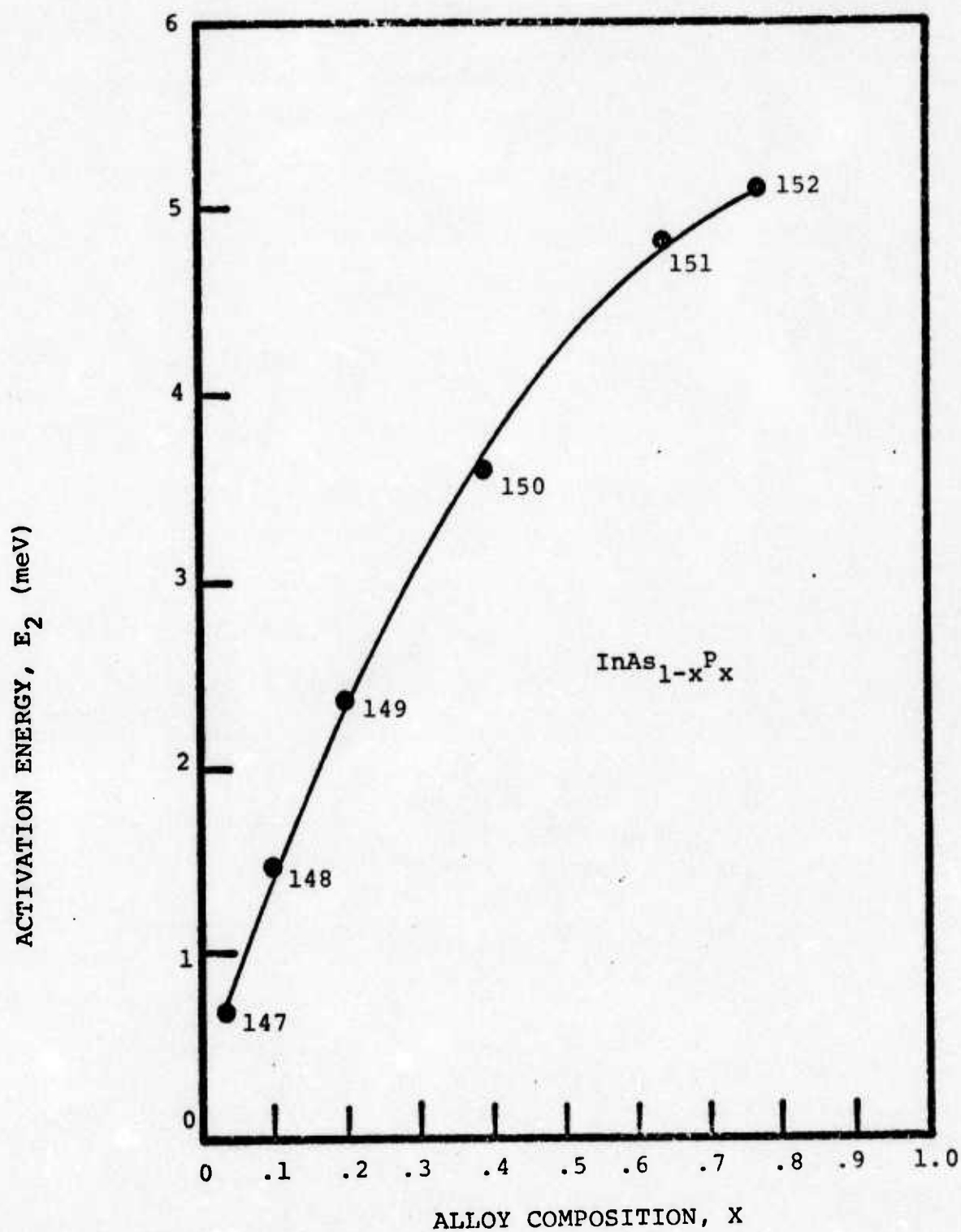
FIGURE 5.3   VARIATION OF ACTIVATION ENERGY, E_2, WITH ALLOY COMPOSITION

the temperature range from 4.2K to 300K. The temperature dependence of this set are shown in Fig. 5.4 where it is seen that the curves show an overall increase as the percentage of phosphorus increases within the epilayer. Of particular interest is the shift of the Hall maximum as a function of composition. The maximum occurs at about 115K for sample 147 and decreases to approximately 38K for sample 152. A Hall maximum occuring at high temperatures indicates in general an increase in the impurity content as indicated in Section 2.2c. The temperatures for the Hall maximum of each sample are given in Table 5.2.

The free electron concentration was calculated from the Hall coefficient using the relation:

$$n_h = \frac{1}{e R_h} \tag{5.2}$$

The results, Fig. 5.5, show that the concentrations were between about $1 \times 10^{16} cm^{-3}$ to $5 \times 10^{16} cm^{-3}$ for all samples. The concentration increased as the samples became more arsenic rich. Using the analysis shown in Section 2.2c, the electron concentrations in both the donor and conduction bands. The exponential decrease of carriers in the conduction band was fitted to the equation:

$$n_c = A_c \exp (-E_{c_1}/kT) \tag{5.3}$$

The values of the mobility ratio, $b = \mu_c/\mu_d$, the coefficient
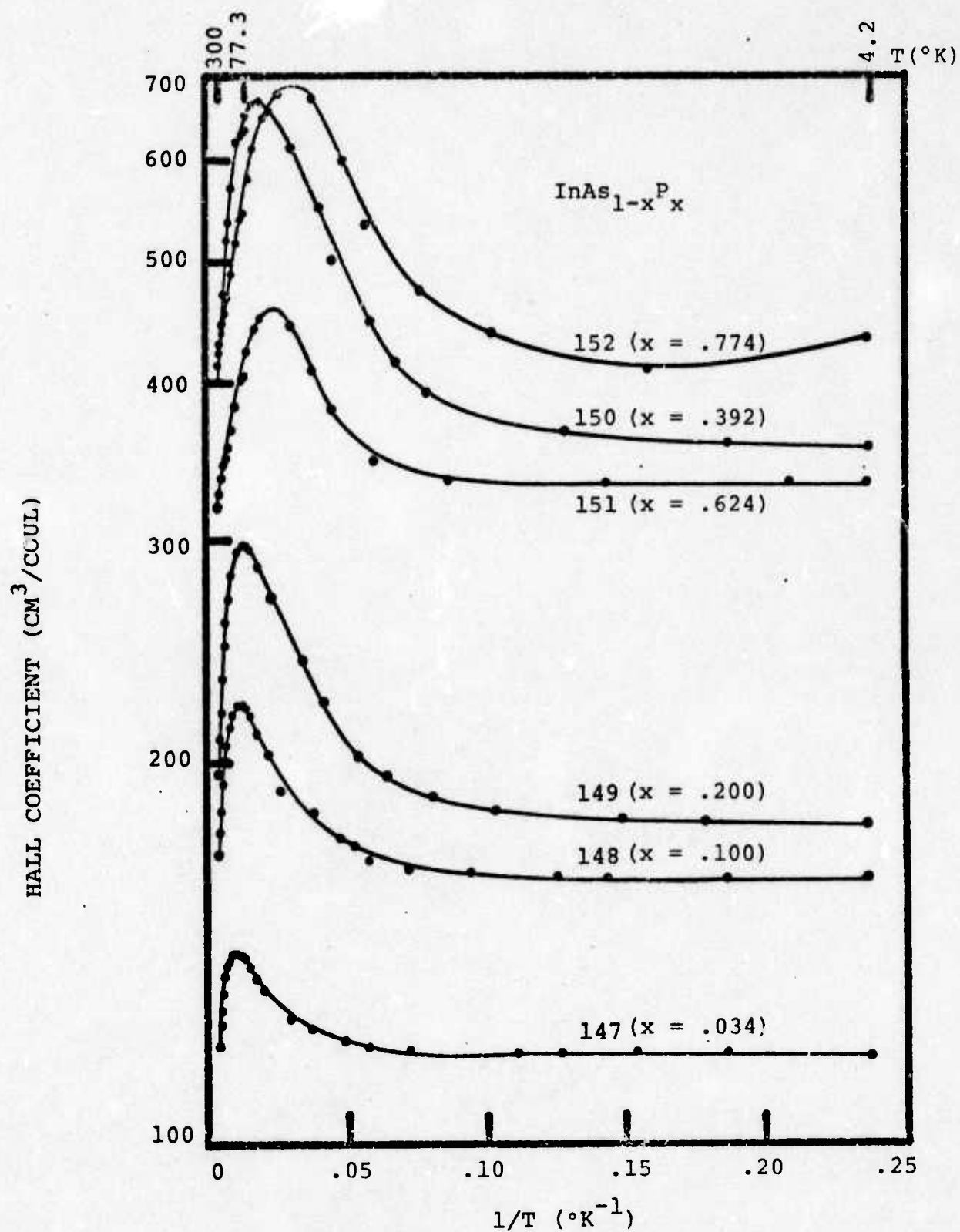
FIGURE 5.4   HALL COEFFICIENT OF SAMPLES 147-152 WITH
INVERSE TEMPERATURE

TABLE 5.2

SAMPLE	$T_{R_{max}}$	$b(\mu_c/\mu_d)$	A_c	E_{c_1} (meV)
147	115K	2.45	11.54	21.6
148	90K	3.23	7.85	20.9
149	73K	4.47	6.27	20.0
150	57K	5.39	2.50	14.5
151	52K	3.39	2.44	5.9
152	38K	4.35	1.82	5.1
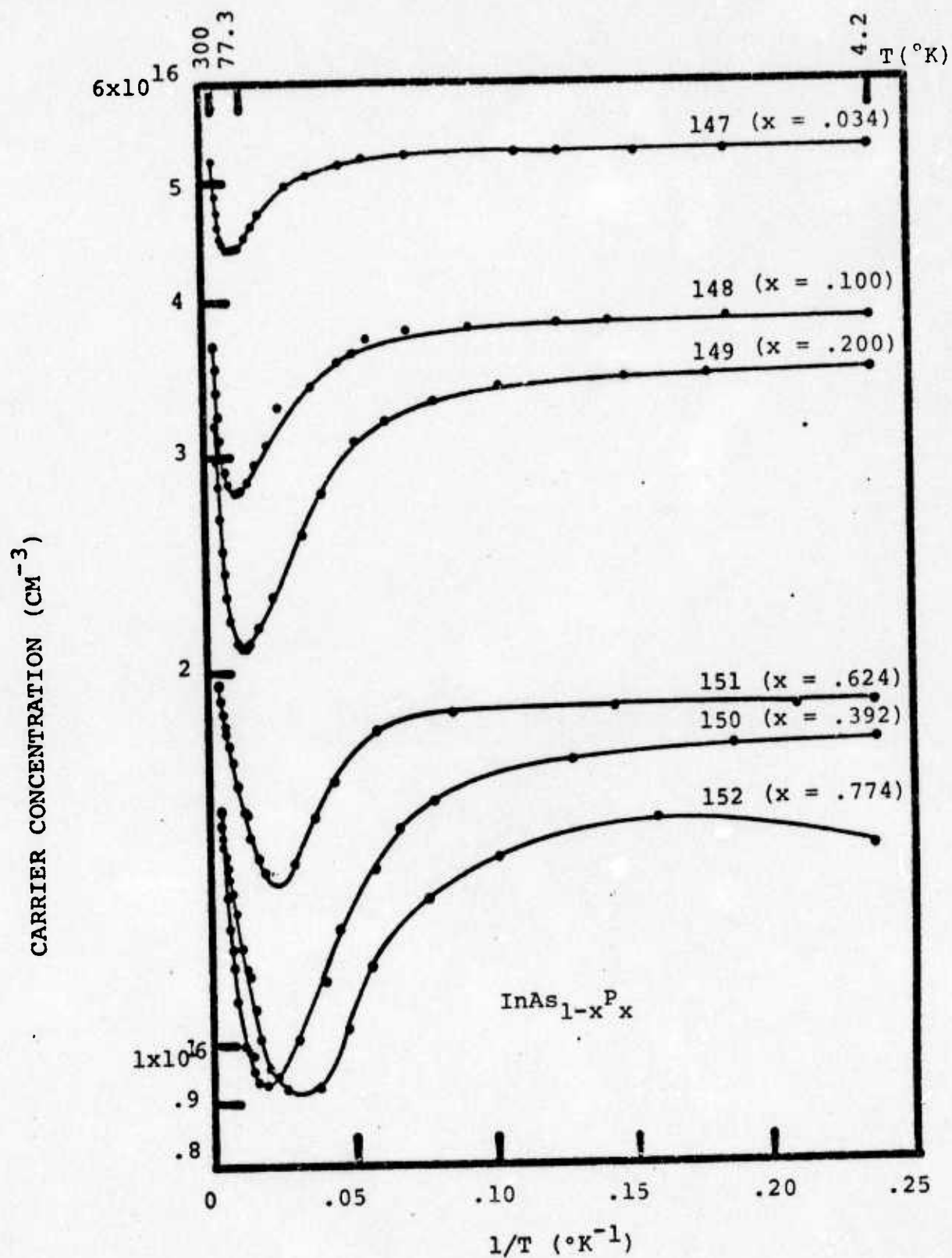
FIGURE 5.5   CARRIER CONCENTRATION OF SAMPLES 147-152
WITH INVERSE TEMPERATURE

A_c, and the activation energy, E_{C_1}, are also given in Table 5.2. In Fig. 5.6, E_{C_1} is plotted as a function of alloy composition. As was discussed previously, an increase in E_{C_1} may be indicative of increased impurity content, increased compensation, or a combination of these two. The high values of E_{C_1} for the sample 147-149 are most likely a result of their decreased thickness where interface states might be a more dominant factor in controlling the transport properties.

5.4 Mobility

The electron mobility for Group V samples was calculated using the relation

$$\mu_h = \frac{R_h}{\rho} \tag{5.4}$$

The results, Fig. 5.7, show mobilities as high as 13,000 cm^2/volt-sec for sample 150 at 77K. Because of the low effective mass for InAs, it would be expected that the mobility of the arsenic-rich samples would be quite high. The mobilities at 300K are plotted against alloy composition in Fig. 5.8. A theoretical curve for that temperature, derived from Ehrenreich,[20] is also shown. Ehrenreich's curve is based on polar optical scattering and ionized impurity scattering (Conwell-Weisskopf formula[17]) using $N_i = 5 \times 10^{16} cm^{-3}$. The fit for large x is acceptable but there is an obvious departure from the theory for samples 147-149.
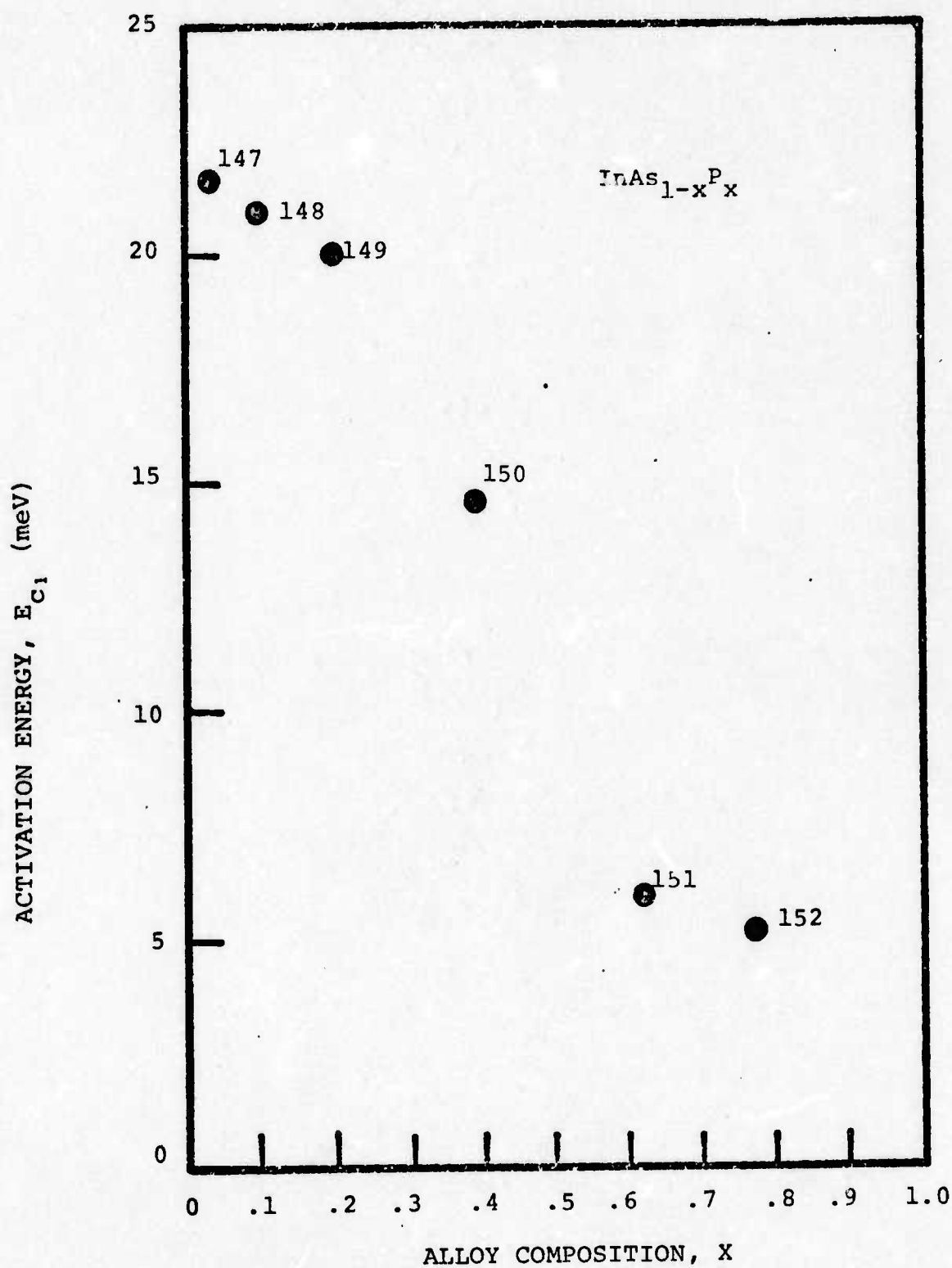
FIGURE 5.6 VARIATION OF ACTIVATION ENERGY, E_{c1}, WITH ALLOY COMPOSITION
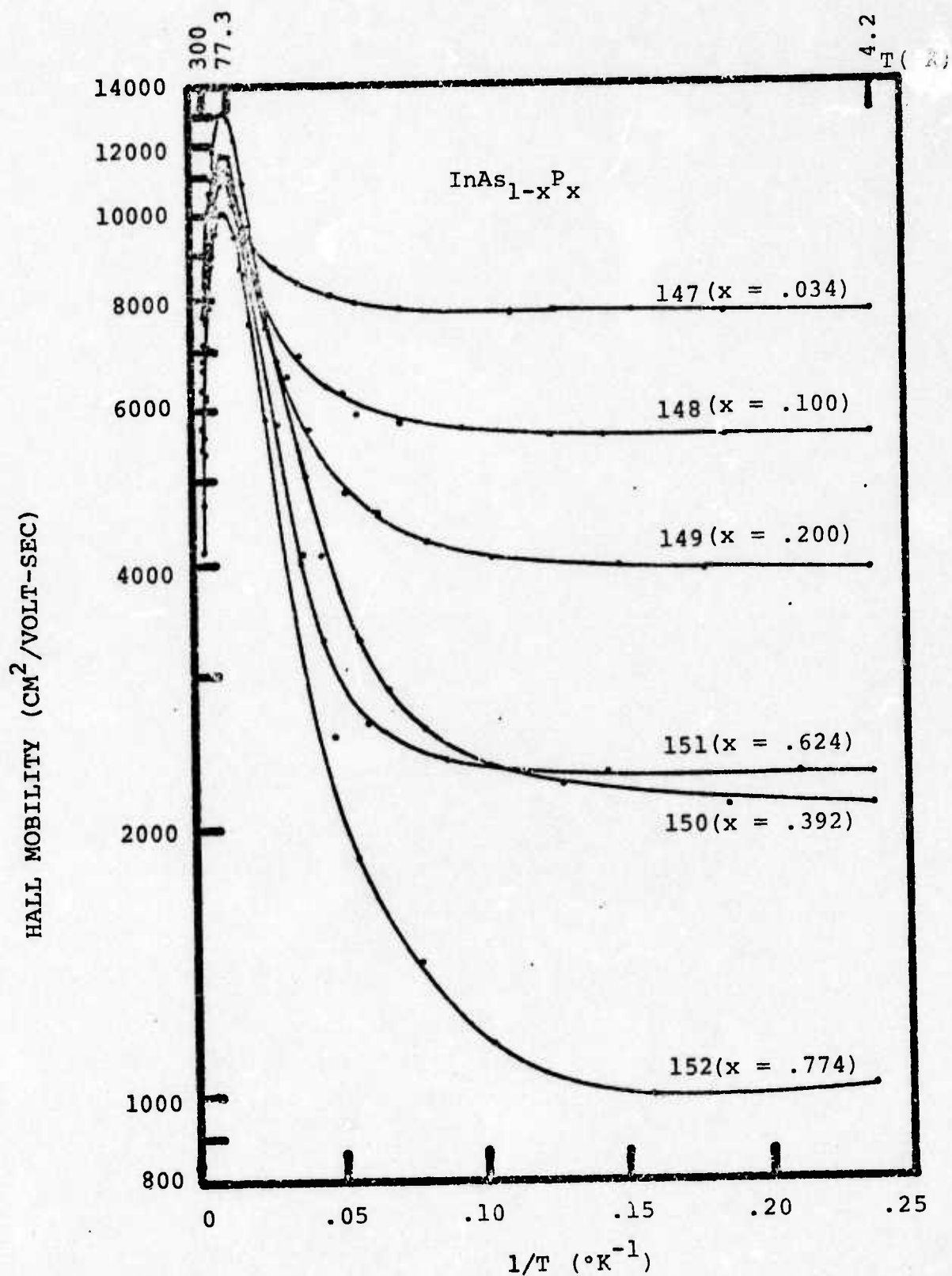
FIGURE 5.7   HALL MOBILITY OF SAMPLES 147-152 WITH
INVERSE TEMPERATURE
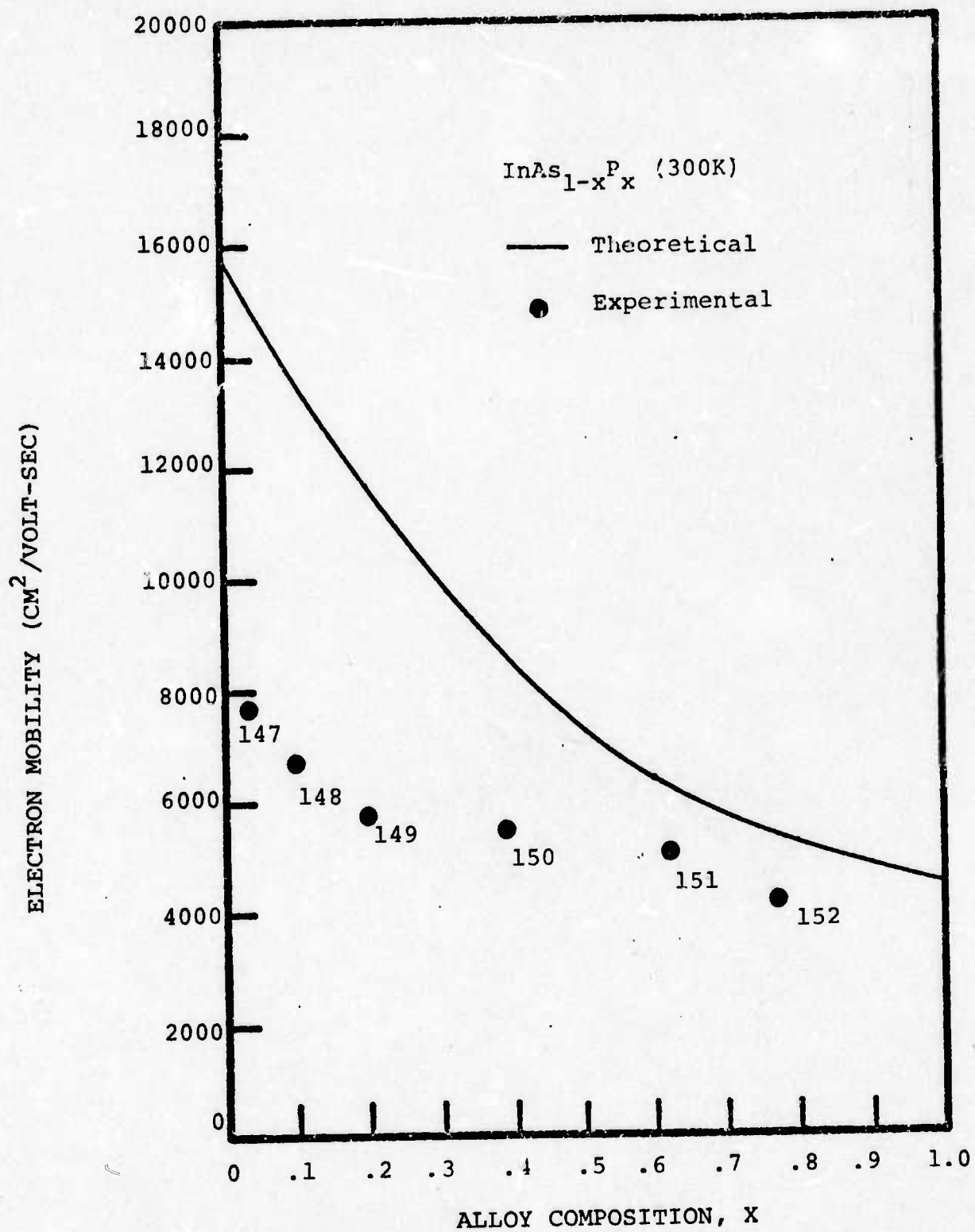
FIGURE 5.8   COMPARISON OF HALL MOBILITY TO
THEORETICAL MOBILITY AT 300K

This might be explained by an increase in N_i due to either lattice mismatch or the interface states.

The high temperature portion of the mobility curves (200K-300K) was fitted by least squares to the power equation

$$\mu = aT^{-\beta} \tag{5.5}$$

The results for a and β in Table 5.3 show an increase in both parameters as the phosphorus content increases. The β values are well below those given in Section 2.1a for polar optical phonon scattering, indicating that ionized impurity scattering is quite effective in these samples even at room temperature.

TABLE 5.3

$$\mu = aT^{-\beta} \quad (200\text{-}300K)$$

SAMPLE	$\underline{a}$	$\underline{\beta}$
147	2.55×10^5	.615
148	3.68	.705
149	8.04	.868
150	12.01	.950
151	13.83	.988
152	29.09	1.152

CHAPTER VI

CONCLUSIONS

There are several conclusions which may be drawn from the experimental results of electron transport in both $InAs_{0.61}P_{0.39}$ (Chapter IV) and $InAs_{1-x}P_x$ (Chapter V). A comparison of the theoretical and experimental results shows that the mobility may be adequately described by the interactions of optical phonon, ionized impurity, and neutral impurity scattering over the whole temperature region studied. It is suggested that any further or similar work should include regions of higher temperature for two reasons. First, the true effect of polar optical phonon scattering could be seen more easily and thus extracted from the experimental mobility at lower temperatures. This would result in a more accurate knowledge of the effects of ionized impurity scattering. Second, higher temperatures would push the carrier concentration well into the exhaustion range where a more accurate figure for N_d-N_a could be obtained. The basic problem with higher temperatures is that of electrical contacts to the samples. Spring-type contacts to small indium dots on the sample could be a possible solution. Metals with higher melting temperatures than indium could be tried for direct wire connections.

All samples investigated were seen to have a high concentration of impurities which formed a band centered at the donor level, capable of conduction at even the lowest temperatures. The mobility within this band was calculated to be much smaller than the mobility in the conduction band, typically by a factor of 0.2. The compensation of the donor impurities by acceptor states was also evidence with values of N_a/N_d ranging from 0.19 to 0.63. The impurity and compensation levels were governed by two factors - the hydrogen flow rate during the epitaxial growth and the thickness of the epitaxial layers. For the thinner groups of samples the impurity compensation levels increased as the thickness decreased. This effect may be attributed to the interface states due to the lattice mismatch between GaAs and $InAs_{1-x}P_x$. A calculation for $InAs_{0.61}P_{0.39}$ shows that these states would, under ideal conditions, be at least $6.7 \times 10^{12} cm^{-2}$. If they are distributed over, for example, a 1μm transition layer there would be $6.7 \times 10^{16} cm^{-3}$ ionized states in addition to all other impurities. In a 3μm sample this would definitely affect the carrier concentration and mobility. Evidence of this effect is clearly seen in sample 172-178 and in the $InAs_{1-x}P_x$ sample (147-152) where the arsenic-rich epilayers fall short of their expected mobility at 300K. The effect of flow rate variation is more clearly seen in the thicker samples (153-159) where decreasing the flow rate decreases

both the concentration of impurities and the compensation level. The thickest samples (196-186) however were plagued by nonuniform epilayer thicknesses and large surface irregularities.

It is suggested that future research on $InAs_{1-x}P_x$ epitaxial layers should be directed toward decreasing the interface states. This might be accomplished by using different substrates or variations in the substrate orientation. The hydride growth system is easily adapted to composition grading which might also tend to reduce interfacial states.

The results of this research indicate a definite need for better and more controlled growth procedures. The hydride system would seem to be quite useful if these problems could be overcome. However, in spite of the high impurity content, the $InAs_{1-x}P_x$ samples still maintained high mobility levels which is one of their most enhancing features. It is hoped that this work will stimulate more research into the $InAs_{1-x}P_x$ system, especially in respect to device applications.

REFERENCES

1. A. G. Thompson and B. Rose, "Indium-Arsenide-Phosphide Injection Lasers," ONR Final Technical Report, Contract No. N00014-69-C-0415 AD 715454 (1970).

2. H. Sonnenberg, Appl. Phys. Lett., 16, 245 (1970).

3. L. W. James and J. J. Vebbing, Appl. Phys. Lett., 16, 370 (1970).

4. J. B. Gunn, Solid State Comm., 1, 88 (1963).

5. C. Hilsum and H. D. Rees, Electron. Lett., 6, 277 (1970).

6. O. G. Folberth, Z. Naturforsch., 10a, 502 (1955).

7. R. Bowers, J. E. Bauerle, and A. J. Cornish, J. Appl. Phys., 10, 1050 (1959).

8. A. G. Thompson, J. E. Rowe, and M. Rubenstein, J. Appl. Phys., 40, 3280 (1969).

9. J. J. Tietjen, H. P. Maruska, and R. B. Clough, J. Electrochem. Soc., 116, 492 (1969).

10. H. A. Allen and E. W. Mehal, J. Electrochem. Soc., 117, 1081 (1970).

11. H. A. Allen, J. Electrochem. Soc., 117, 1417 (1970).

12. J. M. Ziman, Electrons and Phonons, Oxford U.P., London (1962).

13. D. J. Howarth and E. H. Sondheimer, Proc. Roy. Soc., A219, 53 (1953).

14. H. Ehrenreich, J. Phys. Chem. Solids, 2, 131 (1957).

15. H. Ehrenreich, J. Phys. Chem. Solids, 8, 130 (1959).

16. R. K. Willardson and A. C. Beer, Semiconductors and Semimetals, Vol. 2, Academic Press, New York (1966).

17. E. Conwell and V. F. Weisskopf, Phys. Rev., 77, 388 (1950)

18. H. Brooks, Phys. Rev., 83, 879 (1951).

19. P. P. Debye and E. M. Conwell, Phys. Rev., 93, 693 (1954).

20. H. Ehrenreich, J. Phys. Chem. Solids, 12, 97 (1959).

21. G. L. Pearson and J. Bardeen, Phys. Rev., 75, 865 (1949).

22. C. Erginsoy, Phys. Rev., 79, 1013 (1950).

23. P. Norton, T. Braggins, and H. Levinstein, Phys. Rev., 8, 5632 (1973).

24. N. Sclar, Phys. Rev., 104, 1559 (1956).

25. L. Spitzer, Jr and R. Harm, Phys. Rev., 89, 977 (1953).

26. E. H. Putley, The Hall Effect and Semiconductor Physics, Dover, New York (1960).

27. J. S. Blakemore, Semiconductor Statistics, Pergamon, New York (1962).

28. A. G. Milnes, Deep Impurities in Semiconductors, Wiley, New York (1973).

29. C. S. Hung and J. R. Gliessman, Phys. Rev., 79, 726 (1950).

30. S. H. Koenig and G. R. Gunther-Mohr, J. Phys. Chem. Solids, 2, 268 (1957).

31. E. A. Davis and W. D. Compton, Phys. Rev., 140, A3183 (1965).

32. W. Baltensperger, Phil. Mag., 44, 1355 (1953)

33. E. Conwell, Phys. Rev., 103, 51 (1956).

34. N. J. Berg and A. G. Lieberman, J. of Appl. Phys., 46, 3475 (1975).

35. D. D. Kleppinger and F. A. Lindholm, Solid State Electron, 17, 199 (1971).

36. C. S. Hung and J. R. Gliessmann, Phys. Rev., 96, 1226 (1954).

37. O. V. Emel'yanenko, T. S. Lagunova, D. N. Nasledov and G. N. Talalakin, Soviet Phys. - Sol. State, 7, 1063 (1965).

38. J. K. Kennedy, Air Force Cambridge Research Lab., L. G. Hanscom Field, Bedford, Mass. 01730.

39. L. J. van der Pauw, Philips Research Reports, 13, 1 (1958).

40. H. Fritzsche, Phys. Rev., 99, 406 (1955).

41. H. Fritzsche, Phys. Chem. Solids, 6, 69 (1958).

42. H. J. Hrostowski, F. J. Morin, T. H. Geballe, and G. H. Wheatley, Phys. Rev., 100, 1672 (1955).

43. H. Fritzsche and K. Lark-Horovitz, Phys. Rev., 99, 400 (1955).

44. N. J. Berg, Ph.D. dissertation (University of Maryland, 1974).

PART II

OPTICAL AND RECOMBINATION PROPERTIES
OF BULK $InAs_{1-x}P_x$ SYSTEM

CHAPTER 1

OPTICAL TRANSMISSION MEASUREMENT
AND ELECTRON MICROPROBE ANALYSIS

I. INTRODUCTION

$InAs_{1-x}P_x$ alloy systems have recently received considerable attention since their energy band gaps cover the near infrared spectrum (i.e., from $0.95\mu m$ to $3.6\mu m$). With this broad range of band gap variation plus high electron mobility, the $InAs_{1-x}P_x$ alloy system offers potential advantages for a number of device applications. These include applications for infrared photocathodes, photodetectors and laser diodes. [1-5]

Early reports on the growth of single crystal InAsP alloy systems were given by Folberth, [6] and by Weiss. [7] A brief report on the study of room temperature electrical properties (conductivity and Hall mobilities) and band gap variation with the alloy composition has also been made by these authors over a finite alloy composition range (i.e., for $x < 0.4$). Ehrenreich[8] calculated the electron mobilities in these alloys over the temperature range from $200°K$ to $500°K$. More recently, Thompson and Wagner[9] reported the growth of bulk ingots of InAsP alloys prepared throughout the entire composition range by pulling the crystal from the melts, using both Gremmelmaier and liquid encapsulation methods. Subsequently, crystal growth of $InAs_{1-x}P_x$ and studies of electrical properties in these alloys were also reported by other researchers. [10-13]

In this paper, we report the energy band gap versus composition on seven undoped bulk samples of $InAs_{1-x}P_x$ alloy (x = 0, .41, .43, .75, .77, .89, 1.00), as determined by optical transmission measurements and electron microprobe analyses. The availability of InAsP samples covering this complete composition range made possible analysis of the nonlinear variation of energy gap with alloy composition.

II. EXPERIMENTAL DETAILS

2.1 Sample Preparation

Seven specimens of bulk $InAs_{1-x}P_x$ ingots with different alloy compositions, obtained from Bell & Howell, Inc.,[9] were used for the present study. These include InAs, InP (W16) and $InAs_{1-x}P_x$ ($0.41 \leq x \leq 0.89$) (see Table I). The H-series samples were grown by the sealed Czochralski technique whereas the W-series samples were grown by the liquid encapsulation technique.[9]

Sample polishing was done with a Multipol Precision polishing machine made by "IMANCO". This machine uses a variation of the Droper System whereby the sample is swept back and forth across one side of the lap, while rotating about its own center, as the lap rotates underneath. This polishing technique greatly improved the flatness of the specimen surface. In order to maintain maximum flatness a precision polishing jig with attached conditioning ring was used. The conditioning ring was used to maintain the

TABLE I Bulk InAs$_{1-x}$P$_x$ Ingots (Undoped)
Produced by Czochralski Technique

Ingot No.	a_o(Å)	$x^{\dagger}$	Total Atomic Percentages of InAsP as Determined by Electron Microprobe Analysis			$x^{\dagger\dagger}$
H1	5.975	0.43	In: 49.15%	As: 28.74%	P: 22.11%	.435
H2	5.944	0.41	49.13%	29.86%	21.01%	.413
H5	5.940	0.75	49.99%	12.46%	37.57%	.751
H6	5.9003	0.77	49.73%	11.70%	38.57%	.767
H7	5.8872	0.89	50.31%	5.37%	44.32%	.891
W-16	-	1.00	50%	-	50%	1.00
InAs	-	0	-	-	-	-

†See reference #16, pp. 19-20 - X-ray powder photography at room temperature assuming Vegard's law is valid.

††x as determined from electron microprobe analysis; where $x = \dfrac{P(\%)}{As(\%) + P(\%)}$ atomic percentage $\times$ 100%

flatness of the lap where, otherwise, high zones on the lap would develop because of the lightly loaded specimen.

A four-step polishing procedure was used starting with a coarse grit silicon carbide powder and finishing with a 0.05 micron Al_2O_3 abrasive solution. Surface quality was checked and compared using a microscope at 40x. Flatness and thicknesses were determined by using a Granit-chek base with a 0.0001" Fowler gauge.

2.2 Optical Transmission Measurements

Optical transmission measurements on each sample were made with a Perkin-Elmer model 98 spectro-photometer. Principal components of this system include a Nernst globar light source, a NaCl prism monochrometer, a 70x power microscope attachment for beam condensing (to handle small size sample), and a thermocouple detector with KBr window and appropriate amplification circuits. The absorption edge of the majority of these $InAs_{1-x}P_x$ samples fell within the most sensitive region of this system. This region, between 1-2μm, was not affected by water vapor in the optical path.

The absorption coefficients were determined from the measured optical transmission coefficient, using the following relation:[14]

$$\alpha = \frac{2.3\log(T_1/T_2)}{(d_2-d_1)}, \text{valid for } R^2 e^{-2\alpha d} \ll 1. \qquad (1)$$

In Eq. (1), α is the absorption coefficient; d_1 and d_2 are different thicknesses of the sample, and T_1 and T_2 are the transmission coefficients corresponding to d_1 and d_2.

Measuring T_1, T_2 as a function of wavelength and knowing d_1, d_2, one can calculate the absorption coefficient versus wavelength from Eq. (1).
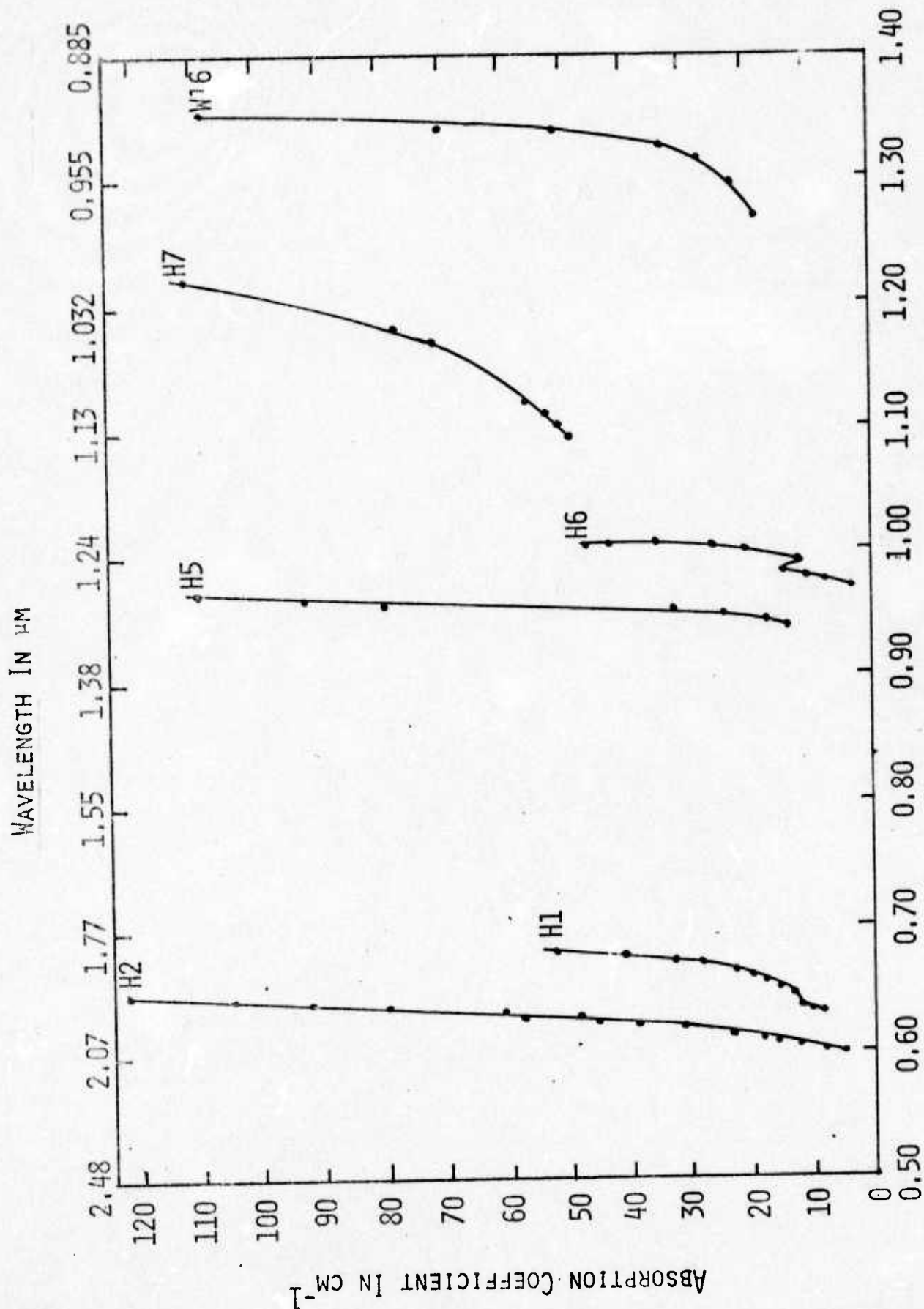
2.3 Electron Microprobe Analysis

Electron microprobe technique was used to determine the arsenic and phosphorus composition of samples H1, H2, H5, H6, H7, and W-16. The samples to be analysed were all embedded in coper-filled diallyi phthalate. A standard metallurgical thermosetting modeling cycle, using an Adolph Buehler Simplimet press, was used to embed the semiconducting samples in the mount. This method facilitates polishing and conductive mounting in the electron microprobe and, in addition, insures that all processing steps for each sample will be identical.

A Cameca MS-64 electron microprobe, made by Actor Laboratories, Inc., was used to determine the As to P ratio. This analysis was based on background corrected x-ray intensities of the sample compared to standards of As, In, and InP (W-16). The relative x-ray intensities for an electron-beam having 1μ diameter, 20keV potential, and an x-ray takeoff angle of 18.0° were obtained for each sample. This information was used in conjunction with a computer program for quantitative microprobe analysis, MAGIC III, which performs all the necessary corrections needed to determine the mean chemical composition in absolute atomic percent. Results of this microprobe analysis are given in Table I, along with some pertinent physical parameters.

III. RESULTS AND DISCUSSION

Composition determined by x-ray powder photography and electron microcprobe analysis agreed with each other within 1% (see Table I). These results greatly increase the accuracy and confidence in the compositions used to determine the bowing effect seen in the energy gap versus composition. Absorption coefficients were calculated near the fundamental absorption edge by using Eq. (1) and transmission measurement data. These coefficients versus photon energy for six bulk samples are displayed in Fig. 1. The square of the absorption coefficient is plotted as a function of photon energy in Fig. 2, whereby E_g can be determined for each sample. In Fig. 2 it was assumed at the higher photon energy part of each curve for direct gap semiconductors that $\alpha^2 \sim (h\nu - E_g)$; where α is the absorption coefficient, $h\nu$ is the photon energy and E_g is the energy band gap of the material. The linear dependence of α^2 on the photon energy $h\nu$ illustrated in Fig. 2 confirms that all these $InAs_{1-x}P_x$ samples are direct band gap semiconductors. Thus a variation in the alloy composition, x, from InAs to InP alters the energy band gap between the conduction band minimum and the valence band maximum at Γ_{15} of the Brillouin zone. Extrapolation of the linear portion of α^2 versus $h\nu$ in Fig. 2 (from the higher-energy part of the curve to the intercept of $h\nu$ axis) was used to determine the energy band gap, E_g (see Fig. 3). The well-known "bowing" effect was

Figure 1. Absorption coefficient versus photon energy for $InAs_{1-x}P_x$ samples H1, H2, H5, H6, H7, W16.

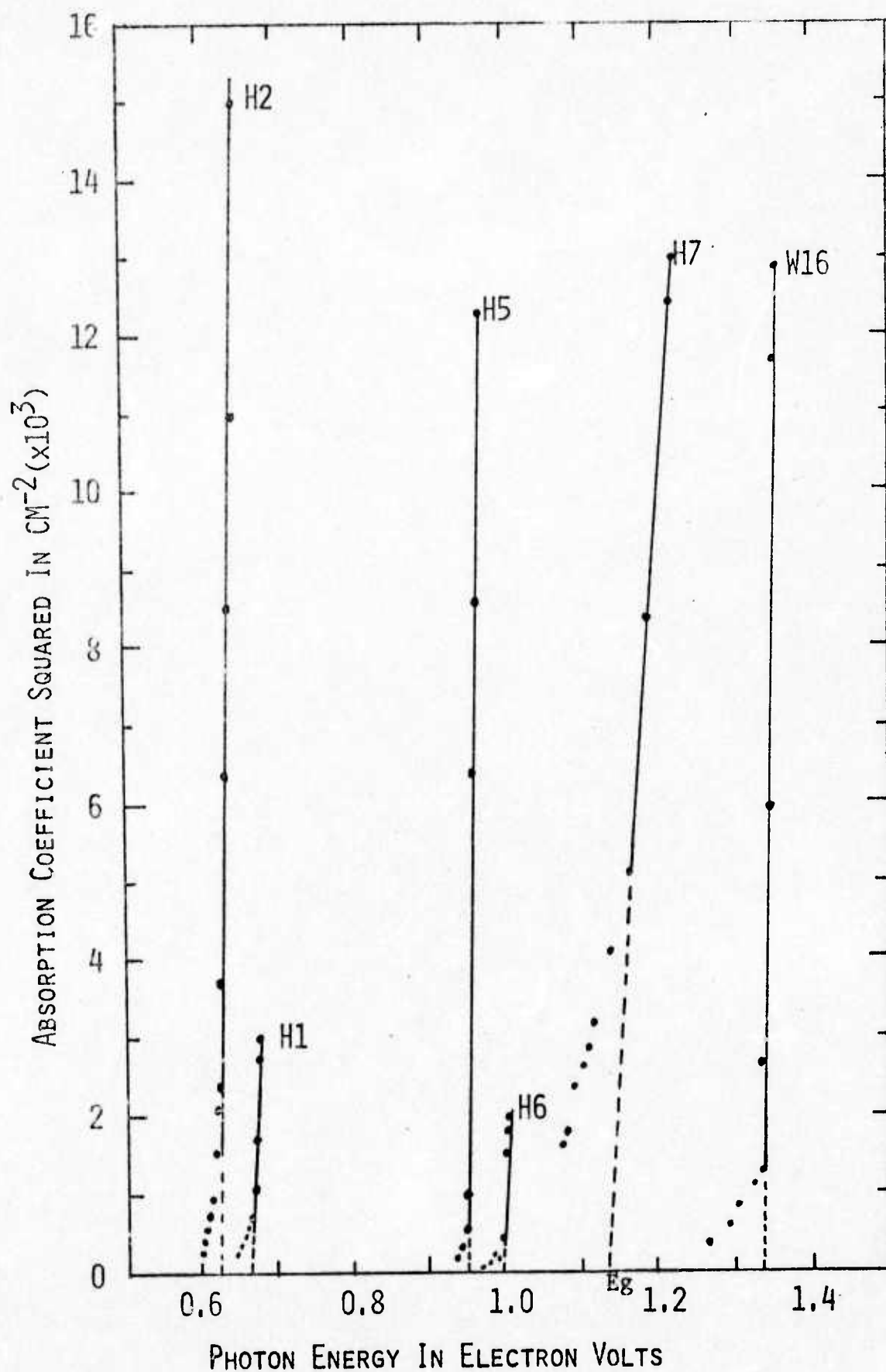Figure 2. The square of the absorption coefficient versus photon energy for $InAs_{1-x}P_x$ samples H1, H2, H5, H6, H7 and W16.

observed, which has been previously predicted as common to all III-V alloys.[15]

In order to evaluate the significance of Fig. 3, Table II was constructed. Thompson and Wooley used E_g = 0.39eV (InAs) and 1.37eV (InP) to establish C = 0.32eV, which agrees with data measured in this report (E_g = 0.36eV and 1.34eV) to give C = 0.325eV. Values indicated in Table II would allow 0.32eV $\leq$ C $\leq$ 0.35eV at 300°K and 0.31eV $\leq$ C $\leq$ 0.32eV at 0°K. Fig. 3 shows plotted points for two other curves of $E_g(x)$ = 0.36 + 0.66x + 0.32x^2 and $E_g(x)$ = 0.36 + 0.52x + 0.4x^2. Clearly, the best fit to the measured data using the extrapolation of α^2 versus hν is obtained for C = 0.40eV. The significance of C = 0.40eV compared to the predicted value of 0.32eV is difficult to explain. A larger C value increases the Bowing effect and increases the apparent errors between composition and energy band gap. The difference cannot be explained by impurity effects because calculated values of N_D - N_A were all in the 10^{16} cm^{-3} range.[16] Although the bulk samples were polycrystalline, the small area used for transmission measurements was usually centered on one single crystal to overcome this problem.

This difference in "C" may be due to the different criteria used to determine the energy gap from the absorption coefficients obtained by transmission data. If E_g was equal to the point where α = 10^3cm^{-1}, the energy band gaps would become 0.38eV, 0.66eV, 0.70eV, 0.98eV, 1.05eV, 1.23eV, and

TABLE II Values of Energy Gap Published for InAs and InP

InAs

300°K	0°K
0.28eV[17]	0.38eV (at 77°K)[17]
0.36eV[18]	
0.33eV[19]	0.46eV[19]
0.36eV[21]	
0.36eV[22]	0.47eV[22]
0.33eV[23]	0.46eV[23]
0.31-0.33eV (Impurity Doping)[24]	
0.34-0.44eV (Impurity measured at $\alpha = 10^3 cm^{-1}$)[24]	
0.39eV[27]	
0.36eV†	

InP

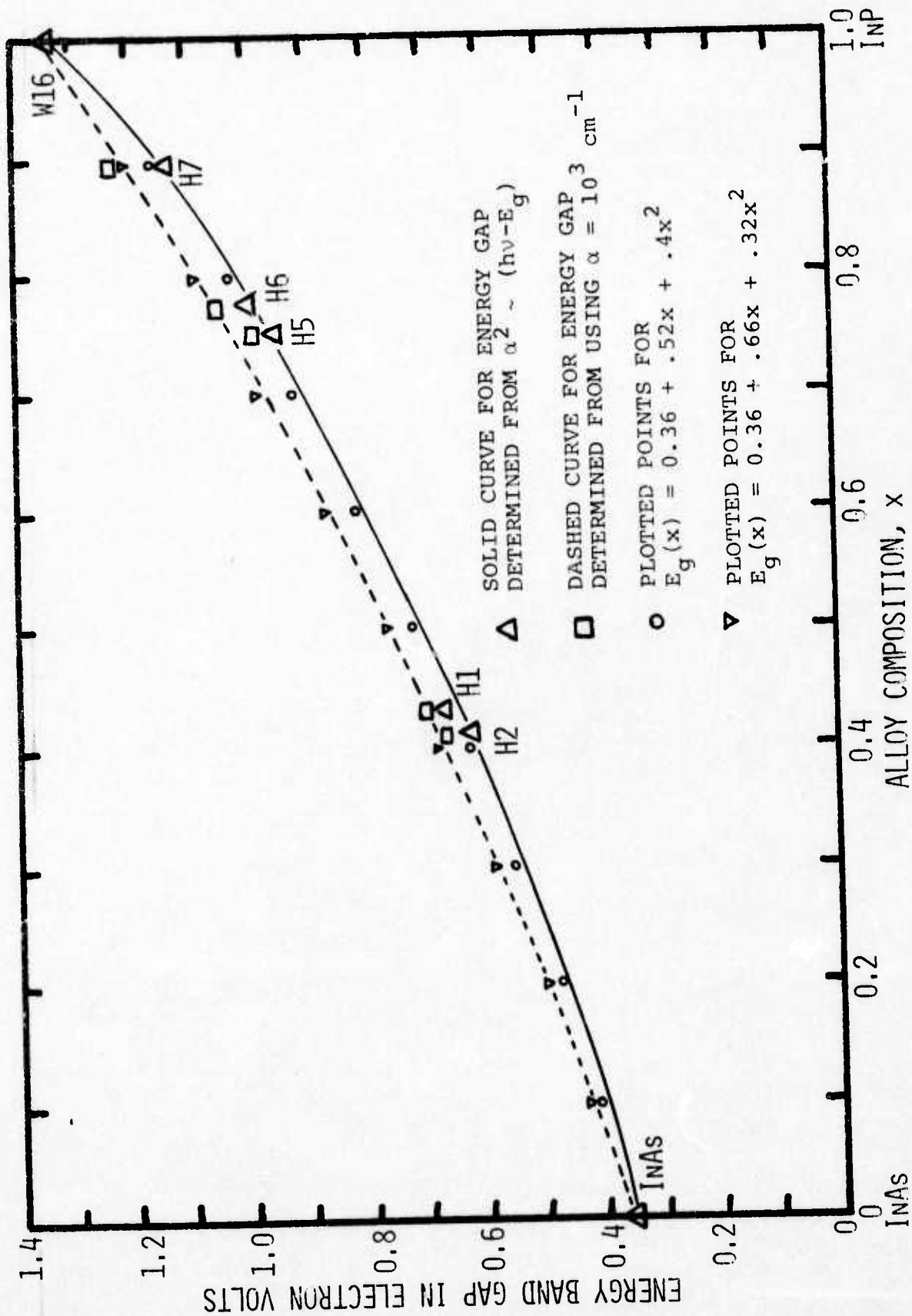| 300°K	0°K
1.28eV[28]	1.42eV[28]
	1.34eV (thermal)[28]
1.29eV[19]	1.34eV[19]
1.20eV[21]	
1.26eV[22]	1.34eV[22]
1.29eV[23]	1.34eV[23]
1.35eV[25]	1.43eV[25]
1.26eV (at $\alpha = 0$ cm^{-1})[26]	1.36eV (at $\alpha = 0$ cm^{-1})[26]
1.33eV (at $\alpha = 10^3 cm^{-1}$)[26]	1.40eV (at $\alpha = 10^3 cm^{-1}$)[26]
1.34eV†	

†Values obtained from experimental work presented in this report.

Figure 3. Energy band gap versus alloy compositions for InAs$_{1-x}$P$_x$ samples H1, H2, H5, H6, H7, W16, and InAs.

1.36eV (Fig. 3). In this case $E_g(x) = 0.36 + 0.66x + 0.32x^2$ would give the best fit to the data and, in addition, would then agree with the prediction of Thompson and Wooley.[15] However, the method utilized for determining E_g from the extrapolation of α^2 is well known in quantum mechanics.[29] Thus, we find no obvious explanation for our observed value of C = 0.4eV.

It is worth noting that the long absorption tail associated with sample H7 shown in Fig. 1 could be due to the presence of a larger amount of defect density in this sample than the rest of the samples.

IV. CONCLUSIONS

The composition of the ternary InAsP alloy system was determined by x-ray powder photography and electron micro-probe analysis. Both methods were found in excellent agreement when compared. Transmission measurements confirmed $InAs_{1-x}P_x$ was a direct gap semiconductor alloy system. The "Bowing Effect" was observed between composition and energy gap. When E_g was determined from $\alpha^2 \sim (h\nu - E_g)$, C = 0.40eV. However, when E_g was determined where $\alpha = 10^3 cm^{-1}$, C = 0.32eV, which agrees with previously published predictions.[15]

REFERENCES

1. A.B. Alexander et al., Appl. Phys. Lett., vol. 4, B-15 (1964).

2. B. Ross, Bull. Am. Phys. Soc., 13, 1640 (1968).

3. H. Macksay et al., J. Appl. Phys., 43, 3533 (1972).

4. H. Sonnenberg, Appl. Phys. Lett., 14, 289 (1969); ibid., 19, 431 (1971).

5. L.W. James, et al., J. Appl. Phys., 42, 580 (1971).

6. Von O.G. Folberth, A. Naturforschg., 10a, 502-503 (1955).

7. Von H. Weiss, A. Naturforschg., 11a, 430-434 (1956).

8. H. Ehrenreich, J. Phys. Chem. Solids, vol. 12, 97-104 (1960).

9. A.G. Thompson and J.W. Wagner, J. Phys. Chem. Solids, vol. 32, 2613-2619 (1971).

10. A.G. Thompson, J.E. Rowe and M. Rubenstein, J. Appl. Phys., 40, 3280 (1969).

11. J.J. Tietjen, H.P. Maruska and R.B. Clough, J. Electro-chem. Soc., 116, 492 (1969).

12. G.A. Antypas and T.O. Yep, J. Appl. Phys., 42, 3201 (1971).

13. S.S. Li, J.R. Anderson and J.K. Kennedy, J. Appl. Phys., 46, 3, p. 1223 (1975).

14. D.L. Greenaway and G. Harbeke, "Optical Properties and Band Structure of Semiconductors," Pergamon Press, p. 9 (1966).

15. A.G. Thompson and J.C. Woolley, Can. J. Phys., 45, 255 (1967).

16. S.S. Li, "Investigation of Basic Electronic Transport, Recombination and Optical Properties in InAsP Alloy Systems for 1~2µm IR Applications," First Semi-Annual Technical Report, Contract No. DAAK02-74-C-0102, June 15, 1974.

17. F. Oswald, Z. Naturforschg., 10a, 927 (1955).

18. S. Swerdling, B. Lax, and L.M. Roth, Phys. Rev., 108, 1402 (1957).

19. S.M. Sze, "Physics of Semiconductor Devices," Wiley, p. 20 (1969).

20. K. Wiser and R.S. Levitt, *Appl. Phys. Lett.*, 2, 178 (1963).

21. H. Ehrenreich, *J. Appl. Phys.*, 32, 2155 (1961).

22. K. Seeger, "Semiconductor Physics," Springer-Verlag, p. 16 (1973) (From Madelung, "Physics III-V Compounds," Wiley, 1964).

23. F. Blatt, "Physics of Electronic Conduction in Solids," McGraw-Hill, p. 247 (1968). (From C. Hilsum and A.C. Rose, "Semiconducting IV-V Compounds," Pergamon Press, 1961).

24. W. Spitzer and H. Fan, *Phys. Rev.*, 106, 882 (1957).

25. Y. Tsay, B. Gong, S. Mitra, and J. Vetelino, *Phys. Rev. B.*, 6, 2330 (1972).

26. R. Newman, *Phys. Rev.*, 111, 1518 (1958).

27. I. Melngailis, *Appl. Phys. Lett.*, 2, 176 (1963).

28. H. Welker, *Z. Electron.*, 1, 181 (1955).

29. K. Seeger, "Semiconductor Physics," Springer-Verlag, pp. 369-371 (1973).

CHAPTER 2

SURFACE PHOTOVOLTAGE MEASUREMENT

I. INTRODUCTION

This chapter describes the application of the surface photovoltage (SPV) method to determine the hole diffusion length in n-type InP single crystals with (111) and (100) orientations. The SPV method has been used by previous investigators [1-7] to measure the minority carrier diffusion length in bulk semiconductor materials, the epilayers (n/n$^+$ or p/p$^+$ junction), and the pn junction solar cells.

The SPV method provides a nondestructive means of measuring minority carrier diffusion lengths and is suitable for process control applications, and for material acceptance tests.

II. THEORY

The theory of the SPV method has been reported by previous investigators [3-9], and the results pertinent to this work will be described briefly in this section.

The specimen surface is illuminated with chopped monochromatic radiation of energy slightly greater than the bandgap of the semiconductor. Electron-hole pairs are produced and diffused to the surface where they are separated by the electric field of a depletion region to produce a surface photovoltage (SPV). The SPV signal is capacitatively coupled into a lock-in amplifier for amplification and measurement.

125

The light intensity is adjusted to produce the same value of SPV at different wavelengths of illumination. The photon intensity required to produce this constant SPV signal is plotted as a function of the reciprocal absorption coefficient for each wavelength. The resultant linear plot is extrapolated to zero intensity and the negative intercept value is the effective minority carrier diffusion length.

The SPV signal developed at the illuminated surface of a semiconductor specimen is a function of the excess minority carrier density injected into the surface space charge region. The excess carrier density is in turn dependent upon the incident light intensity, the optical absorption coefficient, and the minority carrier diffusion length. The minority carrier diffusion length is determined by measuring the variation of SPV with optical absorption coefficient. An accurate knowledge of absorption coefficient versus wavelength is required for the SPV method. It can be shown that the surface photovoltage for an n-type semiconductor may be written as [2]:

$$V_{sp} = f(\Delta p) \tag{1}$$

and

$$\Delta p = \frac{\eta I_o (1-R)}{(D/L) + S} \frac{\alpha L}{1 + \alpha L} \tag{2}$$

where Δp is the excess hole density, η is the quantum efficiency, I_o is the light intensity, R is the reflection coefficient, D is the hole diffusion coefficient, S is the surface recombination velocity, α is the optical absorption coefficient, and L

is the hole diffusion length. Equation (1) is valid if $\alpha \gg L$, $n \gg \Delta p$, and $\alpha d > 1$ (where d is the specimen thickness).

If η and R are assumed constant over the measured wavelength interval, the incident light intensity, I_o, required to produce a constant SPV, V_{SP}, is a linear function of the reciprocal absorption coefficient, α^{-1}

$$I_o \sim C(\alpha^{-1} + L) \tag{3}$$

where C is a constant, independent of the photon wavelength. The linear plot of I_o versus α^{-1} is extrapolated to zero intensity and the (negative) intercept value is the effective hole diffusion length.

III. EXPERIMENT

Undoped InP single crystal wafers of (111) and (100) orientations were used for SPV measurements. The wafers, about 10 mil thick and 0.5" diameters, were polished mechanically on one side and lapped on the other side. In order to enhance the SPV signal, all three specimens were treated by boiling the specimens in dionized water for 30 minutes [10] prior to the SPV measurement to adjust the surface conditions (i.e., to create a surface depletion region). In addition, the two specimens with (100) orientation were also etched in HF for one minute prior treatment in boiling water; however, no noticeable changes in SPV signal were observed.

The experimental arrangement for the SPV measurement is similar to that reported elsewhere [5,11]. The specimen surface is illuminated with chopped monochromatic light of energy slightly greater than the band-gap of InP (e.g., $\lambda \sim 0.7$ μm to 0.94 μm was used for this work). The SPV signal is capacitatively coupled into a lock-in amplifier for amplification and measurement. The photon intensity ($I_o = \lambda \cdot V_D$; V_D is the voltage reading from a thermopile) is adjusted to produce the same value of SPV at various wavelengths of incident photons. The photon intensity required to produce this constant SPV signal is plotted against the reciprocal absorption coefficient for each wavelength. The resultant linear plot is extrapolated to zero photon intensity and the negative intercept value is the effective minority carrier diffusion length. The optical absorption coefficient for InP for the wavelength interval of interest is listed in Table I.

IV. RESULTS AND DISCUSSIONS

Results of the SPV measurement for InP specimens are shown in Figs. 1 to 3. Fig. 1 shows the I_o versus α^{-1} plot for the InP specimen fo (111) orientation, for $V_{SP} = 100$ and 160 μV; the intercept with α^{-1} axis at $I_o = 0$ yields hole diffusion length $L = 1.8$ μm. Figs. 2 and 3 show the plot of I_o versus α^{-1} for specimens S-1 and S-2, both of (100) orientation. The intercept of I_o versus α^{-1} plots with α^{-1}

TABLE I

Optical Absorption Coefficient of InP at 300°K [12]

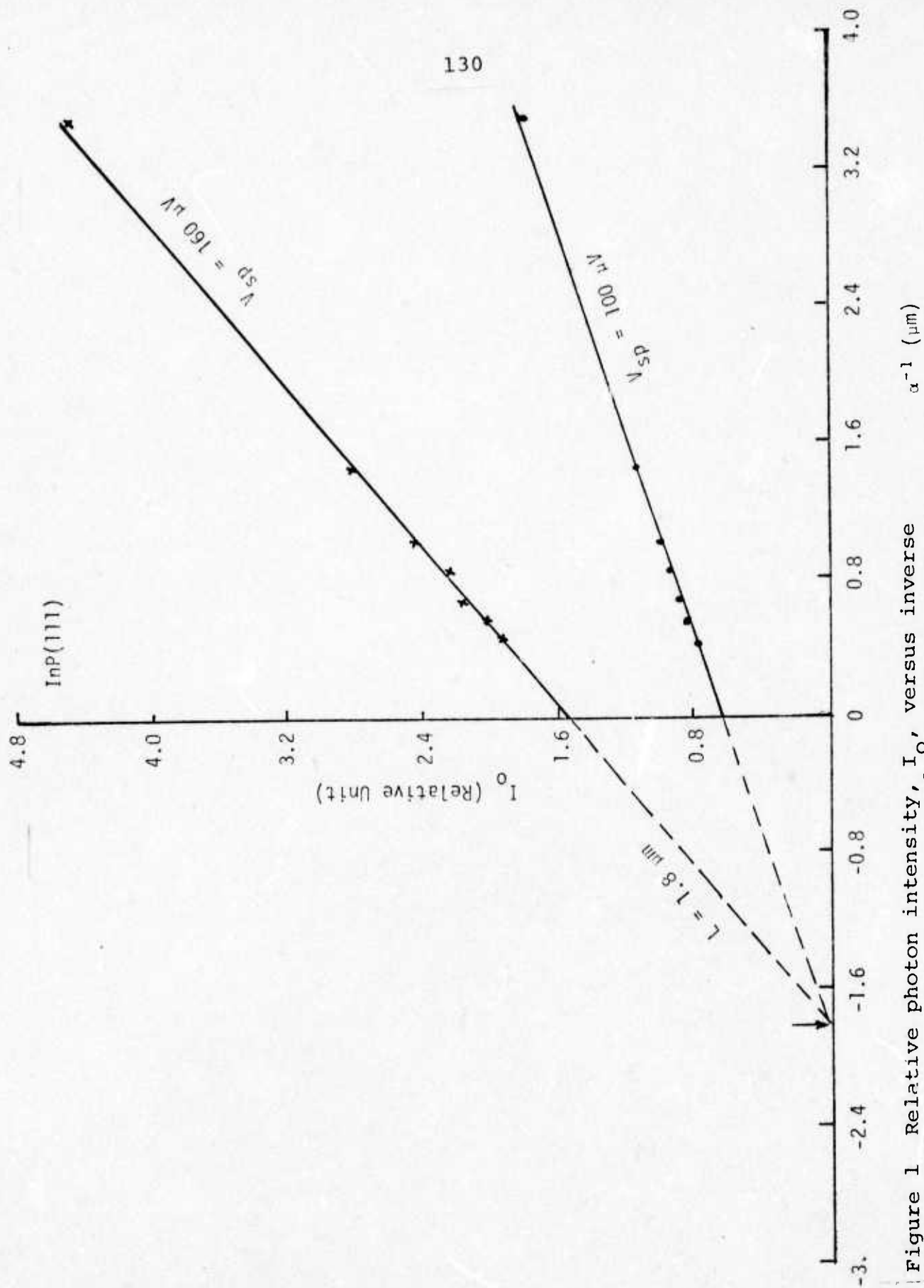| λ (μm)	0.7	0.75	0.80	0.85	0.88	0.90	0.91	0.92	0.93
α (cm^{-1})	3.5×10^4	3.1×10^4	2.3×10^4	1.8×10^4	1.5×10^4	1.2×10^4	10^4	7.1×10^3	2.9×10^3

Figure 1 Relative photon intensity, I_0, versus inverse absorption coefficient, α^{-1}, for the InP specimen of (11ī) orientation.
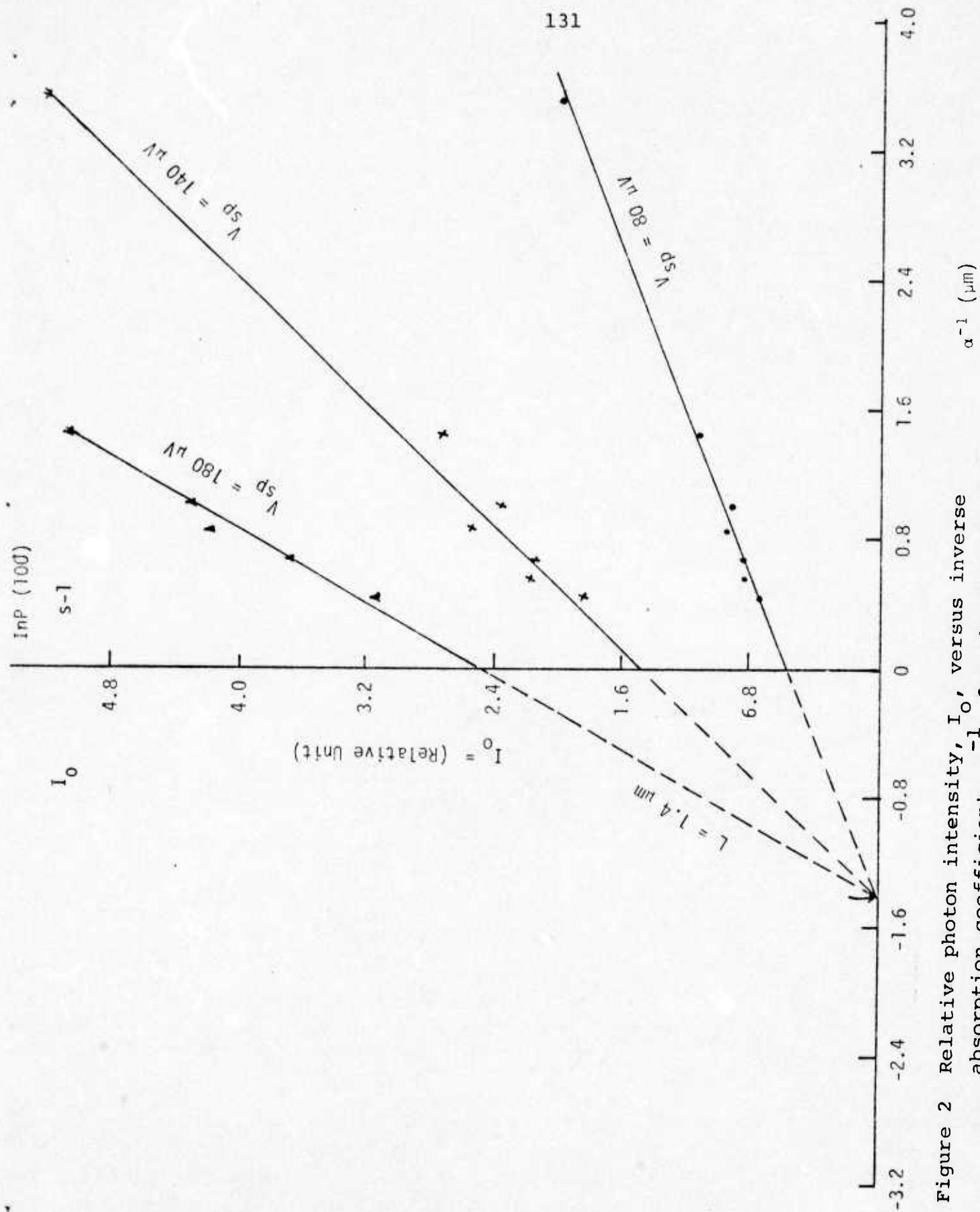
Figure 2 Relative photon intensity, I_0, versus inverse absorption coefficient, α^{-1}, for the InP specimen S-1 of (100) orientation.
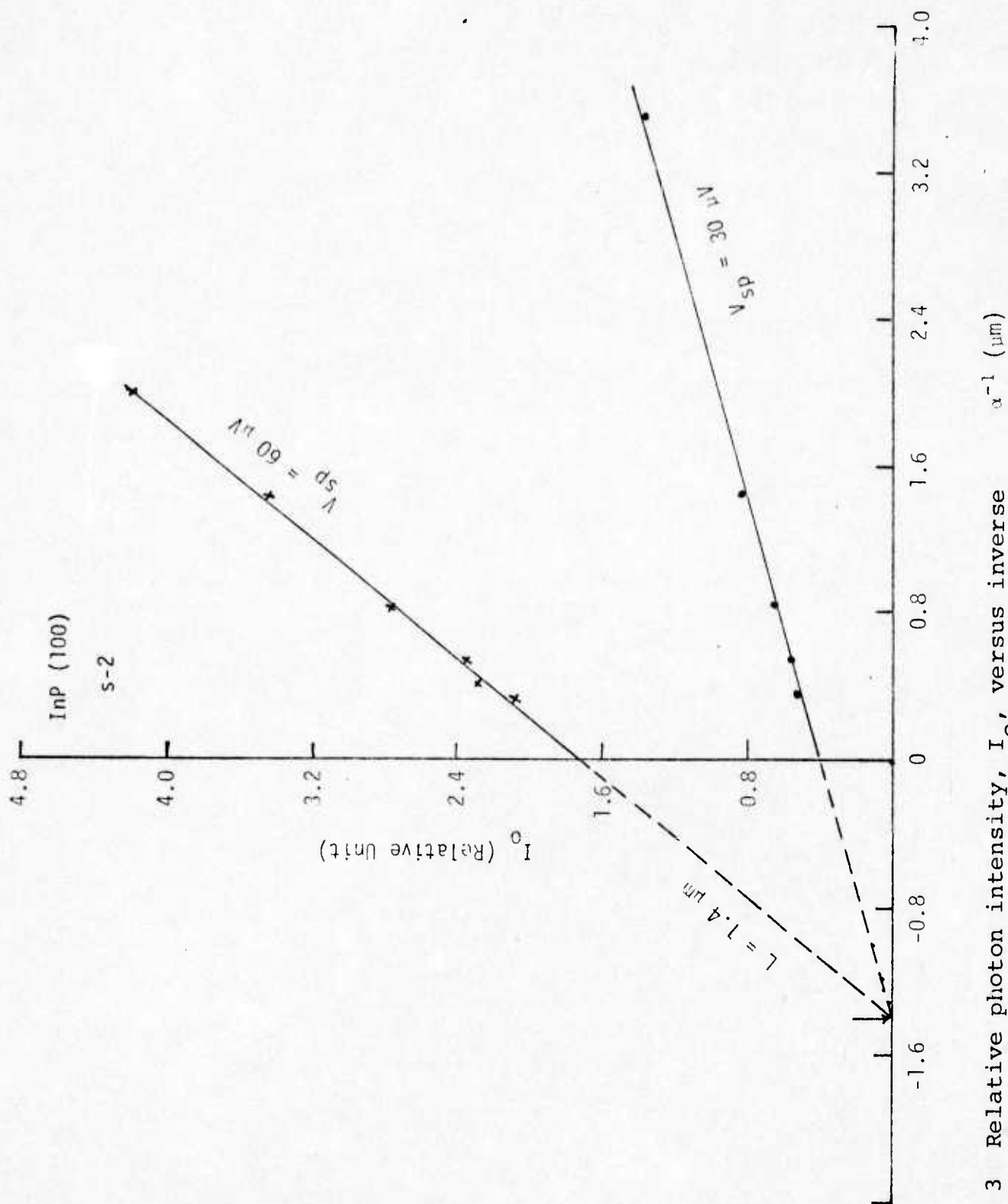
Figure 3 Relative photon intensity, I_o, versus inverse absorption coefficient, α^{-1}, for the InP specimen S-2 of (100) orientation.

axis yields a hole diffusion length of 1.4 μm. Note that the SPV signal for specimen S-1 is much larger than for specimen S-2. This is due to the fact that surface conditions for specimen S-2 are worse than specimen S-1 (e.g., with deep saw mark existing even after polishing). However, it is interesting to note that the resulting hole diffusion length is the same for both specimens, indicating that the measured hole diffusion length is the true bulk diffusion length independent of the surface conditions.

From our least square fitting of plots shown in Figs. 1 to 3, the overall error for this measurement is estimated to be less than ± 10 percent, which comes mainly from uncertainty in α^{-1} and instrument readings. It is worth noting that surface treatments are extremely important for the SPV method. For example, by boiling the InP specimens in the deionized water for 30 minutes we were able to improve the SPV signal by one to two orders of magnitude to that of the untreated specimens.

In conclusion, we have demonstrated the use of the SPV method to measure the hole diffusion lengths in the range from 1 to 2 μm for InP single crystals.

REFERENCES

1. E. O. Johnson, J. Appl. Phys., 28, 1349 (1957).

2. A. M. Goodman, J. Appl. Phys., 32, 2550 (1961).

3. J. Vilm and W. E. Spicer, ibid., 36, 2815 (1965).

4. R. M. Esposito, J. J. Lofferski and H. Flicker, ibid., 38, 825 (1967).

5. W. E. Philips, Solid-State Electron., 15, 1097 (1972).

6. W. M. Bullis and T. J. Baroddy, Jr., NBS Tech. Notes, 555, p. 9 (1970).

7. E. Y. Wang, C. R. Baraona and H. W. Brandhorst, Jr., J. Electrochem. Soc., 121, 973 (1974).

8. T. S. Moss, J. Electron Control, 1, 126 (1955).

9. E. O. Johnson, Phys. Rev., 111, 153 (1958).

10. S. C. Choo and A. C. Sanderson, Solid-State Electron., 13, 609 (1970).

11. Annual Book of ASTM Standards, p. 752 (1974).

12. Electronic Properties of Solids, p. 21.